Electronic Theses and Dissertations, 2020-

2022

An Investigation of the Relationship Between Respiration and Seismocardiographic Signals Using Signal Processing, Machine Learning and Finite Element Analysis

Tanvir Hassan
University of Central Florida

University of Central Florida

STARS
Showcase of Text, Archives, Research & Scholarship

AN INVESTIGATION OF THE RELATIONSHIP BETWEEN
RESPIRATION AND SEISMOCARDIOGRAPHIC SIGNALS USING SIGNAL
PROCESSING, MACHINE LEARNING AND FINITE ELEMENT ANALYSIS

by

TANVIR HASSAN
M.Sc. in Mechanical Engineering, University of Central Florida, 2019
B.Sc. in Mechanical Engineering, Bangladesh University of Engineering & Technology,
Bangladesh, 2014

A dissertation submitted in partial fulfillment of the requirements
for the degree of Doctor of Philosophy
in the Department of Mechanical and Aerospace Engineering
at the College of Engineering and Computer Science
at the University of Central Florida
Orlando, Florida

Spring Term
2022

Major Professor: Hansen A. Mansy

ABSTRACT

Cardiovascular disease (CVD) is one of the major causes of death worldwide. Disease management, as well as patient health, can be significantly improved by early detection of patient deterioration and proper intervention. Review of the patient's medical history and physical examination including stethoscope auscultation and electrocardiograms (ECG), echocardiography imaging, numerous blood testing, and computed tomography are common means of evaluating cardiac function. Seismocardiographic (SCG) signals are the vibrations of the chest wall due to the mechanical activity of the heart. These signals can provide useful information about heart function and could be used to diagnose cardiac problems. The variability in SCG waveforms may make it difficult to obtain accurate waveforms, limiting SCG clinical value. Breathing is a well-known source of change in SCG morphology. In this dissertation, SCG variability due to respiration is described, related signal characteristics changes are measured, and the effects of breathing states and maneuvers are discussed. Increased SCG variability understanding can aid in accounting for variability in signal as well as more accurate characterization of significant features in SCG that could correlate with heart health.

Direct airflow measurement is frequently used to assess respiration. When direct airflow access is difficult or unavailable, indirect ways to breathing monitoring might be used. The seismocardiographic signal is influenced by respiration. As a result, this signal can be utilized to noninvasively determine the respiratory phases. Hence, SCG may reduce the requirement for direct airflow measurements in situations where SCG signals are easily

available. This dissertation extracts respiration derived from SCG in healthy adults using machine learning techniques and compares the results with direct respiration airflow measurements.

Finite element method (FEM) was implemented to perform SCG simulation during different breathing states by modeling the myocardial movements propagation to the surface of the chest. SCG waveforms predicted by FEM analysis were comparable with SCG signals measured at the surface of the chest suggesting that myocardial activity is the SCG main source. The effects of increased soft tissue in the chest wall on SCG signal were investigated and were found to decrease SCG amplitude. The research led to an enhanced understanding of the SCG variability sources as well as respiratory phase-detection methods. These discoveries could lead to better non-invasive, low-cost approaches development for managing cardiovascular disorders, which can enhance patient quality of life.

This dissertation is dedicated to my parents

MD Sirajul Islam

and

Shirina Islam

who have given me their endless love, support and encouragement.

ACKNOWLEDGMENT

research but is also contributing to all aspects of my life. Her relentless encougement and care have brought the best out of me.

My deep appreciation goes to my amazing parents and siblings for always encouraging me and supporting me at every step of my life. They have immense contribution in each of my success. I am truly grateful to have each of them in my life. At last but not the least, I'd like to express my gratitude to my friends and family for their unwavering support over the years.

TABLE OF CONTENTS

LIST OF FIGURES

xviii

LIST OF TABLES

CHAPTER 1 - INTRODUCTION

In the United States, cardiovascular disorders are one of the main causes of disability and mortality (Virani et al., 2020). As a result, new methods for detecting cardiovascular disease early are needed. The most common procedures for assessing heart function include a history and physical examination, stethoscope auscultation, electrocardiograms (ECG), echocardiographic imaging, and several tests of the blood. Though these treatments can give important diagnostic data, these usually necessitate medical assistance and are only used in clinical settings. Vibrations over the chest surface induced by heart action are known as seismocardiographic (SCG) signals (Bozhenko, 1961). Mechanical activity such as valve closures, blood momentum changes, and cardiac muscle contraction have been linked to these vibrations in the past (Salerno, 1990; Crow, Hannan, Jacobs, Hedquist, & Salerno, 1994; Tavakolian et al., 2012; Taebi & Mansy, 2017; Taebi, Sandler, Kakavand, & Mansy, 2017; Taebi, 2018). Because SCG signals give information about heart function, they may be proven useful in the cardiovascular diseases diagnosis and monitoring. SCG signals were used to extract several parameters of the heart such as systolic time intervals and heart rate (Shafiq, Tatinati, Ang, & Veluvolu, 2016; Taebi & Mansy, 2017; Taebi, Bomar, Sandler, & Mansy, 2018). In phonocardiography (PCG), electronic stethoscopes are used to record sounds caused by blood flow, valve closure and ventricular filling. Seismocardiography (SCG) is a technique for evaluating heart function that involves using accelerometers to detect the chest wall surface vibrations. In ambulatory settings, it can be utilized in conjunction with other modalities. PCG, on the other hand, may not always contain low-frequency heart vibratiosns like S3 and S4 (Glower et al., 1992; Siejko et al., 2013; Hosenpud & Greenberg, 2007). SCG, which can detect low

frequency vibrations with high precision and may also be implemented to recognize cardiac events such as aortic opening, mitral opening, and isovolumetric contraction (Tavakolian, 2016; Crow et al., 1994). In additions, breathing, stomach noises, and body movements may contain traces SCG signals.

As previously stated, SCG signals provide information about the chest wall surface audible and infrasonic vibrations (Taebi et al., 2019; Taebi & Mansy, 2017; Taebi & Mansy, 2017; Taebi et al., 2019) . The frequency of SCG signals was studied in healthy persons. According to Taebi, SCG signal intensities peaked at two points during the cardiac cycle, matching PCG's S1 and S2 sounds which are referred to as SCG1 and SCG2, respectively. When measured at the lower left sternal border in the 4th intercostal space, SCG1 usually exhibits a larger signal intensity than SCG2. The power spectral density (PSD) of SCG1 identified three key frequencies. These are lower domiant frequency 9 Hz, 25 Hz, and higher dominat frequency 50 Hz. The lower dominant frequency of 9 Hz may correspond to ventricular contraction, and the higher dominant frequency of 50 Hz correspond to atrioventricular valve closure, according to Taebi. This demonstrates how SCG signals, which offer data at lower frequencies than PCG signals, can be used to extract extra information about the mechanical activity of the heart. SCG variability, particularly respiratory variability, is little understood, despite its potential utility. These variabilities may mask important diagnostic SCG morphological traits or, conversely, make SCG interpretation problematic. As a result, lowering variability and/or improving our understanding of its origins will increase the utility of SCG. A better understanding of SCG variability could help account for it while also allowing for a clearer interpretation of key SCG features to improve diagnostic predictive value.

The proposed study will focus on SCG variability in relation to respiration, which has not been adequately investigated in previous research.

SCG signal variability during normal breathing and breath holding at varying airway pressure

To help reduce variability with respiration, some earlier studies (Taebi & Mansy, 2017; Solar, Taebi, & Mansy, 2017) categorised SCG events according to their lung volume phases (high lung volume/low lung volume) or respiratory flow (inspiration/expiration). SCG waveforms were better sorted into groups with the least intra-group variability using unsupervised machine learning, according to a previous work (Gamage, Azad, Taebi, Sandler, & Mansy, 2018). Clustering SCG events by lung volume phases, rather than respiratory flow phase, may yield more homogeneous groupings, according to that previous study. SCG fluctuation during breath holding has been less studied in the previous literature. The goal of this study is to see how SCG varies from normal breathing to holding a breath at different lung capacities and airway pressures. Several variables that cause variability (such as heart position and intrathoracic pressure) are altered with breathing. Two SCG signals are shown in Figure 1 during distinct stages of respiration.
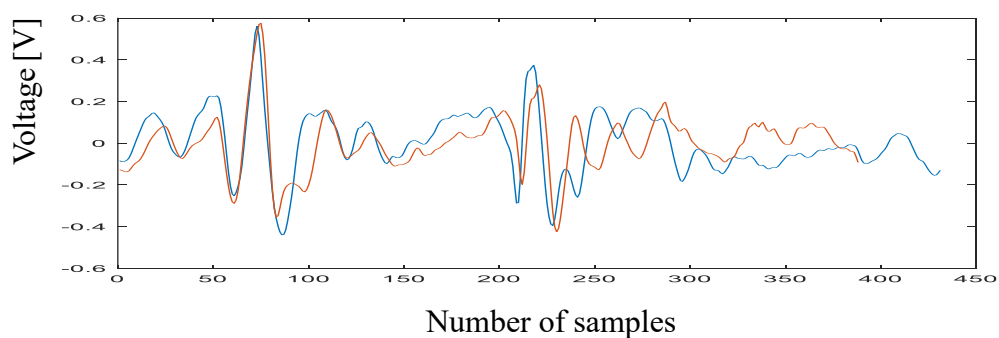
Figure 1 SCG variability with breathing.

The identification of respiratory phase from SCG using machine learning

A mouthpiece or other breathing airflow access is typically utilized to measure respiration. When gaining direct access to breathing airflow is inconvenient or difficult, it could be necessary to use an indirect method of respiration detection. The morphological changes in SCG as a function of respiration have previously been studied (Tavakoliyan et al., 2009; Zakeri et al., 2009). As a result, the respiratory signal can be derived from the SCG signal non-invasively, eliminating the requirement for a less convenient method under certatin circumstances, which is especially useful in an ambulatory context. The accuracy of pulmonary phase calculated from the SCG signals was compared with direct breathing assessment in this study.

Finite element analysis of SCG signal

Understanding how the waveform of SCG signal obtained on the chest wall relates to heart activity could help improve SCG's utility as a reliable diagnostic tool for cardiac problems. Electrocardiography has been used to identify several peaks in a cardiac cycle of SCG (Giorgis et al., 2008; Crow, Hannan, Jacobs, Hedquist, & Salerno, 1994). The findings, however, are still controversial (Akhbardeh et al., 2009). Because of intricate motions of the heart walls, it's difficult to link cardiac movements to SCG morphology. Certain cardiac events that occur at different locations in the heart may overlap, boosting or negating their impact on SCG morphology. However, capturing heart motions and correlating them with the SCG utilizing 4D cardiac image processing and Cine-MRI imaging techniques may aid in finding the signal's origins. Furthermore, realistic 3D heart movement capture might be used to create a computer model to analyze heart movement transmission to the cheat wall from Cine-MRI. One purpose

of this research is to create a computational model that accurately replicates the distribution of cardiac motions to the surface of the chest. The effects of increased soft tissue in the chest wall were also investigated in this study. This type of computer model can be used to investigate the relation between SCG and cardiac motions, as well as to understand SCG's origins.

CHAPTER 2 – SCG SIGNAL VARIABILITY DURING NORMAL BREATHING AND BREATH HOLDING AT VARYING AIRWAY PRESSURE

The variability of SCG waveforms may make it difficult to extract accurate SCG waveforms, limiting its clinical value. If the variability of the SCG is reduced and the sources of variability are better understood, the utility of the SCG can be increased. Breathing is one known source of SCG variation. The position of the heart and the pressure around it are altered while breathing. These modifications may lead to variability the causes problems in SCG interpretation, but they may also contain diagnostic SCG morphological traits. Improved understanding of the causes of variability may aid in the extraction of more accurate SCG waveforms, as well as providing key elements that increase SCG's diagnostic predictive value. There is limited published information about SCG changes during breath holding (BH) to our knowledge. SCG and heart rate fluctuations during regular breathing are compared to BH in this experiment. Some of the characteristics that generate variability (such as heart position) can be maintained during BH. SCG morphological changes at different breathing states can help us better understand SCG sources and identify the optimal breathing states and recording procedures.

Materials and methods

Following IRB permission, we recruited 20 healthy volunteers (Female=14, Male=6, Age: 21±2 years). Subjects were asked to lie supine on a bed with their feet extended horizontally and their head angled to 45 degrees. The methods used in our research is depicted in Figure 2.
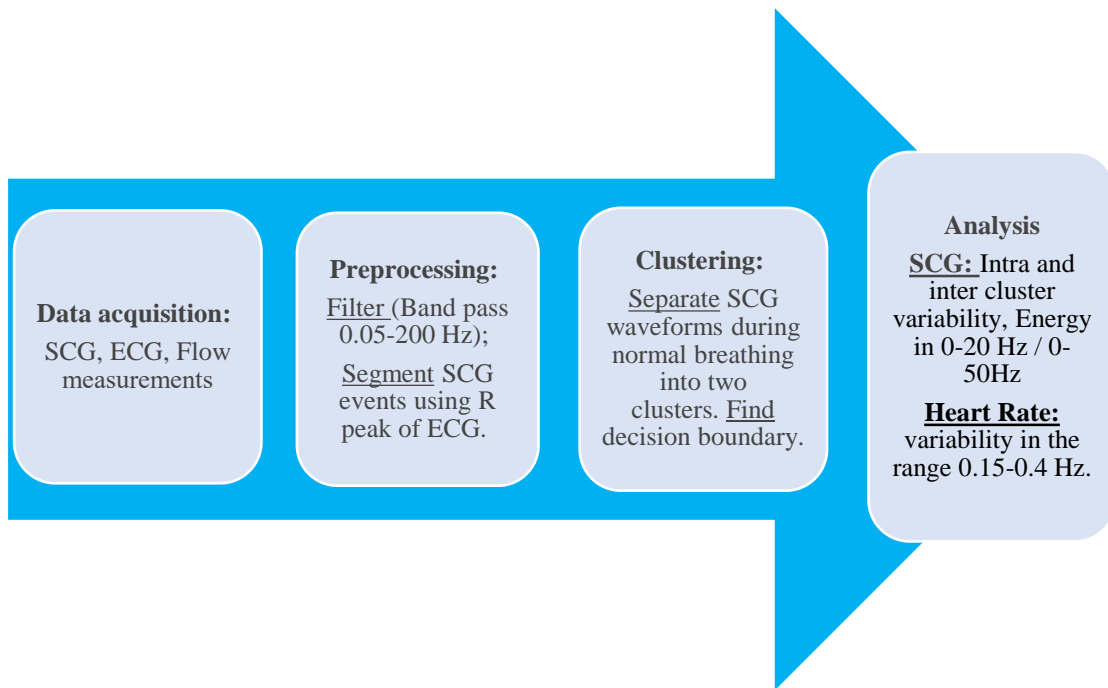
Figure 2 SCG acquisition and analysis methodology.

Data acquisition

A biopotential recorder was used to record the ECG signal (IX-B3G, iWorx Systems, Inc., Dover, NH). A tri-axial accelerometer was used to capture SCG signals (Model: 356A32, PCB Piezotronics, Depew, NY). The sensor was taped to the chest surface in the 4th intercostal space near the left lower sternal border with double-sided medical grade adhesive. A spirometer was used to assess the rate of breathing (Model: A-FH-300, iWorx Systems, Inc., Dover, NH). Figure 3 depicts the experimental setup and sensor placements.
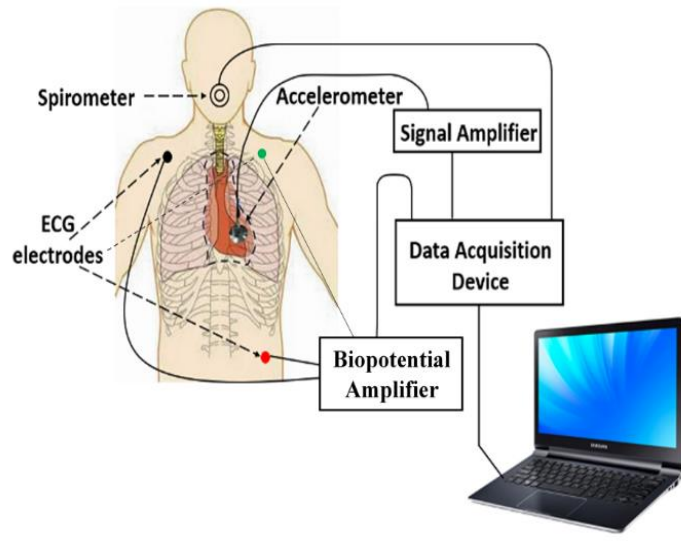
Figure 3 Locations of sensors and experimental setup.

Protocol for collecting data during normal breathing

The first step in performing experimental protocol is to collect data during normal breathing. Here, all studies were done with an air tight face mask covering the nose and mouth and was connected to the spirometer. Figure 4 shows typical flow rate data during normal breathing. The participants were given two minutes to rest while using a spirometer to measure their breathing. The baseline tidal volume was measured during this time. Next, subjects practiced breathing at a tidal volume that is within +/-10-20% of their baseline. Core signals (tri-axial SCG, ECG, and Spirometer flow rate) were collected for 5 minutes (while volunteers maintained a tidal volume of +/-20% of baseline). Flow rate vs. time is plotted in Figure 4 during normal breathing.
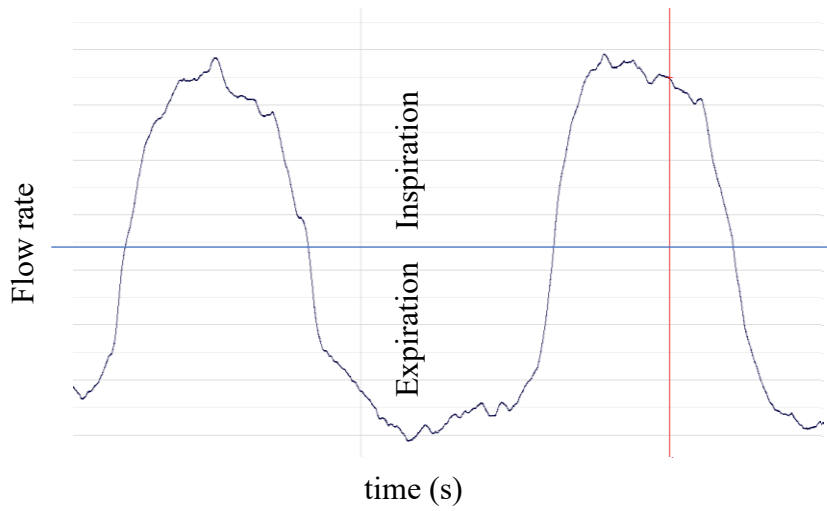
Figure 4 Flow rate vs. time normal breathing.

Protocol for collecting data during breath holding at end inspiration and end expiration

This protocol was performed during breath holding while maintaining an open
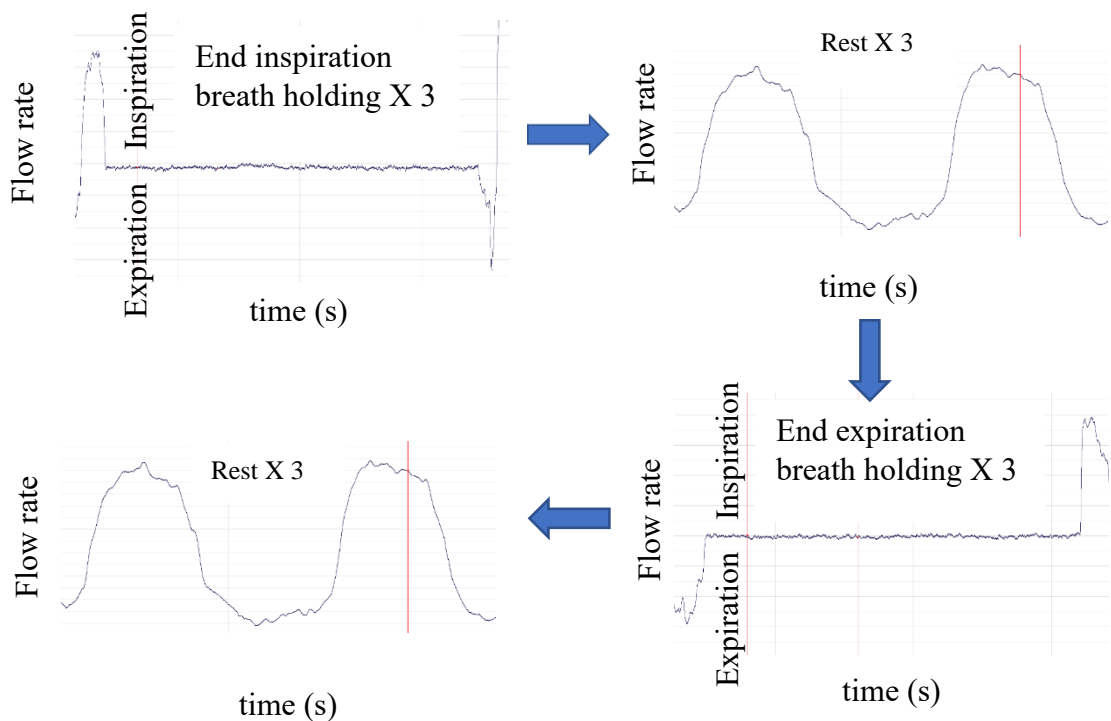
Figure 5 flow rate vs. time during breath holding at end inspiration and end expiration.

glottis. End inspiration BH was conducted for 20 seconds (or as long as feasible) while the signals were being recorded, then a three-minute rest time followed. This cycle was repeated two more times (a total of 3 cycles for end inspiration). Three end expiration BH trials (20 seconds each, if possible) were carried out in the same manner, with three minutes of rest in between. Figure 5 depicts the flow rate vs. time during breath holding at the conclusion of inspiration and exhalation.

Protocol for collecting data during varying airway pressure at breath holding
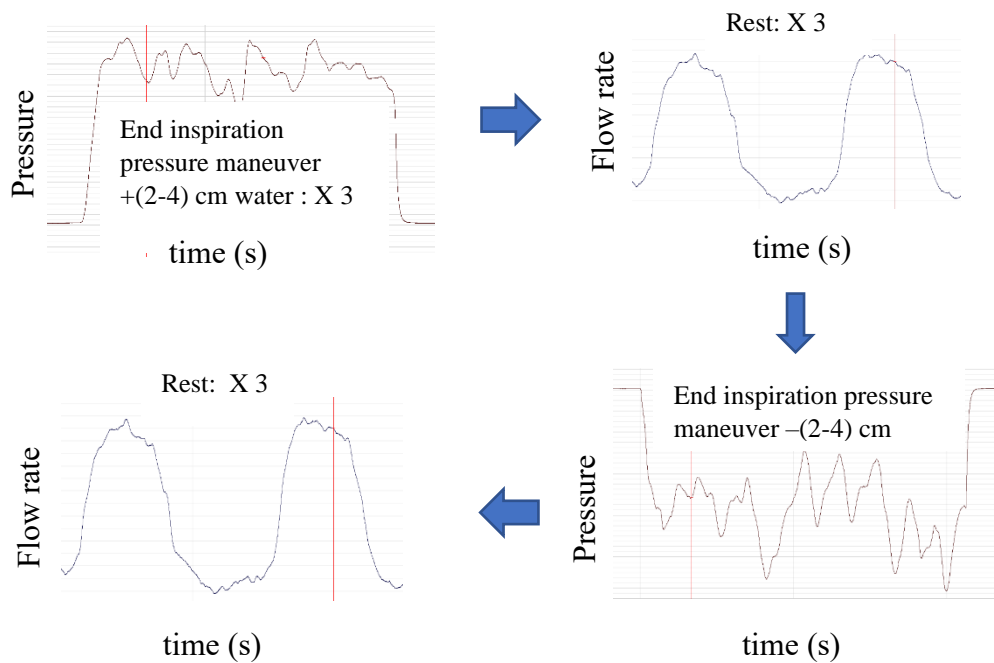
Figure 6 Pressure and flow rate vs. time during end inspiration positive and negative 2-4 cm water pressure.

This experiment is done with open glottis, blocked airflow, face mask covering the nose and mouth connected to the manometer. Here, the experiment is to perform data collection with "normal" airway pressures (positive and neg 2-4 cm water pressure) and with increased airway pressures (positive and neg 15-20 cm water pressure). Then, with 2 minutes of rest between trials, three trials of raised and

10

decreased airway pressure of 2-4 cm and 15-20 cm water at end inspiration and end

expiration were done after subjects have done enough practice following the protocol.
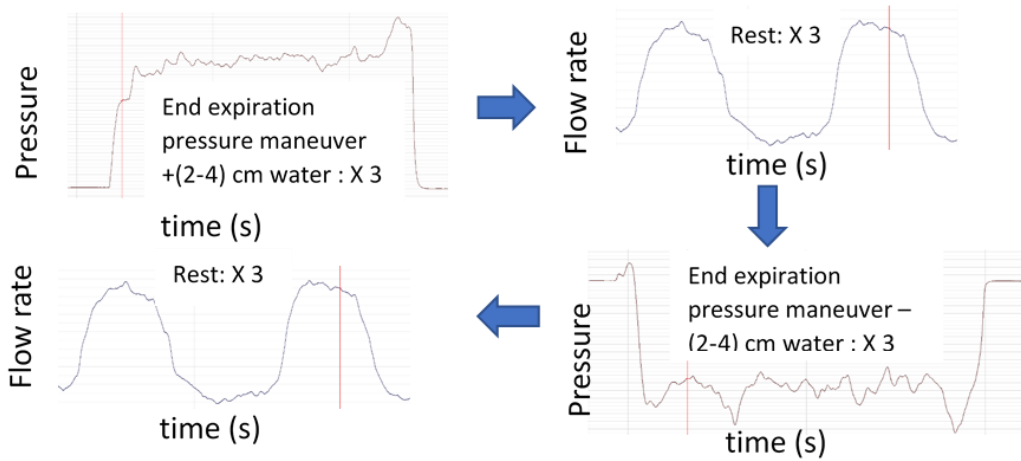
Figure 7 Pressure and flow rate vs. time during end expiration positive and negative 2-4 cm water pressure.
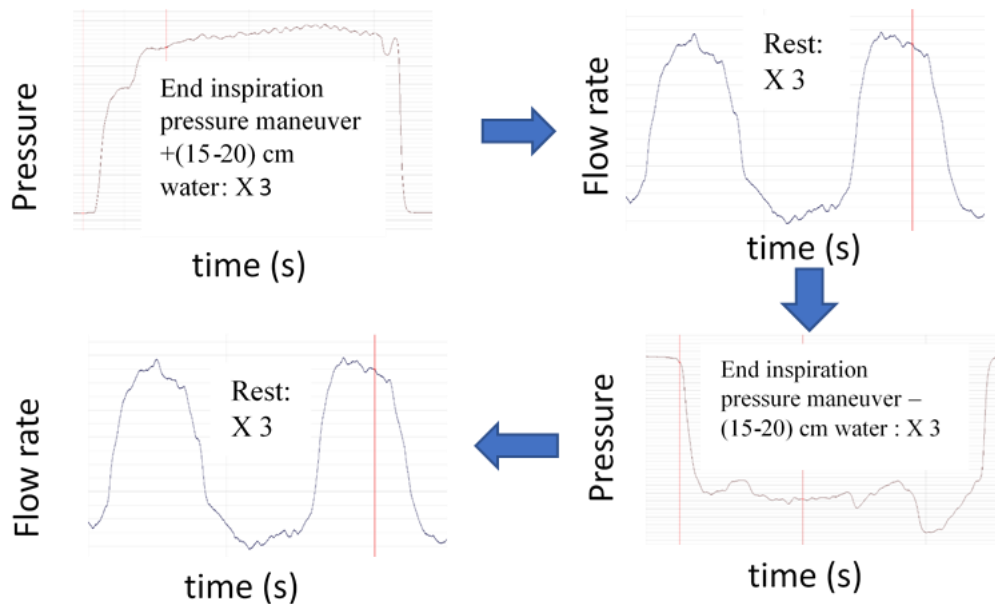
Figure 8 Pressure and flow rate vs. time during end inspiration positive and negative 15-20 cm water pressure.
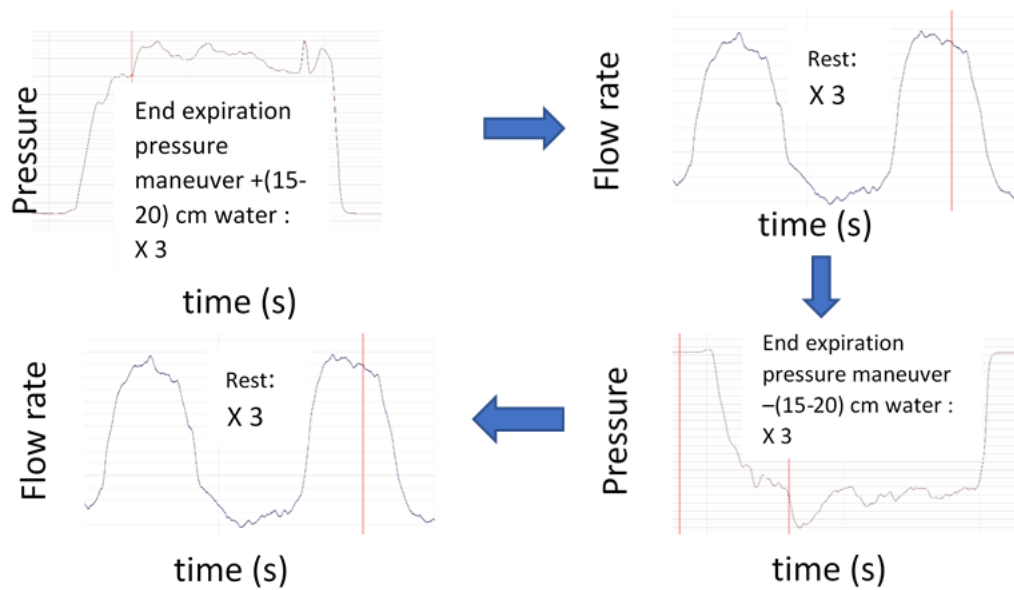
Figure 9 Pressure and flow rate vs. time during end expiration positive and negative 15-20 cm water pressure.
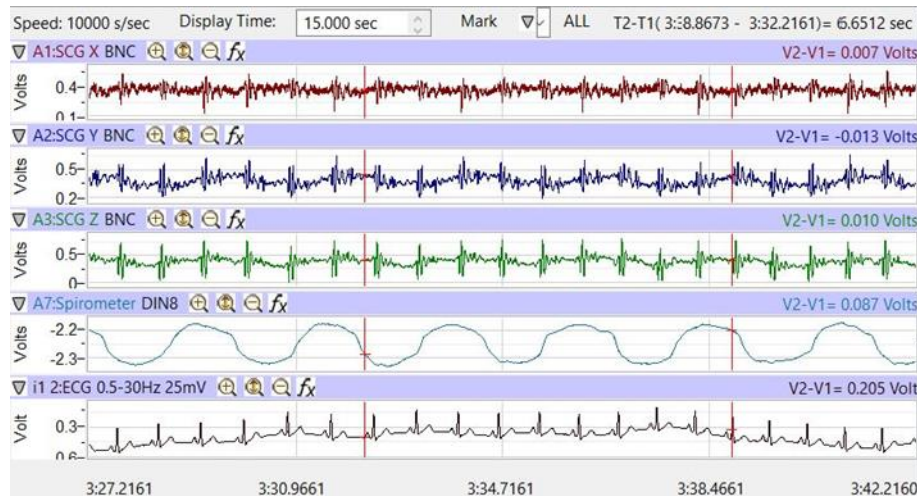
Figure 10 Raw data of SCG X, SCG Y, SCG Z, flow rate and ECG signals (from top to bottom, respectively). Here, SCG in in craniocaudal axis is labeled as SCG X, SCG in lateral axis is labeled as SCG Y and SCG in dorsoventral axis is labeled as SCG Z.

Figure 6 shows pressure and flow rate vs. time during end inspiration positive and negative 2-4 cm water pressure. Figure 7 shows pressure and flow rate vs. time during end expiration positive and negative 2-4 cm water pressure. Figure 8 shows pressure

and flow rate vs. time during end inspiration positive and negative 2-4 cm water pressure. Figure 9 shows pressure and flow rate vs. time during end expiration positive and negative 15-20 cm water pressure. The raw data from the triaxial SCG, ECG, and spirometer flow rate are shown in Figure 10. The sampling rate was 10,000 Hz in this experiment.

Signal processing
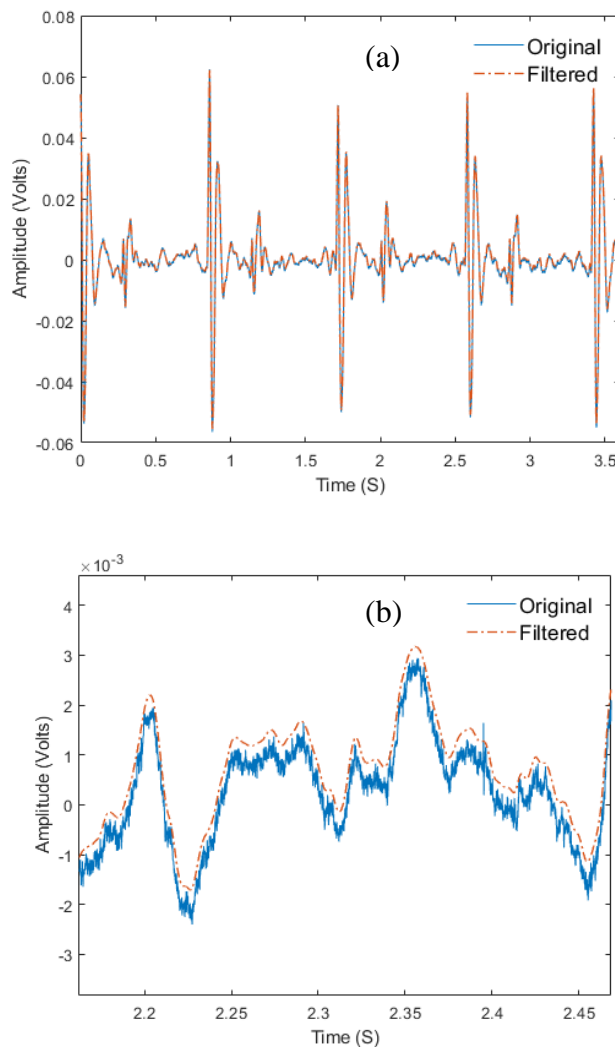
Figure 11 Filtered vs original signal. (a) shows multiple SCG beats ; (b) shows zoomed in view.

After downsampling SCG signals to 1000 Hz, a band pass filter (Chebyshev 2 type) with a cut-off frequency of 0.05–200 Hz was employed to filter the signals. This is done to eliminate background noise as well as baseline drifting caused by breathing and other bodily motions. Figure 11 shows Filtered vs original signal in multiple SCG beats and zoomed in view. The R-R intervals of the simultaneously obtained ECG were used to segment the SCG signal into the SCG events (SCG signals during each heart cycle). To keep it simple and consistent, the beginning and end times of the SCG event were set to be 100 milliseconds before the R wave.

K-medoid clustering

Before clustering, SCG events were downsampled to 500 Hz. An unsupervised machine learning technique known as k-medoid clustering was used to cluster SCG events based on their waveform to reduce SCG variability during normal breathing. The dynamic time warping (DTW) distance was used to cluster the data. Clustering time series based on waveform shape was previously suggested to be more accurate than other approaches.

A common method for comparing two time series is the DTW. The DTW method uses temporal aberrations between two time sequences to achieve an optimum local alignment. A measure of similarity is determined regardless of non-linear variations in time by "warping" the sequences in the time domain.

DTW procedure

The following are the processes for computing the DTW distance between two time series of differing lengths, X and Y.

$$X = \{x_1, x_2, \ldots x_i, \ldots x_n\} \tag{1}$$

$$Y = \{y_1, y_2, \ldots y_j, \ldots y_m\} \tag{2}$$

The lengths of the two signals are n and m, respectively.

The following formula is used to recursively fill this distance matrix:

$$D(i,j) = \delta(x_i, y_j) + min \begin{cases} D(i, j-1) \\ D(i-1, j) \\ D(i-1, j-1) \end{cases} \tag{3}$$

were $\delta(x_i, y_j) = (x_i - y_j)^2$ or $|x_i - y_j|$

An optimal alignment (warping path) $W = \{w_1, w_2, \ldots w_k, \ldots, w_N\}$ is to be found were $w_k = (i, j)$ represent the alignment between i^{th} point of X and j^{th} point of Y.

The optimal warping path is found such that it minimizes,

$$DTW(X,Y) = argmin \sum_{k=1}^{k=N} D(w) \tag{4}$$

where, the warping path should satisfy the following three conditions.

Boundary constraint: $w_1 = (1,1), w_N = (n, m)$

Monotonicity constraint: $w_k = (i, j), w_{k+1} = (i', j')$ were $i' \geq i$ and $j' \geq j$

Continuity constraint: $w_k = (i, j), w_{k+1} = (i', j')$ were $i' \leq i + 1$ and $j' \leq j + 1$

Euclidean

Dynamic Time Warping
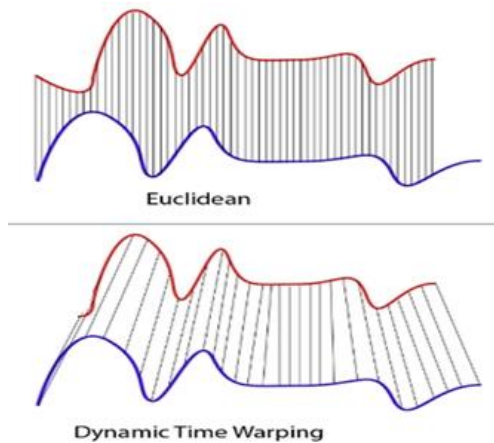
Figure 12 The difference between Euclidean distance and dynamic time warping.
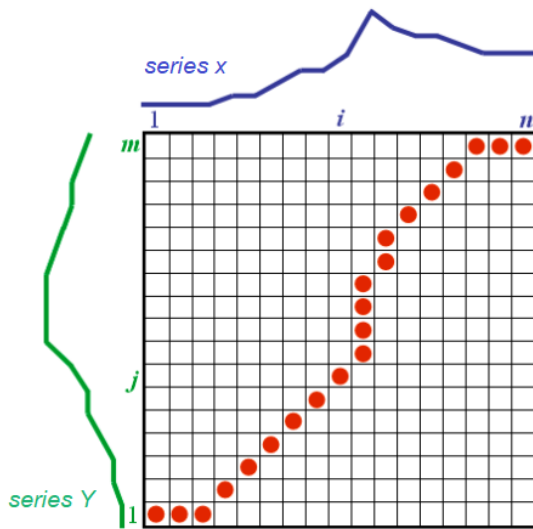
Figure 13 The optimal warping path between signals X and Y to illustrate DTW.

Figure 12 shows the difference between Euclidean distance and dynamic time warping.

Figure 13 shows how DTW algorithm finds distance matrix.

The K-Medoid clustering technique was created in MATLAB. A representative event (medoid) is picked for the cluster instead of a cluster centroid. Medoid is the event in the cluster having the shortest distances to all other events. K-medoid clustering is preferred to K-means clustering because it is less susceptible to outliers.

K-Medoid algorithm

Step 1: Choose inputs: 1) Cluster number $=$ K; 2) The SCG events $\{X_1, X_2, X_3, \dots, X_i \dots, X_N\}$ where N refers to the number of events and each event is a feature vector of signal amplitudes such that $X_i = \{x_1, x_2, x_3, \dots, x_{l_i}\}$.

Step 2: Initialize the medoid for each cluster $C_1, \dots, C_j, \dots C_k$.

Step 3: For each SCG event, X_i, find the nearest cluster medoid C_j (using cross co $-$ relation as the distance measure) and assign X_i to cluster j.

Step 4: After assigning all events to a cluster, use Eq. 5 to update C_j based on the clustered events from the previous step:

$$C_j = argmin_{y \in \{X_{1j}, X_{2j}, ..., X_{ij}, ..., X_{nj}\}} \sum_{i=1}^{n_j} dtw(y, X_{ij}) \tag{5}$$

where Xij is the ith event of cluster j and nj is the number of j events after step 2.

Step 5: Repeat steps 3 and 4 until cluster assignments do not change.

The ideal number of clusters was determined using the elbow method. A small number of clusters were chosen to limit intra-cluster variance. Equation 6 calculates the average sum of distances (SOD) between each event and its cluster medoid, which reveals intra-cluster variability.

$$SOD = \frac{1}{N} \sum_{j=1}^{k} \sum_{i=1}^{n_j} dtw(C_j, X_{ij}) \tag{6}$$

Here, N is the total number of events, X_{ij} is the ith event for cluster medoid C_j, and n_j is the number of events for C_j.
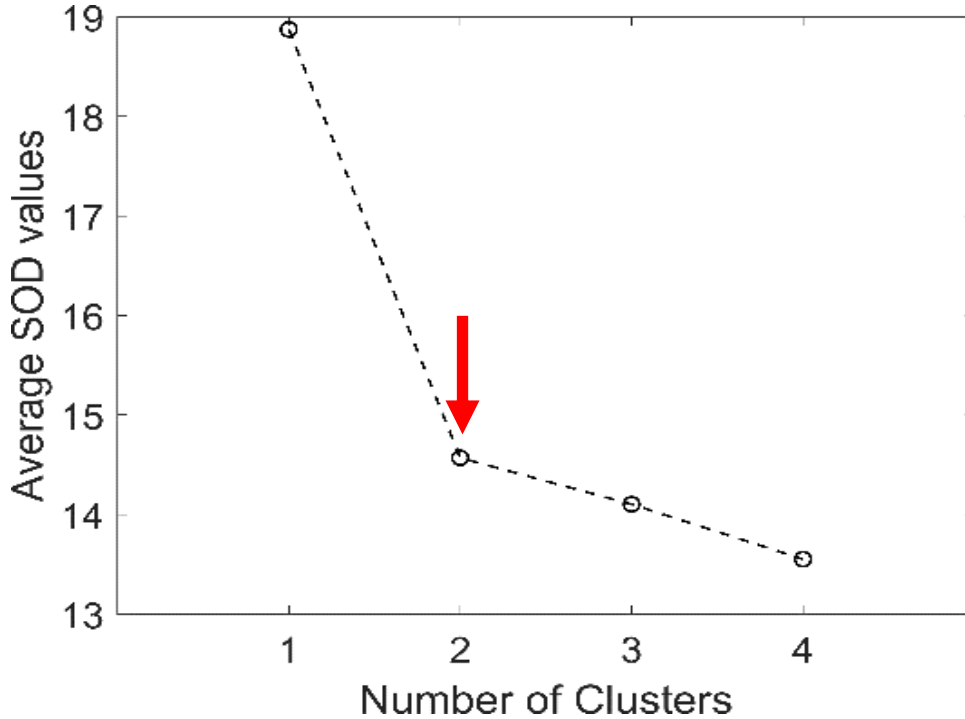
Figure 14 To demonstrate the elbow method, average SOD for different numbers of clusters was calculated.

Figure 14 shows the average SOD for various cluster sizes. When the number of clusters was 2, an elbow form was found, which is consistent with earlier research (Sandler et al., 2021; Sandler et al., 2021; Hassan et al., 2021) . With the fewest number of clusters, it can be argued that two clusters would result in acceptable intra-cluster variance.

Decision Boundary

After clustering, a support vector machine (SVM) was used to create a decision boundary to illustrate how accurately the two clusters are separated. By finding a hyperplane for the features, the SVM algorithm maximizes the margin between the two classes. A decision boundary can be defined (for linearly separable data) as $w. x_i + b = 0$ and the margins are defined using the hyperplanes $w. x_i + b = \pm 1$. Marginal data points on the boundary are known as the support vectors. The weight vector, feature vector, and bias are represented by w, x, and b, respectively. The aim of SVM is to maximize the decision margin $d = \frac{1}{\|w\|}$. Figure 15 shows the SVM hyperplane and margin.
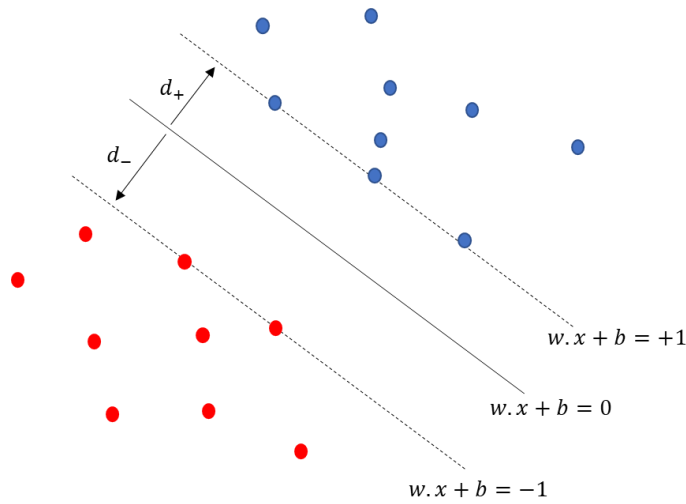
Figure 15 SVM hyperplane showing the decision boundary and margin between the classes.

Statistical Analysis

In this dissertation, the waveform parameters are compared between different physiological states. To calculate the statistical significance of parameter changes, the paired t-test was used.

Results and discussion

In Figure 17, the lung volume change versus flow rate plot for two participants shows the cluster distribution and decision boundary of SCG events. The following equation 7 was used to calculate the decision boundary's accuracy.

$$Accuracy = \frac{(TP+TN)}{(TP+FP+FN+TN)} \tag{7}$$

A simplified lung volume waveform with the four respiratory phases is shown in Figure 16. SCG clustering appears to be related to respiration, as seen in Figure 17, and the two clusters were well separated with high accuracy. Cluster 1 and cluster 2 SCG events are represented by blue '∇' triangles and red 'o' circles, respectively.

Clusters are not separated solely on the basis of respiratory flow rate or lung volume, according to these results.
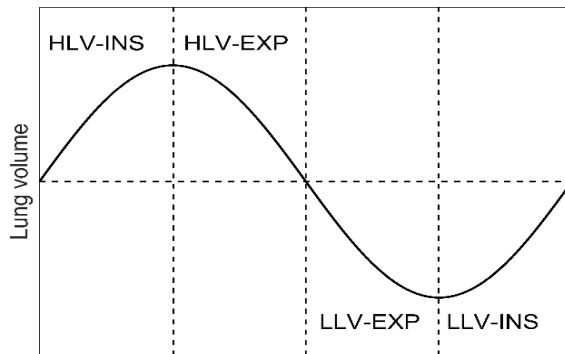
Figure 16 In a simplified waveform of lung volume, the four respiratory phases are labeled.

(a) Accuracy: 0.9844

(b) Accuracy: 0.9836
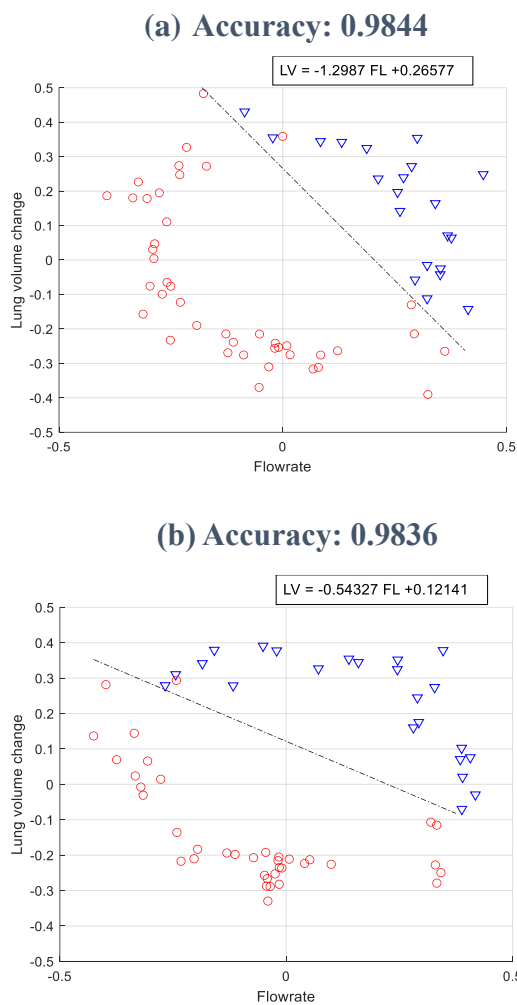
Figure 17 Cluster distribution in the lung volume vs flow rate plane for 2 subjects during 1 minute of data recordings.

Time and frequency domain features

The intra-cluster DTW distance was utilized to measure how dissimilar two waveform sets are. DTW distances are used in Equation 8 to calculate intra-cluster variability.

$$Intra - cluster\ variability = \frac{1}{n_1+n_2}\left[\sum_{i=1}^{n_1} dtw(C_1, X_{i1}) + \sum_{i=1}^{n_2} dtw(C_2, X_{i2})\right] \quad (8)$$

$$Inter - cluster\ variability = \frac{1}{n_1+n_2}\left[\sum_{i=1}^{n_1} dtw(C_2, X_{i1}) + \sum_{i=1}^{n_2} dtw(C_1, X_{i2})\right] \quad (9)$$
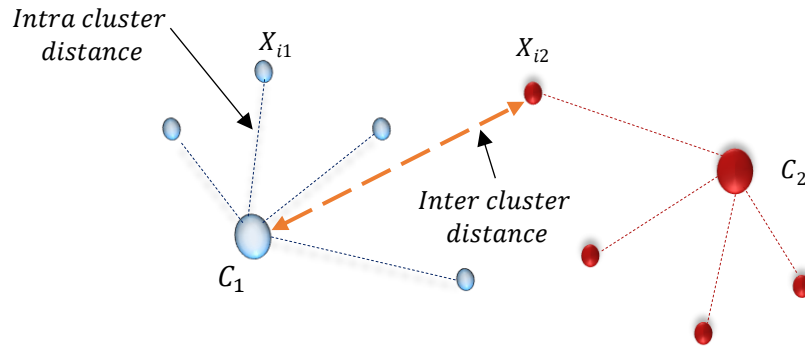
Figure 18 Intra and inter cluster variability (Azad, 2020).
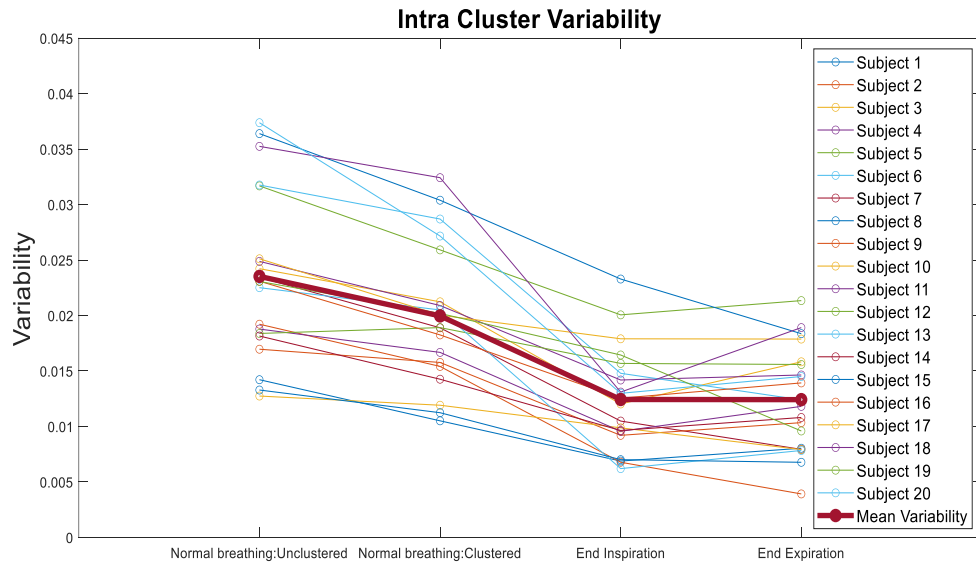
Figure 19 Intra-cluster variability during normal breathing and breath holding.

Table 1 Changes in intra-cluster variability. The study subjects' mean and standard deviation (SD) are reported. There was a decrease with clustering (p<0.05) and a further decrease with breath hold (p<0.05).

Change in intra-cluster variability	Mean (%)	SD (%)
(After clustering -before clustering)/ before clustering	-15	7
(End inspiration BH- Normal breathing unclustered)/Normal breathing unclustered	-52	16
(End Expiration BH- Normal breathing unclustered)/Normal breathing unclustered	-52	17

Inter and intra cluster variability is depicted in Equation 8, 9 and Figure 18. Here, X_{i1} and X_{i2} are the ith SCG event of cluster 1 and cluster 2, respectively. C_1 and C_2 are the respective medoids of the 2 clusters. $n_1\ and\ n_2$ are cluster 1 and 2 total number of events, respectively. Low intra-cluster DTW distance indicates more homogeneous groupings. High inter-clustere variability indicates better cluster separation.

The decrease in intra-cluster variability between the un-clustered normal breathing, clustered normal breathing, BH end inspiration, and BH end expiration states is shown in Figure 19 and table 1. When comparing clustered normal breathing to un-clustered normal breathing, the results demonstrated a 15% reduction in variability (p<0.05). In comparison to the un-clustered normal breathing condition, there was a

52% (p<0.05) drop in variability for end inspiration and a 52% (p<0.05) decrease in variability for end expiration. The high SD indicates a lot of inter-subject variation..
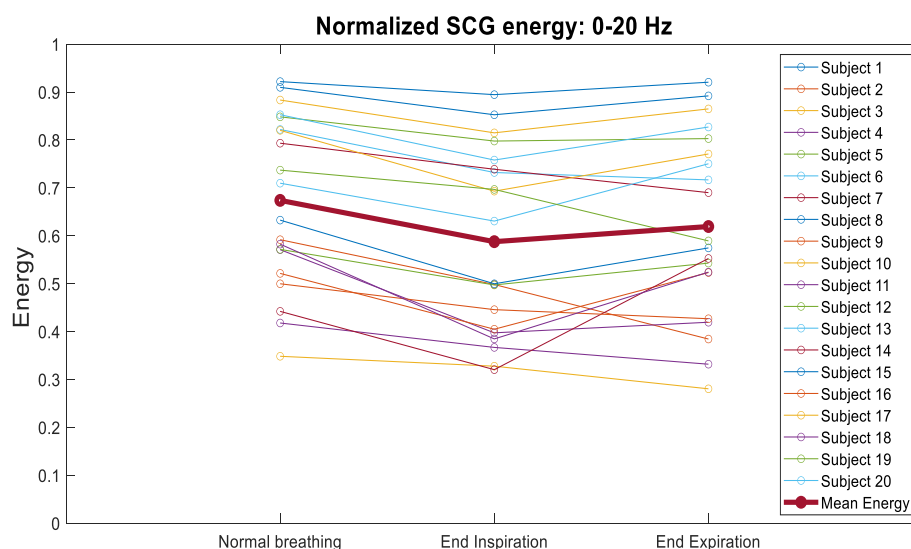
Figure 20 The SCG energy in the 0 –20 Hz (normalized by energy in the 0-50 Hz) during normal breathing and breath holding.

Table 2 In the 0-20 Hz frequency, there is a change in normalized SCG energy. The energy dropped with breath hold (p<0.05).

Change in the energy in the 0-20 Hz for all subjects	Mean (%)	SD (%)
(End inspiration BH- Normal breathing)/Normal breathing	-14	9
(End Expiration BH- Normal breathing)/Normal breathing	-9	13

The energy of the SCG in the 0-20 Hz range was also investigated, as previous research had suggested that this feature could be useful [Gamage, 2020]. The energy in the 0-50 Hz band was used to equalize this energy. The shift in normalized energy in the 0-20 Hz range is depicted in Figure 20 and Table 2. When compared to normal

23

breathing, the study individuals saw a 14% (p<0.05) decrease for end inspiration BH and a 9% (p<0.05) decrease in end expiration BH.

Heart rate

The heart rate was calculated and compared during end inspiration BH, end expiration BH, and the 30 seconds before and after both BH. Table 3 shows the changes in HR. When compared to before and after BH, end inspiration BH resulted in a 9% and 11% (p<0.05) decline in heart rate, respectively. In addition, during end expiration BH, heart rates reduced by an average of 5% and 7% (p<0.05) compared to before and after BH, respectively.

Table 3 Heart rate change. The heart rate decreased with breath hold (p<0.05).

Change in HR during BH for all subjects	Mean (%)	SD (%)
(End inspiration BH- before BH)/before BH	-9	6
(End inspiration BH- after BH)/after BH	-11	6
(End expiration BH- before BH)/before BH	-5	8
(End expiration BH- after BH)/after BH	-7	8

Heart rate variability feature

The HRV's spectral power in the 0.15–0.4 Hz band, often known as the high-frequency region, was calculated (HF). The properties and frequency ranges of heart rate variability are shown in Table 4. The spectral energy variations in HF band between the two breathing conditions are shown in Figure 21 and Table 5. When compared to

normal breathing, the results demonstrated a 59% (p<0.05) decrease in this energy during end inspiration BH and a 64% (p<0.05) decrease during end expiration BH. This drop is most likely due to the fact that breathing frequency falls within this range. Because the HRV linked with breathing (a condition called as respiratory sinuous arrhythmia) is reduced with BH, this frequency band is likely to have less energy.

Table 4 Heart rate variability frequency ranges.

Heart Rate Variability (HRV)	LF	Spectral power in 0.04–0.15 Hz
	HF	Spectral power in 0.15–0.4 Hz
	VHF	Total spectral power in 0.4–1.0 Hz
	TP	Total spectral power in 0–0.4 Hz
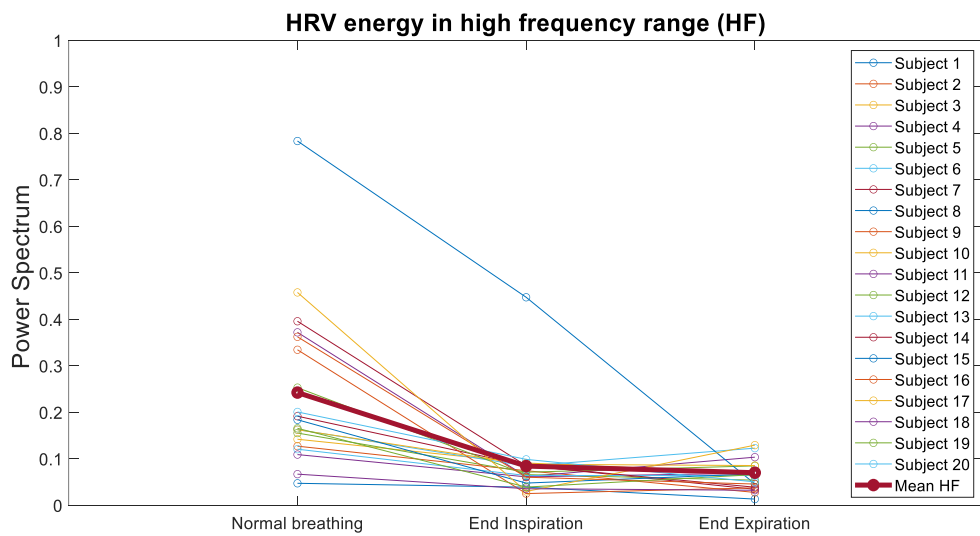
Figure 21 HRV energy in high frequency range (HF) during normal breathing and breath holding.

Table 5 HRV energy change in the high frequency range (HF). With breath held, there was a significant drop. (p<0.05).

Energy change in the HF band for all subjects	Mean (%)	SD (%)
(End inspiration BH- Normal breathing)/Normal breathing	-59	20
(End Expiration BH- Normal breathing)/Normal breathing	-64	21

Effect of intrathoracic pressure

Figure 22 and table 6 shows the intra-cluster variability between the BH end inspiration, positive 2-4 cm water pressure after end inspiration, negative 2-4 cm water pressure after end inspiration, positive 15-20 cm water pressure after end
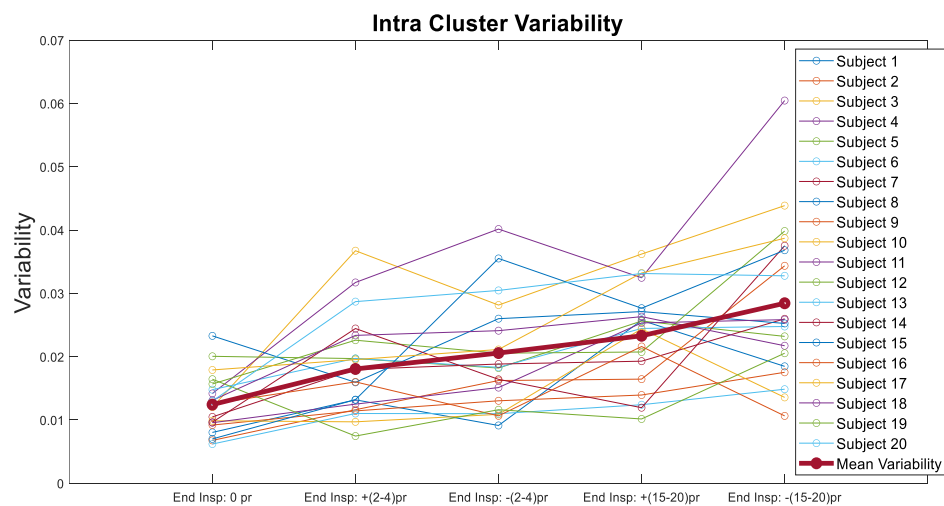
Figure 22 Intra-cluster variability during end inspiration breath holding at varying airway pressure.

Table 6 Intra-cluster variability change. There was an increase with increasing positive and negative intrathoracic pressure after end inspiration breath holding.

Change in intra-cluster variability due to change in intrathoracic pressure	Mean (%)
(End inspiration positive 2-4 cm water- End inspiration)/End inspiration zero pressure	54
(End inspiration negative 2-4 cm water- End inspiration)/End inspiration zero pressure	81
(End inspiration positive 15-20 cm water- End inspiration)/End inspiration zero pressure	105
(End inspiration negative 15-20 cm water- End inspiration)/End inspiration zero pressure	154

inspiration, negative 15-20 cm water pressure after end inspiration states. Results showed an average 54% increase in variability for positive 2-4 cm water pressure after end inspiration compared to BH end inspiration. Also, it was found that there was an average 81% increase in variability for positive 2-4 cm water pressure after end inspiration, 105% increase in variability for positive 15-20 cm water pressure after end inspiration and a 154% increase in variability for negative 15-20 cm water pressure after end inspiration, as compared to the BH end inspiration state.

Figure 23 and table 7 shows the change in intra-cluster variability between the BH end expiration, positive 2-4 cm water pressure after end expiration, negative 2-4 cm water pressure after end expiration, positive 15-20 cm water pressure after end expiration, negative 15-20 cm water pressure after end expiration states. Results showed an average 56% increase in variability for positive 2-4 cm water pressure after end expiration compared to BH end inspiration. Also, it was found that there was an

average 62% increase in variability for positive 2-4 cm water pressure after end expiration, 186% increase (p>0.05) in variability for positive 15-20 cm water pressure after end expiration and a 121% increase (p>0.05) in variability for negative 15-20 cm water pressure after end expiration, as compared to the BH end expiration state.
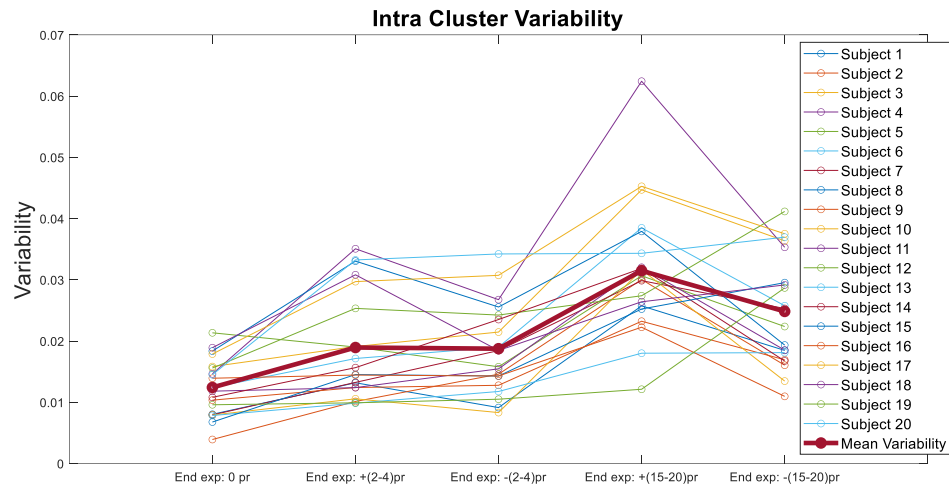
Figure 23 Intra-cluster variability during end expiration breath holding at varying airway pressure.

Table 7 Intra-cluster variability change. There was an increase with increasing positive and negative intrathoracic pressure after end expiration breath holding.

Change in intra-cluster variability due to change in intrathoracic pressure	Mean (%)
(End inspiration positive 2-4 cm water- End inspiration)/End inspiration zero pressure	56
(End inspiration negative 2-4 cm water- End inspiration)/End inspiration zero pressure	62
(End inspiration positive 15-20 cm water- End inspiration)/End inspiration zero pressure	186
(End inspiration negative 15-20 cm water- End inspiration)/End inspiration zero pressure	121

Inter-cluster variability between normal breathing and breath holding

Figure 24 shows the inter-cluster variability between cluster 1 and BH for all subjects separately. Here, blue rectangle shows inter cluster variability between cluster 1 and BH at end inspiration. Red rectangle shows inter cluster variability between cluster 1 and BH at end expiration. Results showed inter cluster variability between
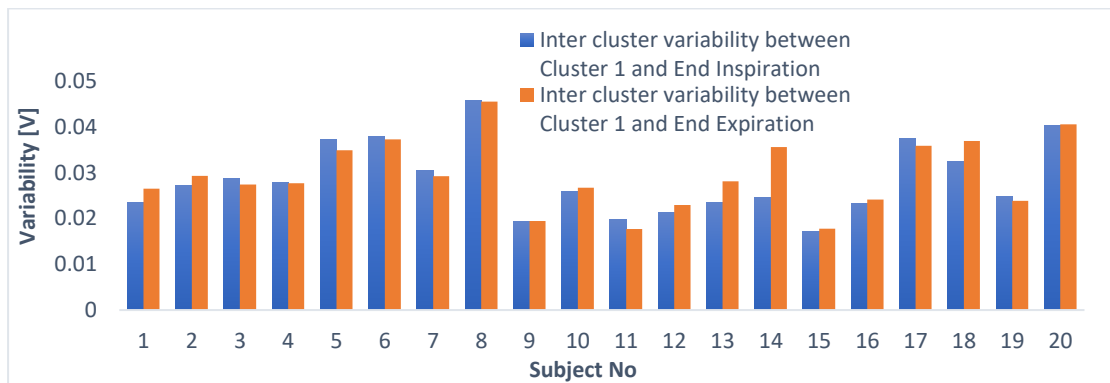
Figure 24 Inter-cluster variability between cluster 1 and breath holding at zero airway pressure.

cluster 1 and end inspiration was lower than inter cluster variability between cluster 1 and end expiration in most of the subjects. This confirms that cluster 1 is more similar to breath holding at end inspiration (at high lung volume).

Table 8 Inter-cluster variability change. There was a decrease in inter-cluster variability between cluster 1 and end inspiration compared to cluster 1 and end expiration ($p<0.05$).

Inter-cluster variability	Mean (mV)
Cluster 1 and end inspiration zero airway pressure	**28.4**
Cluster 1 and end expiration zero airway pressure	29.4

Table 8 shows the average inter-cluster variability for all subjects between cluster 1 and BH. Here, it was found that average inter-cluster variability for all subjects

between cluster 1 and end inspiration was 28.4 mV (p<0.05). Also, the inter-cluster variability for all subjects between cluster 1 and end expiration was 29.4 mV (p<0.05). The results from Figure 24 and Table 8 showed cluster 1 was more similar to end inspiration than end expiration in 11 of the 20 subjects.

Figure 25 shows the inter-cluster variability between cluster 2 and BH for all subjects separately. Here, blue rectangle shows inter cluster variability between cluster
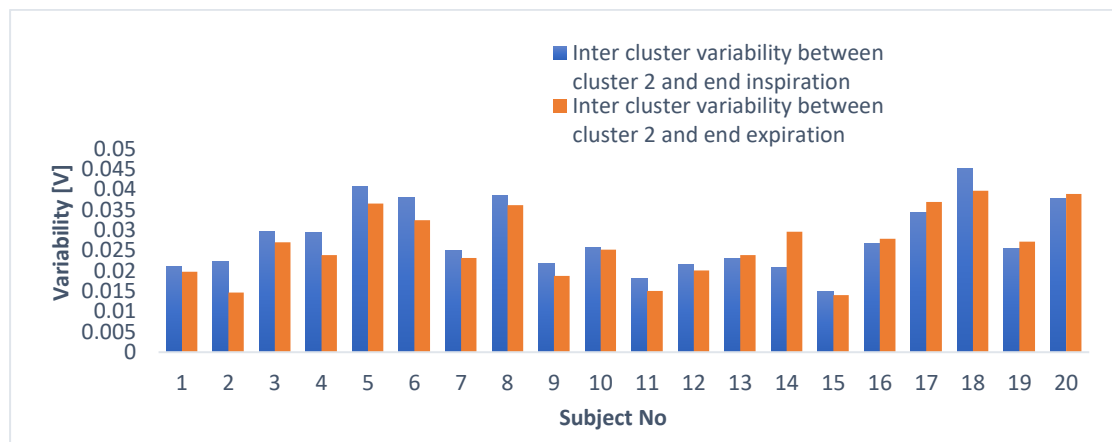
Figure 25 Inter-cluster variability between cluster 2 and breath holding at zero airway pressure.

2 and BH at end inspiration. Red rectangle shows inter cluster variability between cluster 2 and BH at end expiration. Results showed inter cluster variability between cluster 2 and end expiration was lower than inter cluster variability between cluster 2 and end inspiration in 14 of the 20 subjects.

Table 9 Inter-cluster variability change. There was a decrease in inter-cluster variability between cluster 2 and end expiration compared to cluster 2 and end inspiration (p<0.05).

Inter-cluster variability	Mean (mV)
Cluster 2 and end inspiration zero airway pressure	28.0
Cluster 2 and end expiration zero airway pressure	**26.5**

Table 9 shows the average inter-cluster variability for all subjects between cluster 2 and BH. Here, it was found that average inter-cluster variability for all subjects between cluster 2 and end inspiration was 28.0 mV (p<0.05). Also, the inter-cluster variability for all subjects between cluster 2 and end expiration was 26.5 mV (p<0.05). The results from Figure 25 and Table 9 showed cluster 2 was more similar to end expiration than end inspiration based on these findings.

Inter-cluster variability between normal breathing and breath holding at positive 2-4 cm water pressure

Figure 26 Inter-cluster variability between cluster 1 and breath holding at positive 2-4 cm water.

Table 10 Inter-cluster variability change. There was a decrease in inter-cluster variability between cluster 1 and end inspiration positive 2-4 cm water pressure compared to cluster 1 and end expiration positive 2-4 cm water pressure (p<0.05).

Inter-cluster variability	Mean (mV)
Cluster 1 and end inspiration positive 2-4 cm water	**29.3**
Cluster 1 and end expiration positive 2-4 cm water	29.9

Figure 26 shows the inter-cluster variability between cluster 1 and BH at positive 2-4 cm water pressure for all subjects separately. Here, blue rectangle shows inter cluster variability between cluster 1 and BH at end inspiration positive 2-4 cm water pressure. Red rectangle shows inter cluster variability between cluster 1 and BH at end expiration positive 2-4 cm water pressure. Results showed inter cluster variability between cluster 1 and end inspiration positive 2-4 cm water pressure was lower than inter cluster variability between cluster 1 and end expiration positive 2-4 cm water pressure in most of the subjects.

Table 10 shows the average inter-cluster variability for all subjects between cluster 1 and BH at positive 2-4 cm water pressure. Here, it was found that average inter-cluster variability for all subjects between cluster 1 and end inspiration positive 2-4 cm water pressure was 29.3 mV ($p<0.05$). Also, the inter-cluster variability for all subjects between cluster 1 and end expiration positive 2-4 cm water pressure was 29.9 mV ($p<0.05$). The results from Figure 26 and Table 10 showed cluster 1 was more similar to end inspiration positive 2-4 cm water pressure than end expiration positive 2-4 cm water pressure based on these findings.

Figure 27 shows the inter-cluster variability between cluster 2 and BH at positive 2-4 cm water pressure for all subjects separately. Here, blue rectangle shows inter cluster variability between cluster 2 and BH at end inspiration positive 2-4 cm water pressure. Red rectangle shows inter cluster variability between cluster 2 and BH at end expiration positive 2-4 cm water pressure. Results showed inter cluster variability between cluster 2 and end inspiration positive 2-4 cm water pressure was higher than inter cluster variability between cluster 2 and end expiration positive 2-4 cm water pressure in most of the subjects.

Figure 27 Inter-cluster variability between cluster 2 and breath holding at positive 2-4 cm water.

Table 11 shows the average inter-cluster variability for all subjects between cluster 2 and BH at positive 2-4 cm water pressure. Here, it was found that average inter-cluster variability for all subjects between cluster 2 and end inspiration positive 2-4 cm water pressure was 29.5 mV ($p < 0.05$). Also, the inter-cluster variability for all subjects between cluster 2 and end expiration positive 2-4 cm water pressure was 28.1 mV ($p < 0.05$). The results from Figure 27 and Table 11 showed cluster 2 was more similar to end expiration positive 2-4 cm water pressure than end inspiration positive 2-4 cm water pressure based on these findings.

Table 11 Inter-cluster variability change. There was a decrease in inter-cluster variability between cluster 2 and end expiration positive 2-4 cm water pressure compared to cluster 2 and end inspiration positive 2-4 cm water pressure ($p < 0.05$).

Inter-cluster variability	Mean (mV)
Cluster 2 and end inspiration positive 2-4 cm water	29.5
Cluster 2 and end expiration positive 2-4 cm water	**28.1**

Inter-cluster variability between normal breathing and breath holding at negative 2-4 cm water pressure

Figure 28 shows the inter-cluster variability between cluster 1 and BH at negative 2-4 cm water pressure for all subjects separately. Here, blue rectangle shows inter cluster variability between cluster 1 and BH at end inspiration negative 2-4 cm water pressure. Red rectangle shows inter cluster variability between cluster 1 and BH at end expiration negative 2-4 cm water pressure. Results showed inter cluster variability between cluster 1 and end inspiration negative 2-4 cm water pressure was lower than inter cluster variability between cluster 1 and end expiration negative 2-4 cm water pressure in most of the subjects although it was opposite in some subjects as after end inspiration creating negative pressure was challenging for them .

Figure 28 Inter-cluster variability between cluster 1 and breath holding at negative 2-4 cm water.

Table 12 Inter-cluster variability change between cluster 1 and end inspiration negative 2-4 cm water pressure and cluster 1 and end expiration negative 2-4 cm water pressure ($p < 0.05$).

Inter-cluster variability	Mean (mV)
Cluster 1 and end inspiration negative 2-4 cm water	32.7
Cluster 1 and end expiration negative 2-4 cm water	**31.1**

Table 12 shows the average inter-cluster variability for all subjects between cluster 1 and BH at negative 2-4 cm water pressure. Here, it was found that average inter-cluster variability for all subjects between cluster 1 and end inspiration negative 2-4 cm water pressure was 32.7 mV ($p<0.05$). Also, the inter-cluster variability for all subjects between cluster 1 and end expiration negative 2-4 cm water pressure was 31.1 mV ($p<0.05$). There was no clear pattern found for this case because of lack experimental control in some subjects .

Figure 29 shows the inter-cluster variability between cluster 2 and BH at negative 2-4 cm water pressure for all subjects separately. Here, blue rectangle shows inter cluster variability between cluster 2 and BH at end inspiration negative 2-4 cm water pressure. Red rectangle shows inter cluster variability between cluster 2 and BH at end expiration negative 2-4 cm water pressure. Results showed inter cluster variability between cluster 2 and end inspiration negative 2-4 cm water pressure was higher than inter cluster variability between cluster 2 and end expiration negative 2-4 cm water pressure in most of the subjects.
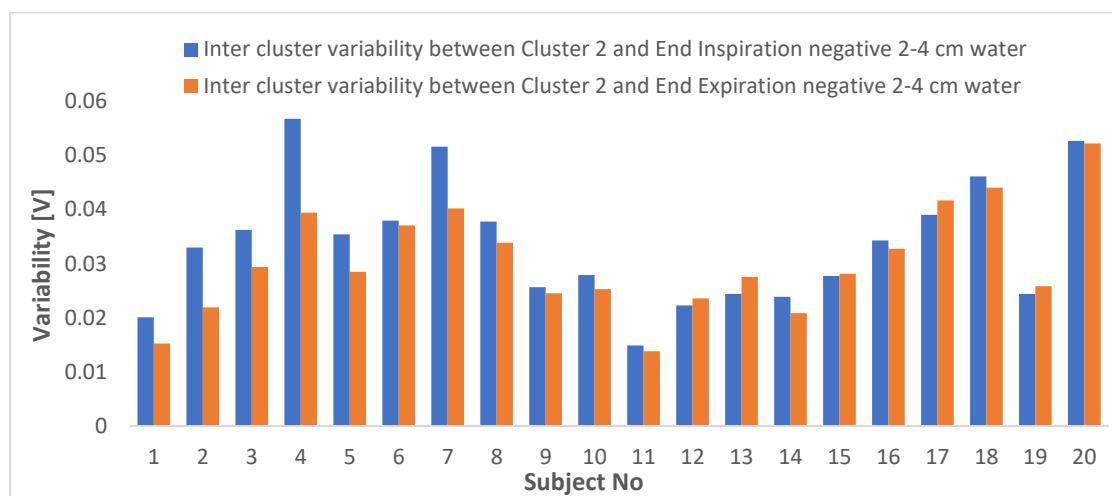
Figure 29 Inter-cluster variability between cluster 2 and breath holding at negative 2-4 cm water.

Table 13 shows the average inter-cluster variability for all subjects between cluster 2 and BH at negative 2-4 cm water pressure. Here, it was found that average inter-cluster variability for all subjects between cluster 2 and end inspiration negative 2-4 cm water pressure was 33.6 mV ($p<0.05$). Also, the inter-cluster variability for all subjects between cluster 2 and end expiration negative 2-4 cm water pressure was 30.3 mV ($p<0.05$). The results from Figure 29 and Table 13 showed cluster 2 was more similar to end expiration negative 2-4 cm water pressure than end inspiration negative 2-4 cm water pressure based on these findings.

Table 13 Inter-cluster variability change. There was a decrease in inter-cluster variability between cluster 2 and end expiration negative 2-4 cm water pressure compared to cluster 2 and end inspiration negative 2-4 cm water pressure ($p<0.05$).

Inter-cluster variability	Mean (mV)
Cluster 2 and end inspiration negative 2-4 cm water	33.6
Cluster 2 and end expiration negative 2-4 cm water	**30.3**

Inter-cluster variability between normal breathing and breath holding at positive 15-20 cm water pressure

Figure 30 shows the inter-cluster variability between cluster 1 and BH at positive 15-20 cm water pressure for all subjects separately. Here, blue rectangle shows inter cluster variability between cluster 1 and BH at end inspiration positive 15-20 cm water pressure. Red rectangle shows inter cluster variability between cluster 1 and BH at end expiration positive 15-20 cm water pressure. Results showed inter cluster variability between cluster 1 and end inspiration positive 15-20 cm water pressure was lower than

inter cluster variability between cluster 1 and end expiration positive 15-20 cm water pressure in most of the subjects.
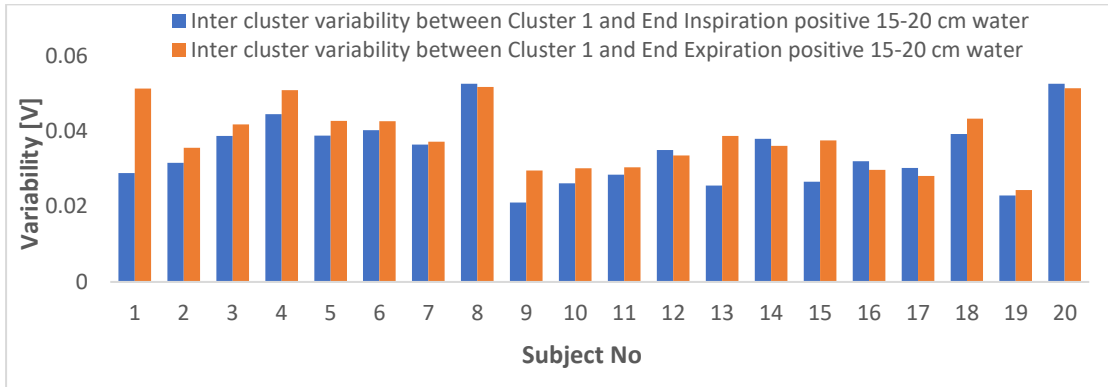
Figure 30 Inter-cluster variability between cluster 1 and breath holding at positive 15-20 cm water.

Table 14 Inter-cluster variability change. There was a decrease in inter-cluster variability between cluster 1 and end inspiration positive 15-20 cm water pressure compared to cluster 1 and end expiration positive 15-20 cm water pressure (p<0.05).

Inter-cluster variability	Mean (mV)
Cluster 1 and end inspiration positive 15-20 cm water	**34.5**
Cluster 1 and end expiration positive 15-20 cm water	38.4

Table 14 shows the average inter-cluster variability for all subjects between cluster 1 and BH at positive 15-20 cm water pressure. Here, it was found that average inter-cluster variability for all subjects between cluster 1 and end inspiration positive 15-20 cm water pressure was 34.5 mV (p<0.05). Also, the inter-cluster variability for all subjects between cluster 1 and end expiration positive 15-20 cm water pressure was 38.4 mV (p<0.05). The results from Figure 30 and Table 14 showed cluster 1 was more similar to end inspiration positive 15-20 cm water pressure than end expiration positive 15-20 cm water pressure based on these findings.

37

Figure 31 shows the inter-cluster variability between cluster 2 and BH at positive 15-20 cm water pressure for all subjects separately. Here, blue rectangle shows inter cluster variability between cluster 2 and BH at end inspiration positive 15-20 cm water pressure. Red rectangle shows inter cluster variability between cluster 2 and BH at end expiration positive 15-20 cm water pressure. Results showed inter cluster variability between cluster 2 and end inspiration positive 15-20 cm water pressure was higher than inter cluster variability between cluster 2 and end expiration positive 15-20 cm water pressure in most of the subjects although it was opposite in some subjects as after end expiration creating positive pressure was challenging for them.
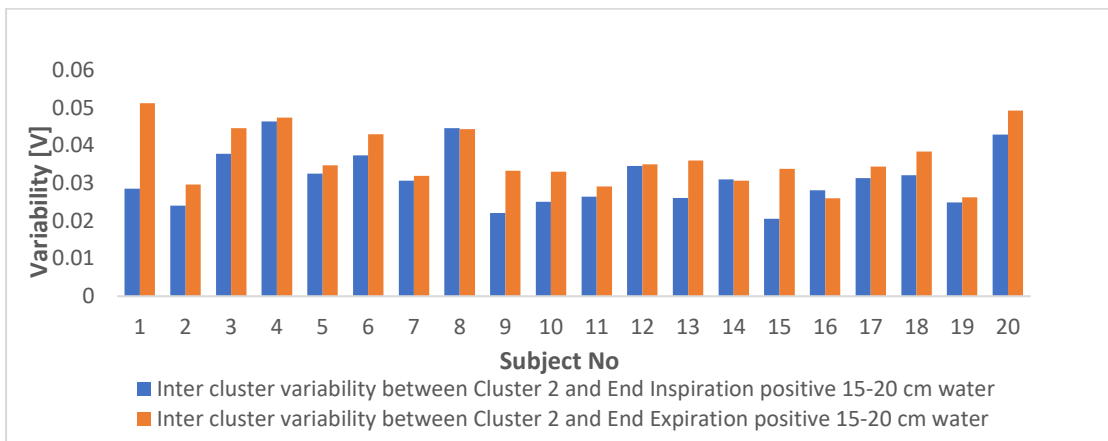
Figure 31 Inter-cluster variability between cluster 2 and breath holding at positive 15-20 cm water.

Table 15 shows the average inter-cluster variability for all subjects between cluster 2 and BH at positive 15-20 cm water pressure. Here, it was found that average inter-cluster variability for all subjects between cluster 2 and end inspiration positive 15-20 cm water pressure was 31.3 mV (p<0.05). Also, the inter-cluster variability for all subjects between cluster 2 and end expiration positive 15-20 cm water pressure was 36.6 mV (p<0.05). The results from Figure 31 and Table 15 showed no clear pattern for this case because of lack experimental control in some subjects.

Table 15 Inter-cluster variability change. There was a decrease in inter-cluster variability between cluster 2 and end expiration positive 15-20 cm water pressure compared to cluster 2 and end inspiration positive 15-20 cm water pressure (p<0.05).

Inter-cluster variability	Mean (mV)
Cluster 2 and end inspiration positive 15-20 cm water	**31.3**
Cluster 2 and end expiration positive 15-20 cm water	36.6

Inter-cluster variability between normal breathing and breath holding at negative 15-20 cm water pressure

Figure 32 shows the inter-cluster variability between cluster 1 and BH at negative 15-20 cm water pressure for all subjects separately. Here, blue rectangle shows inter cluster variability between cluster 1 and BH at end inspiration negative 15-20 cm water pressure. Red rectangle shows inter cluster variability between cluster 1 and BH at end expiration negative 15-20 cm water pressure. Results showed inter cluster variability between cluster 1 and end inspiration negative 15-20 cm water pressure was lower than inter cluster variability between cluster 1 and end expiration negative 15-20 cm water pressure in most of the subjects although it was opposite in some subjects as after end inspiration creating negative pressure was challenging for them .
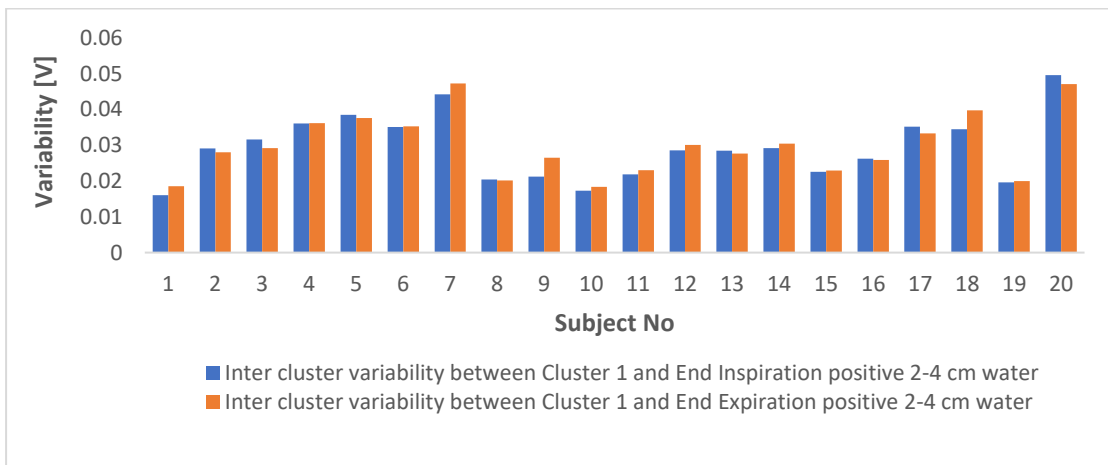

Figure 32 Inter-cluster variability between cluster 1 and breath holding at negative 15-20 cm water.

Table 16 Inter-cluster variability change. There was a decrease in inter-cluster variability between cluster 1 and end inspiration negative 15-20 cm water pressure compared to cluster 1 and end expiration negative 15-20 cm water pressure ($p<0.05$).

Inter-cluster variability	Mean (mV)
Cluster 1 and end inspiration negative 15-20 cm water	37.9
Cluster 1 and end expiration negative 15-20 cm water	**36.4**

Table 16 shows the average inter-cluster variability for all subjects between cluster 1 and BH at negative 15-20 cm water pressure. Here, it was found that average inter-cluster variability for all subjects between cluster 1 and end inspiration negative 15-20 cm water pressure was 37.9 mV ($p<0.05$). Also, the inter-cluster variability for all subjects between cluster 1 and end expiration negative 15-20 cm water pressure was 36.4 mV ($p<0.05$). There was no clear pattern found for this case because of lack experimental control in some subjects .

Figure 32 shows the inter-cluster variability between cluster 2 and BH at negative 15-20 cm water pressure for all subjects separately. Here, blue rectangle shows inter cluster variability between cluster 2 and BH at end inspiration negative 15-20 cm water pressure. Red rectangle shows inter cluster variability between cluster 2 and BH at end expiration negative 15-20 cm water pressure. Results showed inter cluster variability between cluster 2 and end inspiration negative 15-20 cm water pressure was higher than inter cluster variability between cluster 2 and end expiration negative 15-20 cm water pressure in most of the subjects.
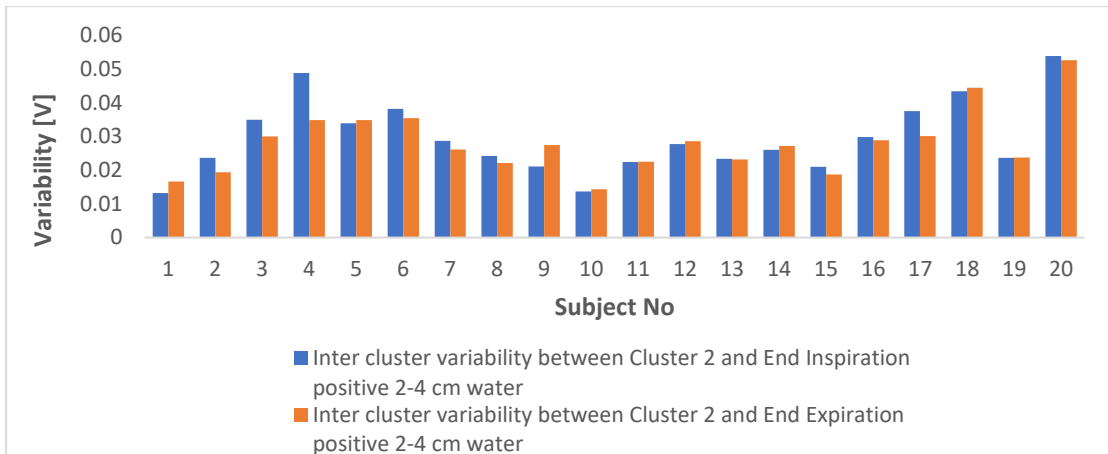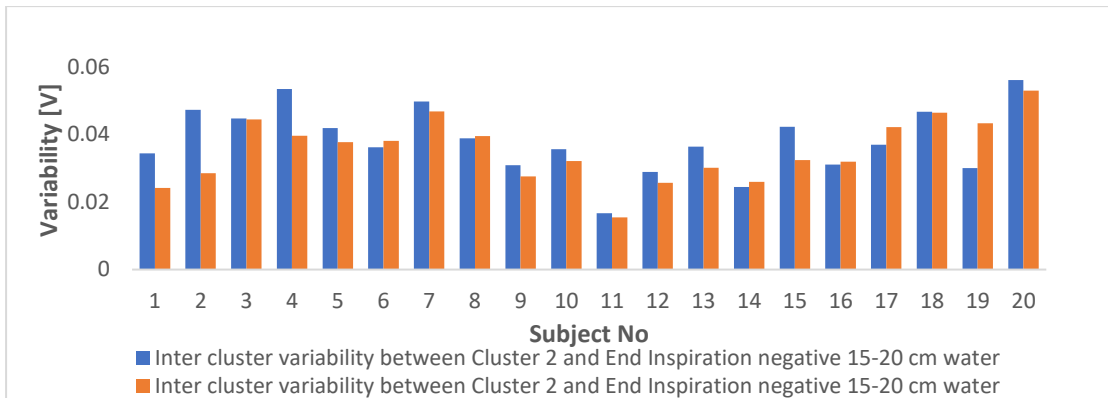
Figure 33 Inter-cluster variability between cluster 2 and breath holding at negative 15-20 cm water.

Table 17 shows the average inter-cluster variability for all subjects between cluster 2 and BH at negative 15-20 cm water pressure. Here, it was found that average inter-cluster variability for all subjects between cluster 2 and end inspiration negative 15-20 cm water pressure was 38.1 mV ($p<0.05$). Also, the inter-cluster variability for all subjects between cluster 2 and end expiration negative 15-20 cm water pressure was 35.2 mV ($p<0.05$). The results from Figure 33 and Table 17 showed cluster 2 was more similar to end expiration negative 15-20 cm water pressure than end inspiration negative 15-20 cm water pressure based on these findings.

Table 17 Inter-cluster variability change. There was a decrease in inter-cluster variability between cluster 2 and end expiration negative 15-20 cm water pressure compared to cluster 2 and end inspiration negative 15-20 cm water pressure ($p<0.05$).

Inter-cluster variability	Mean (mV)
Cluster 2 and end inspiration negative 15-20 cm water	38.1
Cluster 2 and end expiration negative 15-20 cm water	**35.2**

41

Conclusion

The variability in the SCG signal and heart rate during normal breathing and BH at various airway pressures was examined. Waveform variability was reduced by using unsupervised machine learning to group SCG signals obtained during normal breathing. A support vector machine was used to define the decision boundary, and classification accuracy was calculated. SCG waveforms may be accurately divided (>80%) into two groups, according to the findings.

The Unclustered, clustered, and BH instances were studied for changes in intra-cluster variability. The results showed that clustering reduced variability by 15% ($p < 0.05$) and BH reduced variability by additional 52% ($p < 0.05$). Inter cluster variability analysis showed that cluster 1 was more similar to end inspiration phases and cluster 2 was more similar to end expiration phases. The variability of heart rate during BH was also compared to regular breathing. During BH cases, there was an 8% ($p < 0.05$) decrease in heart rate and a 62% ($p < 0.05$) decrease in heart rate energy in the 0.15-0.4 Hz range. Furthermore, when the airway pressure during BH was changed from zero, SCG waveform variability was as high as 180%.

Other unsupervised machine learning techniques and supervised classifiers can be used to cluster SCG events during regular breathing in future investigations, and other supervised classifiers can be used to determine the decision boundary. The findings of future studies can then be compared to the results of this study. Future research with a larger number of subjects is also needed to confirm these findings in healthy people and heart failure patients.

CHAPTER 3 – THE IDENTIFICATION OF RESPIRATORY PHASE FROM SEISMOCARDIOGRAPHIC SIGNAL USING MACHINE LEARNING

Respiration may be monitored in certain patients, especially in critical care settings. Spirometers and thermocouples, which monitor air flow or temperature, can be used to directly measure respiration (Marks et al., 1995). These devices require direct connections to the mouth, nose, or breathing circuit, which can complicate clinical monitoring and possibly cause interference with recorded data (Weissman et al., 1984; Moody et al., 1985). Spirometry should be done in the sitting posture, according to a prior study (Miller et al., 2005), which is impractical for post-operative or ICU patients. These direct assessments may be difficult or undesirable in other situations, such as stress testing, ambulatory monitoring, or long-term surveillance. These drawbacks could be overcome by utilizing less intrusive respiratory monitoring techniques. A multi-lead ECG signal was employed in a prior work (Moody et al., 1985) to extract breathing signals. Transthoracic impedance has been linked to breathing in several studies (Geddes et al., 1962; Allison et al., 1964). According to recent study (Solar et al., 2017; Taebi & Mansy, 2017), changes in lung volume influence seismocardiographic (SCG) signals, implying that these physiological signals can be utilized to extract respiration signals noninvasively.

The objective of this study is to assess the performance of two machine learning algorithms (SVM and XGBoost) in identifying respiratory phases such as high lung volume (HLV) vs. low lung volume (LLV) or inspiration vs. expiration in healthy participants. Thoracic impendence readings are the same as GSR readings recorded at the chest surface.

Methods

Data collection

After receiving IRB approval, 15 healthy volunteers were recruited. The participants were instructed to lie supine on a bed with their feet extended horizontally and their heads tilted at a 45-degree angle. The SCG signals were captured using a tri-axial accelerometer (Model: 356A32, PCB Piezotronics, Depew, NY) mounted to the chest surface at the left lower sternal border at the 4th intercostal space. A recent study (Hassan et al., 2018; Hassan et al., 2019; Hassan et al., 2020; Hassan, 2019) also used accelerometers to measure this signal. A biopotential recorder was used to record the ECG signal (IX-B3G, Dover, NH, IWorx Systems, Inc.). It provides simultaneous acquisition of chest galvanic skin response (GSR) data by putting two separate electrodes beneath the subject's right collarbone and near the left abdomen. The sensor locations and experimental setup for this study are shown in Figure 34.
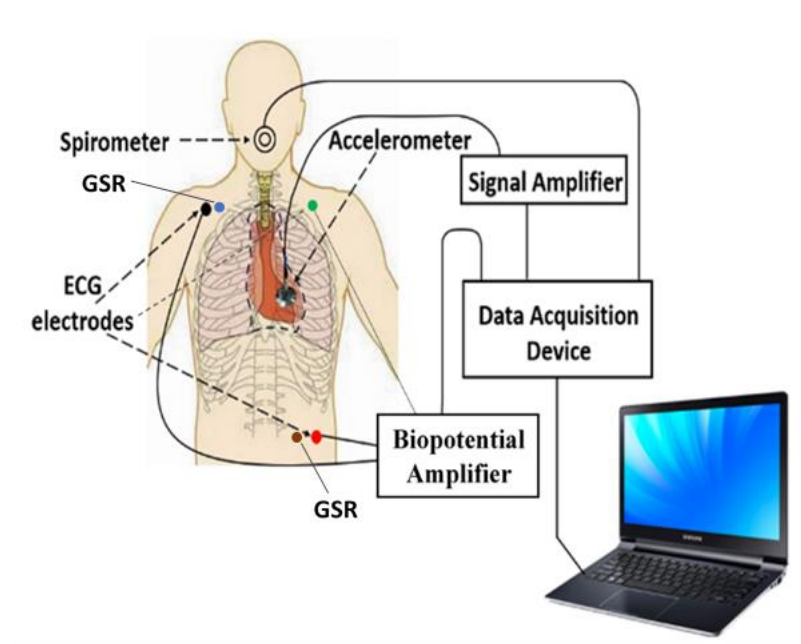
Figure 34 For this study, the sensor placements and experimental setup.

Feature collection, selection, and scaling

ECG R-peaks were used to detect and segment SCG beats. Each SCG event was chosen to start 0.1 seconds before the R peak of the related ECG and end 0.1 seconds before the next R peak. Figure 35 shows the SCG event selection from the R peak of the ECG.
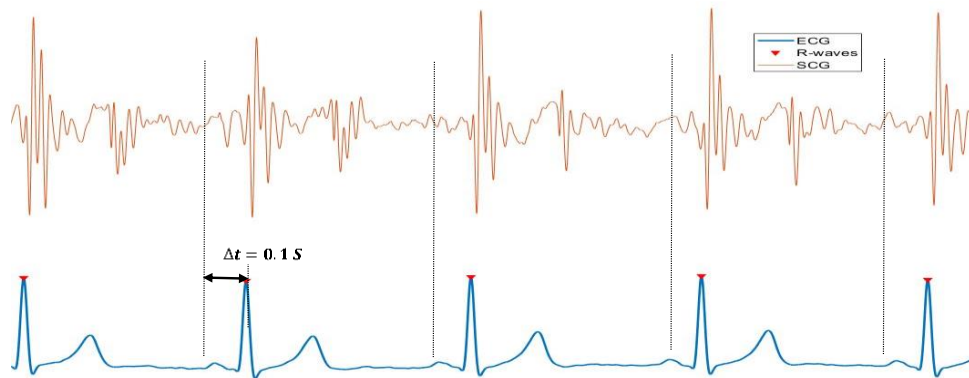
Figure 35 SCG event selection from ECG R peak.

Since an earlier study (Zakeri et al., 2017) showed the utility the waveform amplitudes (voltage) throughout every 4 milliseconds. This characteristic was used in this investigation. The characteristics are collected in Figure 36 by dividing the signal into bins and computing the average amplitude in each bin.

SCG beats were split into inspiratory and expiratory beats, as well as high and low lung volumes (relative to the mean lung volume), based on their time in the respiratory cycle. SCG event labeling based on lung volume signal is shown in Figure 37.

The characteristics were normalized before using them for training and testing, SVM and XGBoost were used for subject-specific (SS) training and testing (i.e., both training and testing were done for each subject separately). 70% of the data was used

for training, while 30% was used for testing each participant. For each subject, Table 18 displays the number of data points used for training and testing.
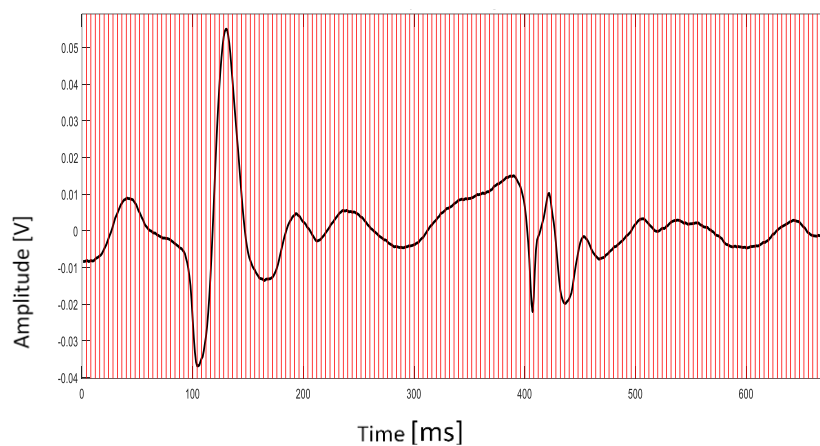
Figure 36 Selection of features from a segmented SCG waveform. The average amplitude over each 4 ms frame (the interval between the red lines) was chosen as a feature in this case.
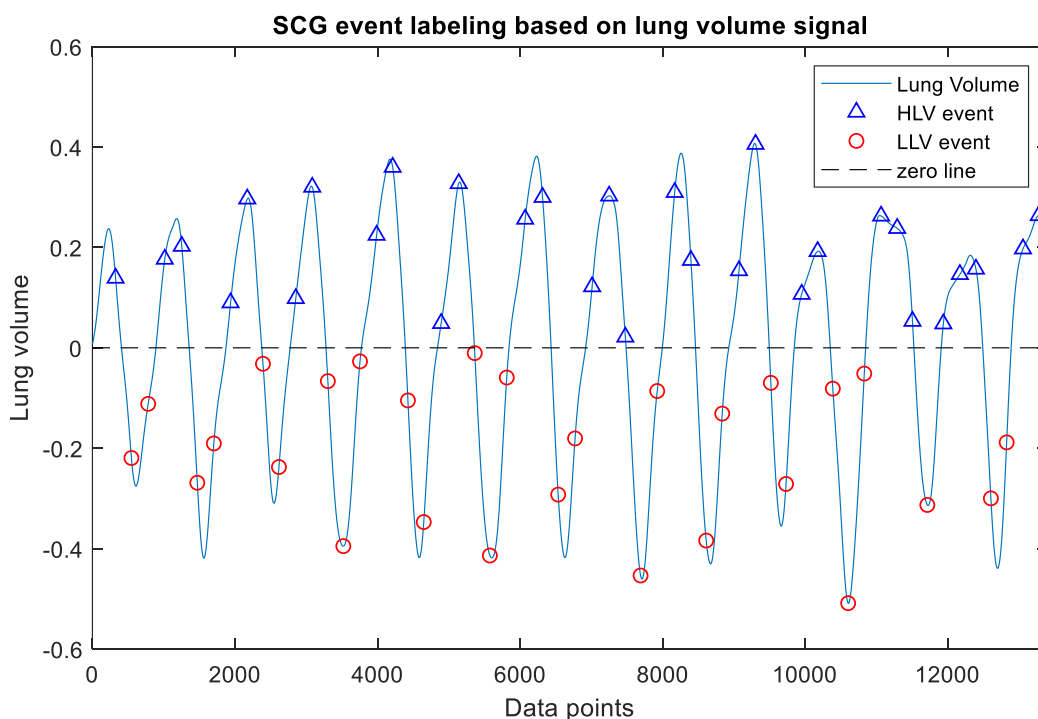
Figure 37 Labeling SCG events based on lung volume signal.

Table 18 The number of data points used for training and testing for each subject.

Subject No	Training samples	Testing samples
1	22088	9500
2	29116	12500
3	23845	10250
4	28112	12000
5	26857	11750
6	21084	9250
7	19327	8250
8	21084	9000
9	21586	9500
10	20080	8750
11	17570	7500
12	20080	8750
13	22590	9750
14	23343	10000
15	26857	11750

Machine learning framework

Support vector machine (SVM) and extreme Gradient Boosting (XGBoost) were utilized to extract respiration phases. When SVM was used, a hyperplane was found in the "features space" (Cortes et al., 1995) that maximizes the margin between classes (i.e., respiration phases). Linear kernel function was used to train the SVM. Boosting algorithms look for predictors in a sequential manner, with each succeeding model attempting to correct the flaws of the one before it. Figure 38 shows the model. For the XGBoost (Chen et al., 2016) model, the number of gradients boosted trees was
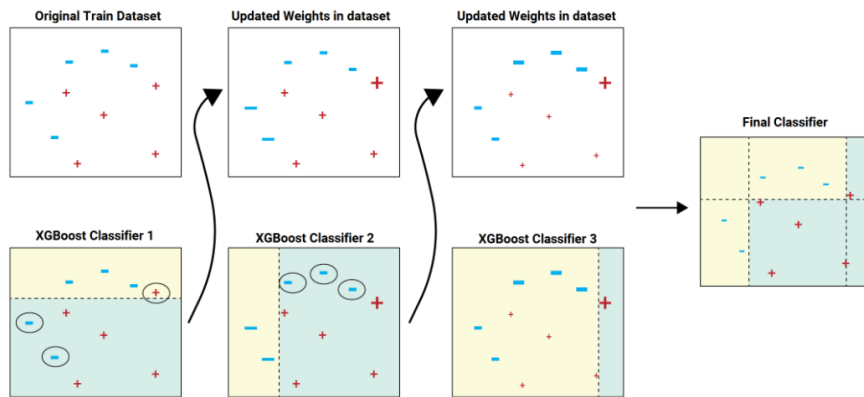
Figure 38 Illustration of finding predictor using boosting algorithm.

Table 19 Validation accuracy for each subject using SVM.

Subject No	Inspiration/Expiration	HLV/LLV
1	81	93
2	87	85
3	93	83
4	87	87
5	95	81
6	88	88
7	86	92
8	92	87
9	87	84
10	86	89
11	99	84
12	79	71
13	96	86
14	92	74
15	93	88

100, the maximum tree depth for base learners was 6 and boosting learning rate was 0.7. K-fold cross-validation (k=10) was performed for both models.

Table 19 and 20 show the validation accuracy using SVM and XGBoost for each subject. The validation accuracy was 89 ± 6 % for inspiration/expiration, 85 ± 6 % for HLV/LLV detection using SVM. For XGBoost the validation accuracy was 90 ± 4 % for inspiration/expiration and 85 ± 3 % for HLV/LLV detection. These findings are consistent with a previous study (Rahman et al., 2021).

Table 20 Validation accuracy for each subject using XGBoost.

Subject No	Inspiration/Expiration	HLV/LLV
1	89	88
2	87	87
3	85	85
4	91	89
5	94	84
6	92	88
7	86	85
8	94	87
9	86	82
10	87	86
11	97	80
12	83	79
13	95	81
14	90	83
15	92	88

Performance parameters

The performance parameters calculated and compared in this study are: testing accuracy, sensitivity/recall, specification, precision, F1 score. Validation accuracy is the calculated accuracy on the data set not used for testing. Testing accuracy is percentage of predicted value that matches with actual value. Sensitivity/Recall is true

positive rate. Specificity is true negative rate. Precision is positive predictive value. F1 score is is the harmonic mean of precision and sensitivity. Sensitivity/recall, specificity, precision and F1 score are calculated from the following equations:

$$TPR = \frac{(TP)}{(TP+FN)} \qquad (10)$$

$$TNR = \frac{(TN)}{(TN+FP)} \qquad (11)$$

$$PPV = \frac{(TP)}{(TP+FP)} \qquad (12)$$

$$F1 = 2\frac{precision * recall}{precision + recall} = \frac{2TP}{(2TP+FP+FN)} \qquad (13)$$

Results

Figure 39, figure 40, figure 41, figure 42, table 21, table 22, table 23, table 24 demonstrate the subject-specific testing accuracy, sensitivity/recall, specificity, precision, and F1 score (Fawcett et al., 2006) for detecting HLV/LLV and inspiration/expiration phases using SVM and XGBoost. Results showed that the average testing accuracy, sensitivity/recall, specificity, precision, F1 score were 91 ± 6 %, 91 ± 9 %, 91 ± 8 %, 91 ± 7 %, 91 ± 6 %, respectively for inspiration/expiration and 86 ± 6 %, 87 ± 8 %, 85 ± 10 %, 88 ± 6 %, 87 ± 5 %, respectively for HLV/LLV detection using SVM. For XGBoost, these parameters were 91 ± 6 %, 93 ± 6 %, 89 ± 9 %, 90 ± 7 %, 91 ± 5%, respectively for inspiration/expiration and 87 ± 3 %, 92 ± 7 %, 82 ± 9 %, 85 ± 6 %, 88 ± 3 %, respectively for HLV/LLV detection.
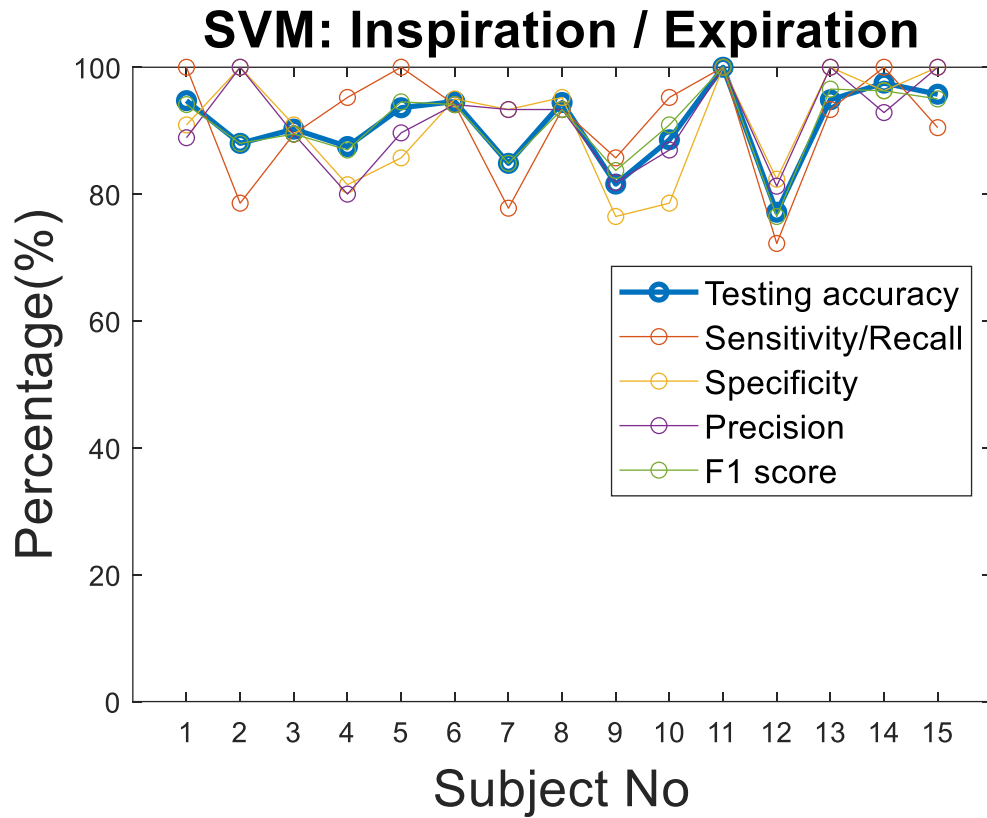
Figure 39 The accuracy, sensitivity/recall, specificity, precision, and F1 score for all participants when using SVM to detect inspiration/expiration phases.

Table 21 For all individuals, the mean and standard deviation of subject-specific testing accuracy, sensitivity/recall, specification, precision, and F1 score to detect to detect inspiration/expiration phases using SVM

SVM: Insp/Exp	Mean	SD
Testing accuracy	90.9	6.3
Sensitivity	91.0	8.8
Specificity	91.1	8.2
Precision	91.4	6.9
F1 score	91.0	6.1

XG Boost: Inspiration / Expiration
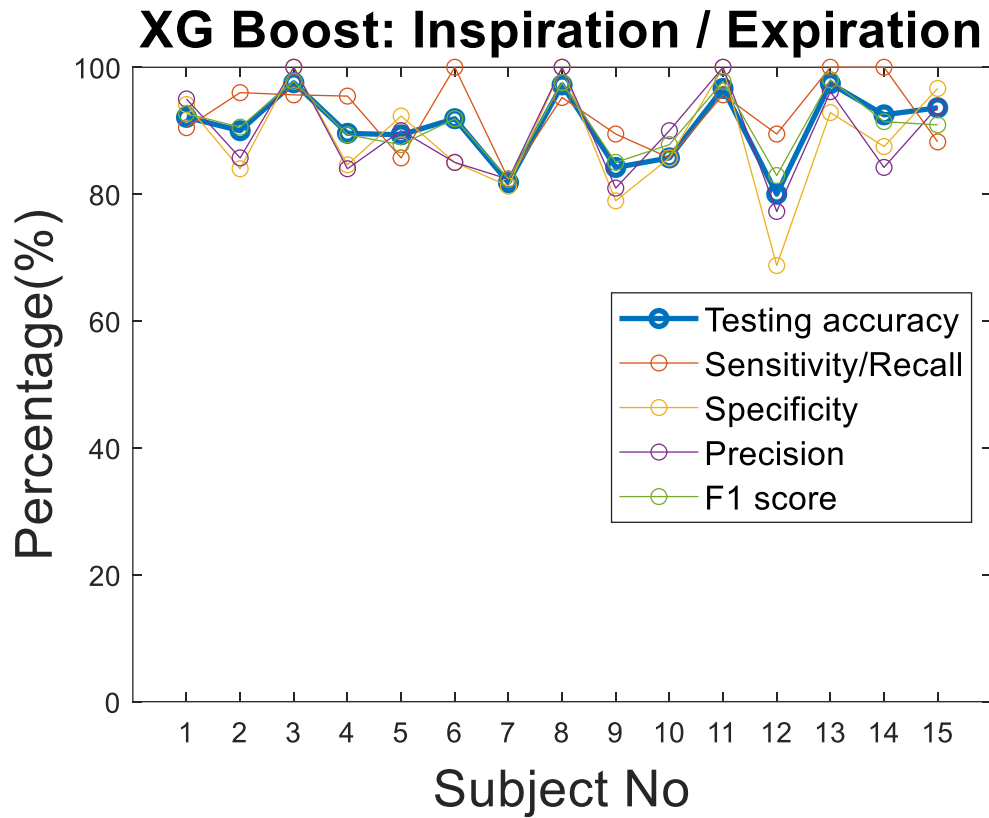
Figure 40 The accuracy, sensitivity/recall, specification, precision, and F1 score for all subjects using XGBoost to detect inspiration/expiration phases.

Table 22 For all individuals, the mean and standard deviation of subject-specific testing accuracy, sensitivity/recall, specification, precision, and F1 score to detect to detect inspiration/expiration phases using XGBoost.

XG Boost: Insp/Exp	Mean	SD
Testing accuracy	90.6	5.7
Sensitivity	92.6	5.7
Specificity	88.8	8.9
Precision	89.6	6.6
F1 score	90.9	5.3
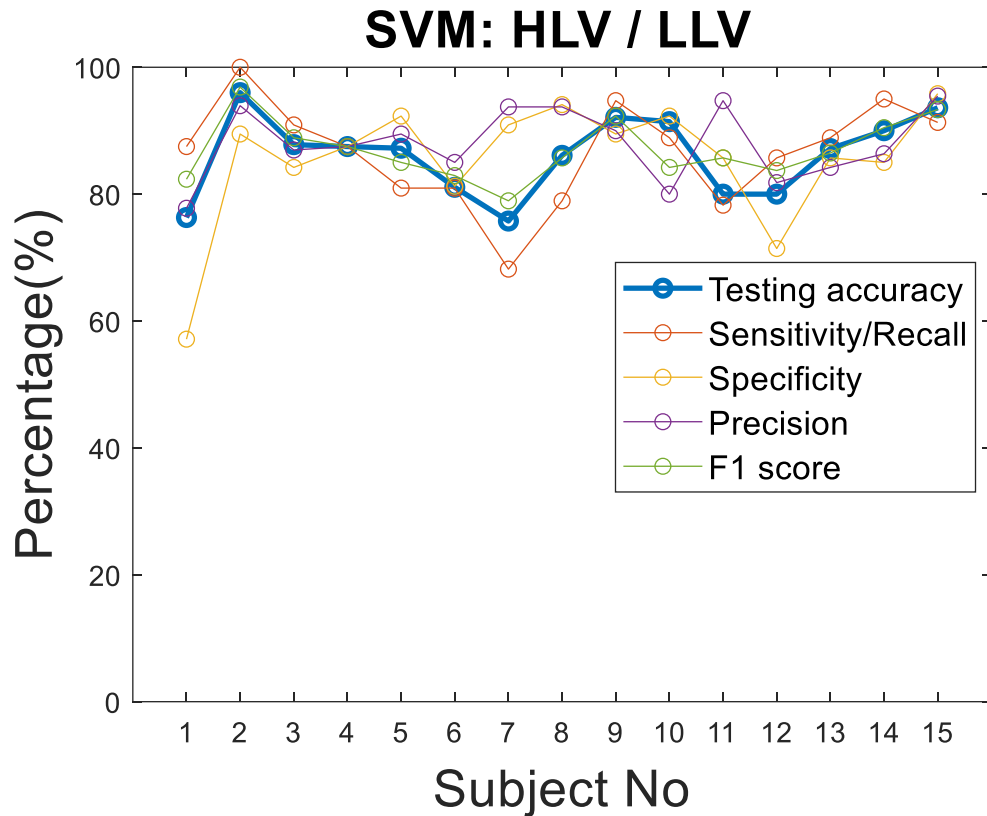
Figure 41 The accuracy, sensitivity/recall, specification, precision, and F1 score for all individuals when using SVM to detect high lung volume/low lung volume phases.

Table 23 For all individuals, the mean and standard deviation of subject-specific testing accuracy, sensitivity/recall, specification, precision, and F1 score to detect to detect high lung volume/low lung volume phases using SVM.

SVM: HLV/LLV	Mean	SD
Testing accuracy	86.1	6.2
Sensitivity	86.5	8.0
Specificity	85.5	9.9
Precision	88.0	5.6
F1 score	87.0	4.7
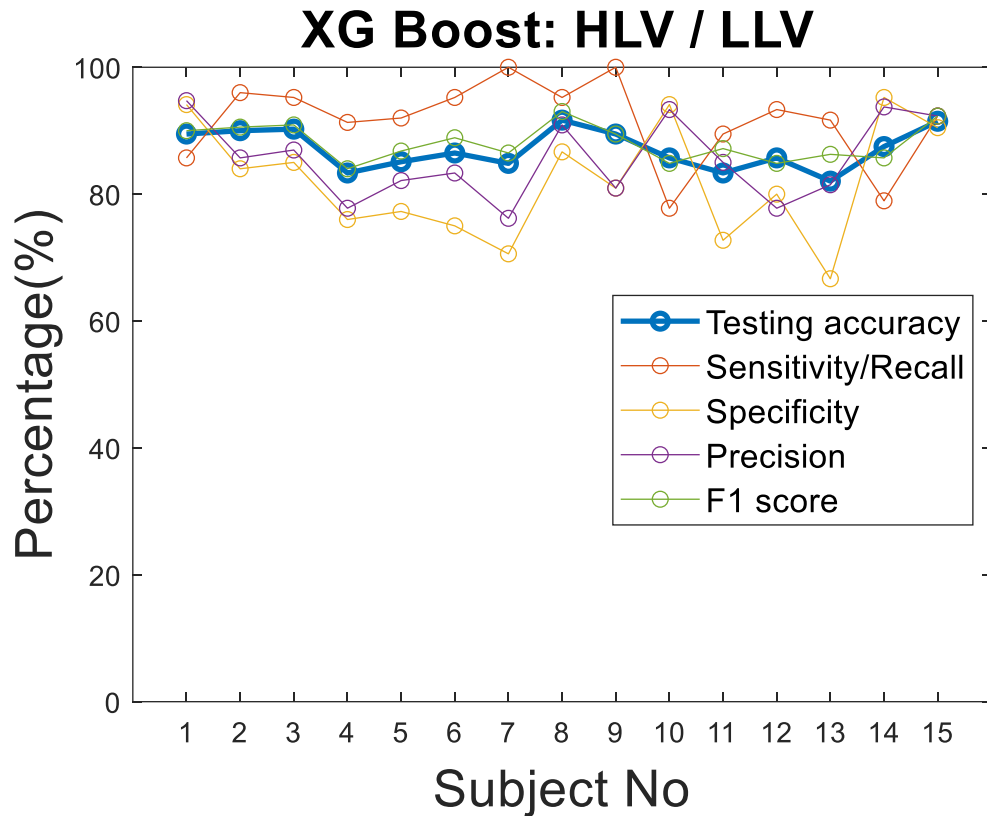
Figure 42 The accuracy, sensitivity/recall, specification, precision, and F1 score for all individuals using XGBoost to detect high lung volume/low lung volume phases.

Table 24 For all individuals, the mean and standard deviation of subject-specific testing accuracy, sensitivity/recall, specification, precision, and F1 score to detect high lung volume/low lung volume phases using XGBoost.

XG Boost: HLV/LLV	Mean	SD
Testing accuracy	87.1	3.1
Sensitivity	91.6	6.5
Specificity	81.9	9
Precision	85.5	6.3
F1 score	88.1	2.9

Conclusion

The accuracy of detecting HLV/LLV or inspiration/expiration phases from SCG was tested using the supervised machine learning techniques SVM and XGBoost in this study. The average testing accuracy using SVM was 91 percent for inspiration/expiration and 86 percent for HLV/LLV detection. The precision of inspiration/expiration was 91 percent with XGBoost and 87 percent with HLV/LLV. SCG signals paired with machine learning algorithms were found to be capable of reliably detecting respiratory phases in normal persons. This information can also be used to calculate the respiratory rate. More testing in a larger sample of both healthy and cardiac disease patients is recommended. Other machine learning approaches, such as random forest, k-nearest neighbor, and artificial neural network, could be used to increase accuracy.

CHAPTER 4 – FINITE ELEMENT ANALYSIS OF SCG

The measurement of vibrations on the chest surface generated by mechanical heart activity such as myocardial contractions, valve closure and opening, and blood momentum changes is known as seismocardiography (SCG) (Gurev et al., 2012; Korzeniowska-Kubacka et al., 2006). To measure SCG, an accelerometer is commonly positioned on the chest surface. Because of its low cost, non-invasive nature, and compatibility with telemedicine, SCG may have high potential for diagnosing and monitoring a variety of cardiac diseases. SCG analysis in the time and frequency domains has been investigated for cardiac diagnosis (Amirtaha Taebi, 2018; Amirtaha Taebi et al., 2018). SCG features have been used to estimate respiratory rate and monitor sleep apnea (Reinvuo et al., 2006; Morillo et al., 2010).

The SCG signal is thought to represent a combination of complicated 3D cardiac motions observed on the chest wall surface during pumping action. Relating the SCG morphology to its vibration origin has been difficult due to the complexity of heart motions, as well as vibrations induced by cardiac muscle activity, blood flow, valve openings and closings, and other factors. Some researchers have used medical imaging to link different SCG signal characteristic points by matching their occurrence time to relevant cardiac events recorded during cardiac imaging (Crow et al., 1994; Giorgis et al. 2008), but the results are still unclear (Crow et al., 1994; Giorgis et al., 2008), but the results are still unclear (Akhbardeh et al., 2009).

Cardiac structures (e.g., pericardium, Aorta wall) diaplace their surrounding tissues before the vibrations propagate to the chest surface (e.g., lung tissue, ribs, chest muscle, and skin). As a result, modeling the propagation of total cardiac wall motion to the chest surface could help us better understand SCG, perform parametric research

56

(e.g., on the effects of tissue features, etc.), and investigate SCG origin by correlating feature points to cardiac wall motion.

In a few articles, SCG has been computationally modelled. To assess the movements of the ventricles, one study (Akhbardeh et al., 2009) separated the ventricles frame by frame and fitted a deformable mesh to the segmented volume. By subtracting the displacement of a site on the ventricle wall from an observation point, the tissue movement signal was computed. Using an electro-mechanical model of a canine heart, the same study (Akhbardeh et al., 2009) discovered a SCG-like acceleration at the center of mass of the ventricles. This electromechanical model (Akhbardeh et al., 2009) was employed in another study (Tavakolian et al., 2012) to see how simple geometries affected the simulated SCG. These studies predicted SCG waveforms that matched the general shape of previously published SCG waveforms (Amirtahà Taebi et al., 2019).

The current study aims to model the propagation of heart wall vibrations to the chest surface in order to simulate the SCG. The 3D motion of the heart wall was tracked using an optical flow-based motion tracking approach using short-axis cardiac cine MRI images (Peshala Gamage, 2020). The Finite Element Method (FEM) and the recorded heart wall movements boundary conditions were implemented to generate in a computer model of SCG. A section of the lung, rib cage, intercoastal muscles (ICMs), and other chest wall musculature in the thorax were included in the model geometry.

Shifting the location of the heart and relative to rib cage was used to duplicate the geometry of the end inspiration and end expiration. The simulated morphological alterations of SCG wer compared to measured human SCG to study the effect of heart displacement with respiration. This study also looked into the effect of additional soft

tissue in the outer muscle on SCG signal. These studies may increeas our understanding of SCG propoagation, potentially increasing SCG's diagnostic utility.

Methods: computational modeling

By segmenting the voxel in chest images, the geometry of a computational model was constructed (Gamage, 2020). Short-axis MRI slices were stacked to construct this voxel dataset (Gamage, 2020). This region includes the chest muscle, ribs, cartilage, and lung, as shown in figure 43 (a) (b). Although the position of the sternum could be observed in MRI images, the intensity contrast levels of available MRI imaging hindered effective segmentation of the ribs and cartilage. As a result, the ribcage was separately modeled using dimensions from the literature (Laurin, Jobin, & Bellemare, 2012). The geometry was then scaled and put into the model to match the size and alignment of the sternum and ribs. The intercostal muscles were modeled by connecting the muscle tissue between the ribs (Hamzah et al., 2013). On a human chest, Figure 44 demonstrates the placement and direction of computational geometry (c). The geometry was restricted to that region to save time and money while still incorporating regions of the chest surface where SCG is regularly recorded (Taebi et al., 2019).

The computational modeling was done using the ANSYS (ANSYS Inc, Canonsburg, PA) transient structural analysis module, which uses the finite element method (FEM) to solve displacements in the computational domain. In FEM, the structural domain is divided into small (finite) elements that are assembled to satisfy boundary requirements and represent component interfaces (i.e., contacts). The forces and displacements acting on each constituent are governed by the equation of motion.

58

All of the component equations are combined into a system of equations, which is then solved to provide all of the element displacements (Gamage, 2019).

Figure 43 (a) shows the resultant finite element mesh, which contained 45000 elements and 84500 nodes and was produced in ANSYS. The observed motion of the cardiac surface was matched to the computer model, as shown in figure 43 (b). As shown in figure 43 (c) and (d), all degrees of freedom were set at the medial and lateral borders of the ribs (d). This could be explained by the exceedingly low (near-zero) vibrations of the rib cage (during breath-holding). Bonded connections were defined at the rib cage and muscle interfaces. A contact condition was created at the lung-chest wall interface to aid sliding between the lung and chest wall.
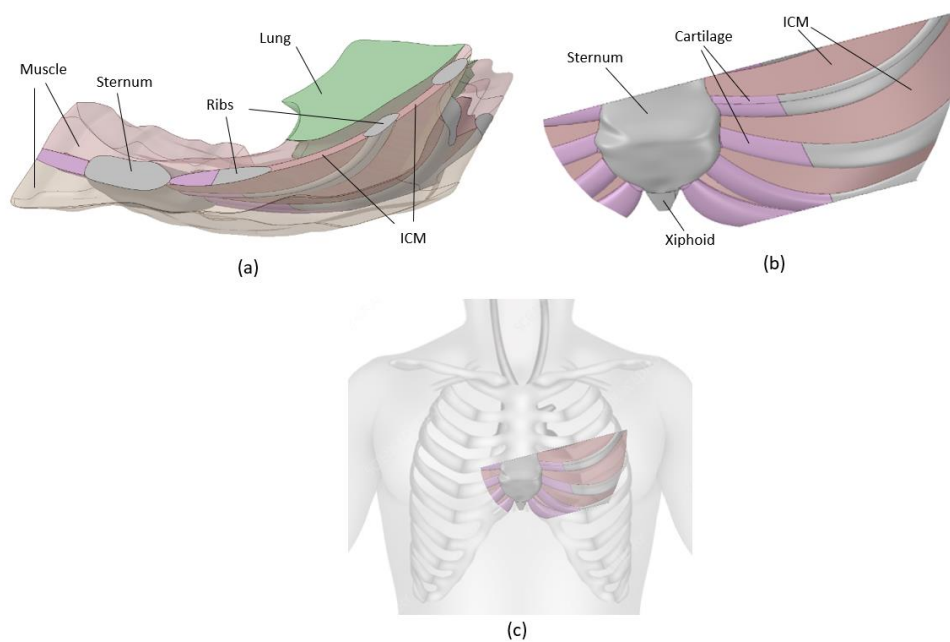
Figure 43 The 3D modeled region's location and detailed structures (a) Muscular, bony, and lung regions (b) Ribs, ICM, cartilage, sternal, and xiphoid (c) placement and orientation of the modeled region (Gamage, 2020).
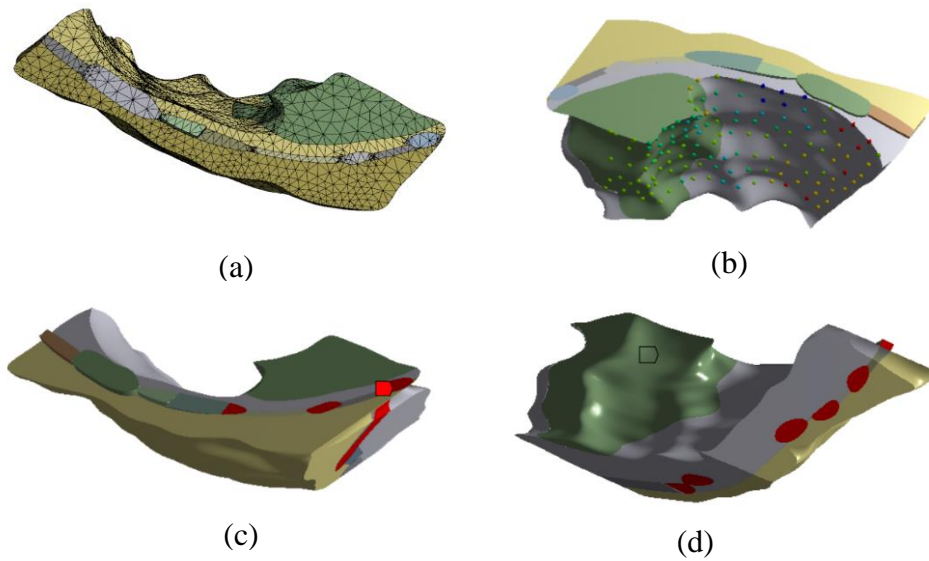
Figure 44 (a) Computational mesh, (b) MRI-mapped displacements of the heart surface, and (c) and (d) further 3D views of the computational model domain. The rib edges are in red color (Gamage, 2020).

All components are assumed to have a linear elastic behavior, with the exception of the lung. The lung hyperplastic material properties were fitted to the Mooney-Rivlin 5th order model using existing knowledge (Al-Mayah et al., 2007). Each component material properties are listed in Table 25. Even though the chest muscle and skin are made up of multiple separate components, they were modeled as a single component in this study (pericardial muscle, pectoralis major, and skin). Because previous studies (Chawla et al., 2006; Gefen & Dilmoney, 2007; Zigras, 2007) demonstrated a variety of elasticity values for these components, the impact of different elasticities on the simulated SCG was investigated.

Table 25 Material properties (Gamage, 2020)

Component	Young's modulus	Density (kg/m3)	Poisson's ratio	References
Chest Muscle (includes pericardial tissue, pectoralis major, Skin)	2.5 (MPa)	1000	0.3	(Chawla, Mukherjee, & Karthikeyan, 2006; Gefen & Dilmoney, 2007; Zigras, 2007
Sternum, Ribs, Xiphoid	12 (GPa)	2000	0.4	(Sundaram & Feng, 1977)
Costal cartilage	3 (GPa)	2000	0.4	(Chawla et al., 2006)
Intercostal muscle	3 (MPa)	1000	0.4	(Chawla et al., 2006)
Lung	Mooney Rivlin 5th order $C10=-859.78$ Pa $C01= 947.5$ Pa $C20=1783.2$ Pa $C11=-5440.5$ Pa $C02=4633.5$ Pa	1250	-	(Al-Mayah, Moseley, & Brock, 2007; Zeng, Yager, & Fung, 1987)

<u>Results</u>

Respiratory effect (heart location changes)

The SCG signal has been demonstrated to be influenced by breathing. Several research have looked into the morphological variability of the SCG due to respiration (Azad, Gamage, Sandler, Raval, & Mansy, 2019; Gamage et al., 2018; Gamage, Azad, Taebi, Sandler, & Mansy, 2020; Sandler et al., 2019; Sandler et al., 2019). To investigate the effect of heart position (due to breathing) on the SCG signal form, the relative position between the heart and the ribcage was changed to replicate the end-

expiration and end-inspiration phases. In this scenario, the model geometry original position (derived from MRI imaging) provided the final inspiration. The rib cage was adjusted (with respect to the heart) to imitate end inspiration, based on prior work (Bogren et al., 1977) that analyzed the 3D respiratory movement of the heart using cineangiography.
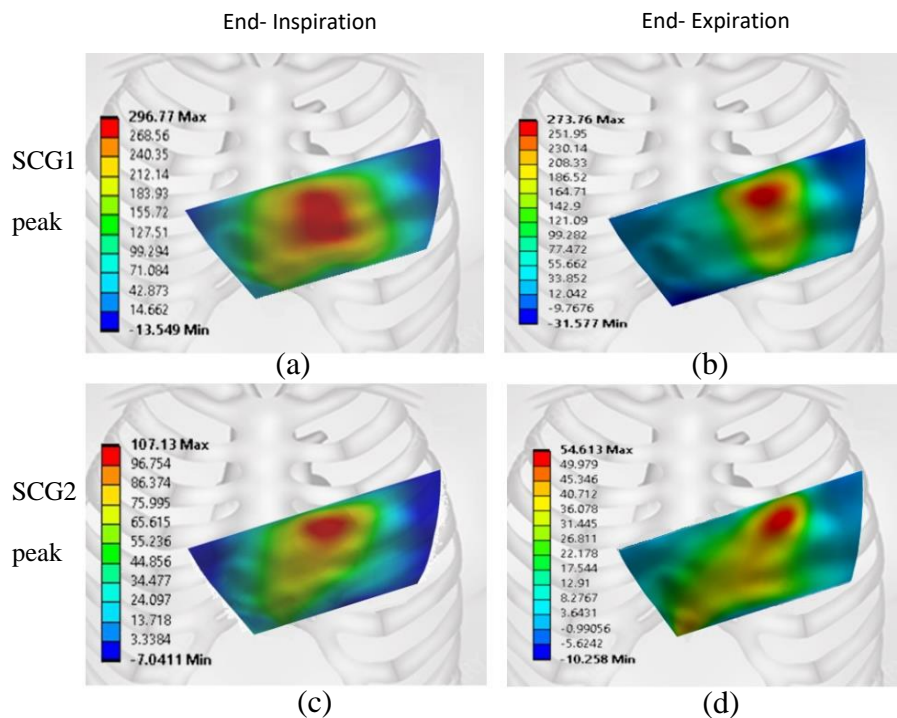
Figure 45 Surface acceleration distribution in the dorso-ventral direction at SCG 1 and SCG 2 peak times at: (a) & (c) end inspiration state; and (b) & (d) end expiration. The SCG peak tended to be louder at the end of inspiration. The SCG1 peak moved about 3cm to the right at the end of expiration, which is comparable with the corresponding upward movement in the heart position; all data are in mm/s^2 (Gamage, 2020).

For the inspiratory and expiratory states, Figure 45 depicts the surface acceleration distribution of the chest surface at SCG1 and SCG2 peaks. There is a variation in the maximum amplitude regions between the two states. At the time of SCG1 peak, the region with the largest amplitudes for the end-inspiration state was concentrated along the left sternal border of the 4th ICS, and this region shifted laterally and upward to the 3rd ICS for the end-expiration state. At the moment of SCG 2 peak,

the maximum amplitude region shifted somewhat laterally and superiorly with expiration. The heart's lateral and upward movement during expiration could be the cause of this occurrence.
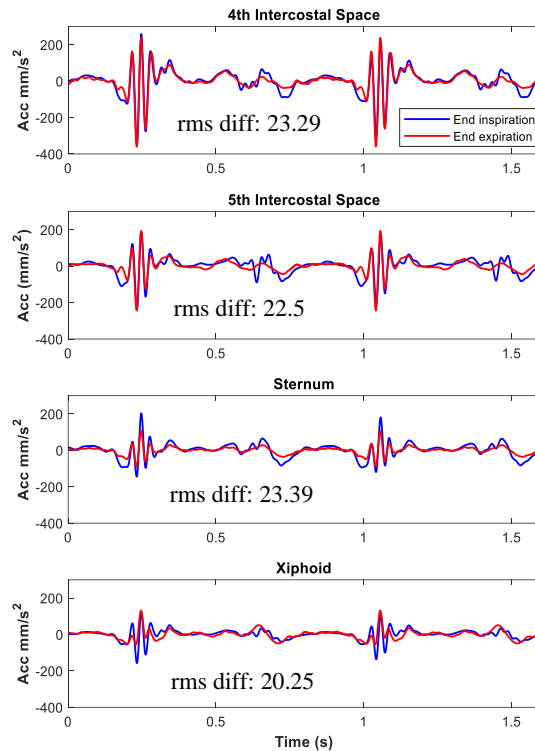
Figure 46 End-of-inspiration and end-of-expiration SCG signals simulated at various chest sites. The waveform variability (measured as the rms of the waveform difference) matched experimental results (Gamage, 2020).

To investigate the effect of heart position (due to respiratory motion) on SCG morphology, the simulated SCG was created on the same surface location for end inspiration and end expiration simulations. There were little morphological variations between the end-inspiration and end-expiration phases. To quantify the dissimilarity of the SCG morphologies, the root mean square (rms) of the difference between two waveforms was used to examine the morphological changes of two SCG waveforms. Figure 46 depicts the SCG waveforms at the end of inspiration and end of expiration, as well as their relative rms differences. These differences were similar to experimental

breath-hold (i.e., measured during end-inspiration and end-expiration) SCG data collected in a previous study (Azad et al., 2019), which found an rms difference of (mean=28.24, SD=8.909 mm/s2) for measurements at the 4th ICM near the left Intercostal Border (ICB) on 5 healthy subjects (Azad et al., 2019). These data suggest that variations in SCG shape due to changes in the relative positioning of the heart and rib cage during breathing could be one of the variability causes (Azad et al., 2019; Gamage et al., 2020).

Effect of extra soft tissue
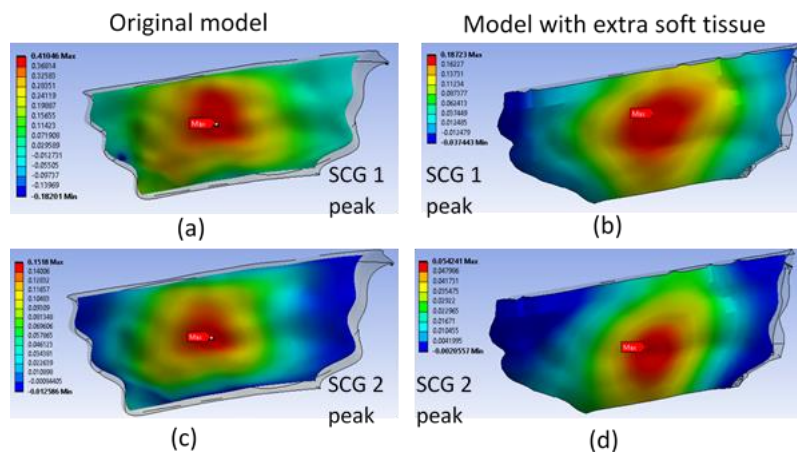
Figure 47 Surface acceleration distribution in dorso-ventral direction at: (a) &(c) original model in end inspiration state; and (b) & (d) 1 cm extra soft tissue on outer muscle during both SCG 1 and SCG 2 peak timing.

To see how extra soft tissue may affect the SCG signal, 1 cm of soft tissue was added to the outer chest surface. The chest surface acceleration distribution at the SCG1 and SCG2 peaks is shown in Figure 47 for the original model and the model with added soft tissue. There was a variation in the maximum amplitude regions between the two states.

The simulated SCG was created on the same surface as the original model at end inspiration, and the model with extra soft tissue was used to investigate the effect of extra soft tissue on SCG waveform. When compared to the original model, SCG of the model with more soft tissue had morphological differences and a lower amplitude. The morphological difference between the two SCG waveforms (those with and without extra soft tissue) was measured by comparing the SCG 1 maximum peak ratio and SCG 2 maximum peak ratio between the original model and the model with extra soft tissue. For the original model and the model with added soft tissue, the SCG 1 maximum peak ratio was 2 and the SCG 2 peak ratio was 3. Figure 48 shows the SCG waveforms for the original model and the model with added soft tissue.
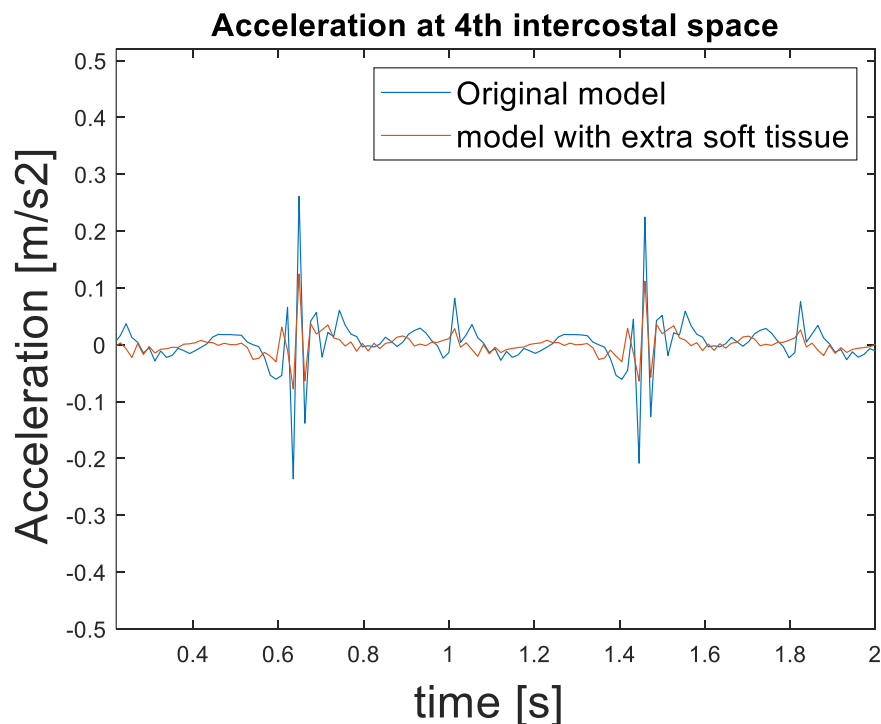
Figure 48 Simulated SCG signals at 4th intercostal space for the original model and model with extra soft tissue. SCG amplitude was decreased by 0.0305 m/s^2 due to extra soft tissue in the model.

Conclusion

The propagation of cardiac vibration from the heart wall boundary to the chest surface was modeled computationally. A region of the chest above the heart ventricles containing ribs, intercostal muscles, chest tissue, and lung was studied. Changes in the location of the heart relative to the rib cage was implemented to replicate end-inspiratory and end-expiratory breath hold phases and to explore the influence of heart displacement (due to respiration) on SCG. The morphological differences of SCG detected at these two states are equivalent to the differences seen in experimental measurements, implying that cardiac respiratory motion could be a contributing factor to the varied SCG morphologies described in prior studies. SCG amplitude also decreased as the thickness of the outer muscle was increased by introducing extra soft tissue. The study's findings should help us better understand the origins of SCG, which could lead to increased clinical utility for SCG. Future research could incorporate SCG modeling for failing hearts, which would provide more detailed information on SCG genesis.

APPENDIX A: TIME AND FREQUENCY DOMAIN ANALYSIS OF SCG EVENTS DURING DIFFERENT BREATHING MANEUVERS

Objective: The objective of this study is to perform SCG time and frequency domain analysis during different breathing maneuvers to investigate morphological variation in SCG signal between these breathing states.

Methods: After segmenting SCG events from R peak, time and frequency domain analysis was performed for all breathing states. The analysis was performed on both unclustered and clustered normal breathing runs.
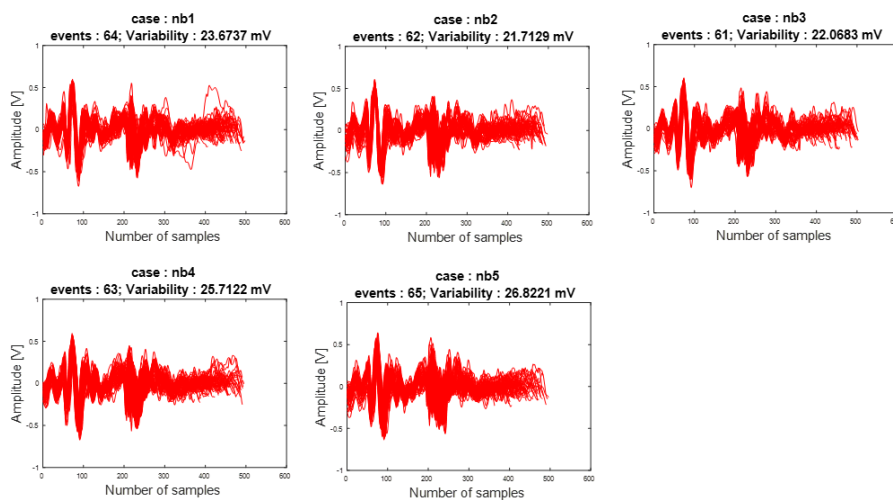
Figure 49 Time domain analysis during 5 runs of normal breathing without performing clustering with events plotted on top of each other for a subject. Number of events and variability values in each run are also listed.

Figure 50 Time domain analysis during 5 runs of normal breathing without performing clustering where events are plotted on top of previous SCG event for a subject.

Figure 51 Frequency domain analysis during 5 runs of normal breathing without performing clustering where the spectra of each SCG event are plotted on top of each other.

Findings: Events and variability in each run during different breathing maneuvers were calculated when time domain analysis was performed for each subject. Figure 49 shows Time domain analysis during 5 runs of normal breathing without performing clustering with number of events where each events are plotted on top of each other. Waveform variability in each run can be seen. Figure 50 shows time domain analysis during 5 runs of normal breathing without performing clustering where each events events are plotted

Figure 52 Time domain analysis during 5 runs of normal breathing cluster 1 with events plotted on top of each other for a subject. Number of events and variability values in each run are also listed.

69

on top of previous SCG event. Figure 51 shows Frequency domain analysis during 5 runs of normal breathing without performing clustering where the SCG waveform are plotted on top of each other.

Figure 53 Time domain analysis during 5 runs of normal breathing cluster 1 where events are plotted on top of previous SCG event for a subject.

Figure 54 Frequency domain analysis during 5 runs of normal breathing cluster 1 where the spectra of each SCG event are plotted on top of each other.

Figure 52 shows Time domain analysis during 5 runs of normal breathing cluster 1 with number of events where events are plotted on top of each other and variability can be seen in each run for another subject. Figure 53 shows time domain analysis during 5

runs of normal breathing cluster 1 where events are plotted on top each other. Figure 54 shows Frequency domain analysis during 5 runs of normal breathing cluster 1 where frequency domain of each events are plotted on top of each other for aother subject.

Figure 55 Time domain analysis during 5 runs of normal breathing cluster 2 with events plotted on top of each other for a subject. Number of events and variability values in each run are also listed.

Figure 56 Time domain analysis during 5 runs of normal breathing cluster 2 where events are plotted on top of previous SCG event for a subject.
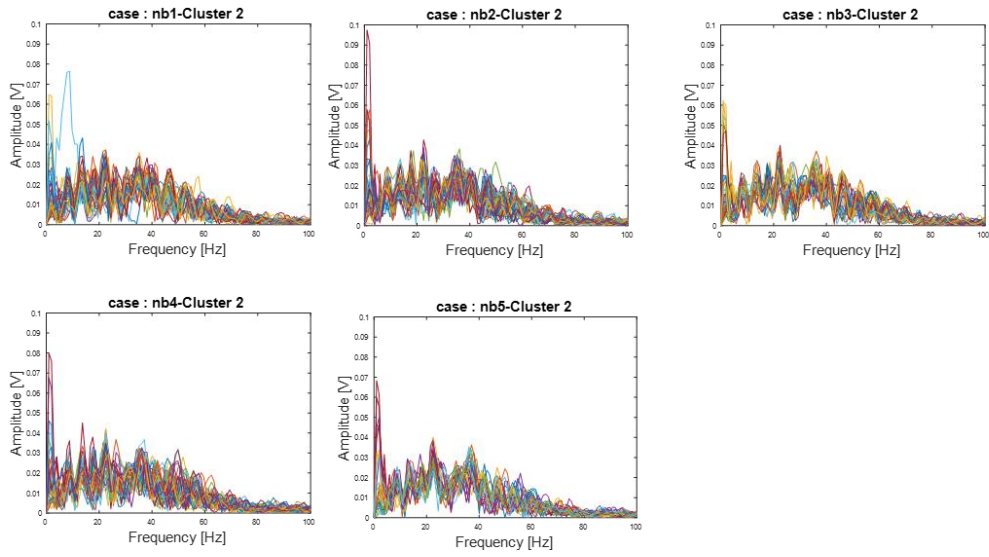
Figure 57 Frequency domain analysis during 5 runs of normal breathing cluster 2 where the spectra of each SCG event are plotted on top of each other.

Figure 55 shows Time domain analysis during 5 runs of normal breathing cluster 2 with number of events where events are plotted on top of each other and variability in each run for another subject. Figure 56 shows time domain analysis during 5 runs of normal breathing cluster 2 where events are plotted on top of previous SCG event for another subject. Figure 57 shows Frequency domain analysis during 5 runs of normal breathing cluster 2 where frequency domain of events are plotted on top of each other. Time and frequency domain results from Figure 49-57 shows that by performing clustering variability is reduced.

Figure 58 Time domain analysis during 3 runs of breath holding at end inspiration with events plotted on top of each other for a subject. Number of events and variability values in each run are also listed.
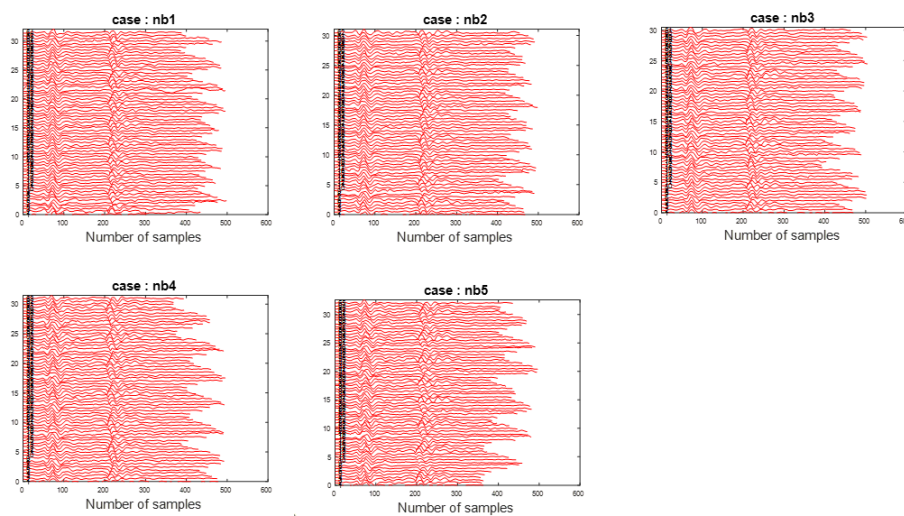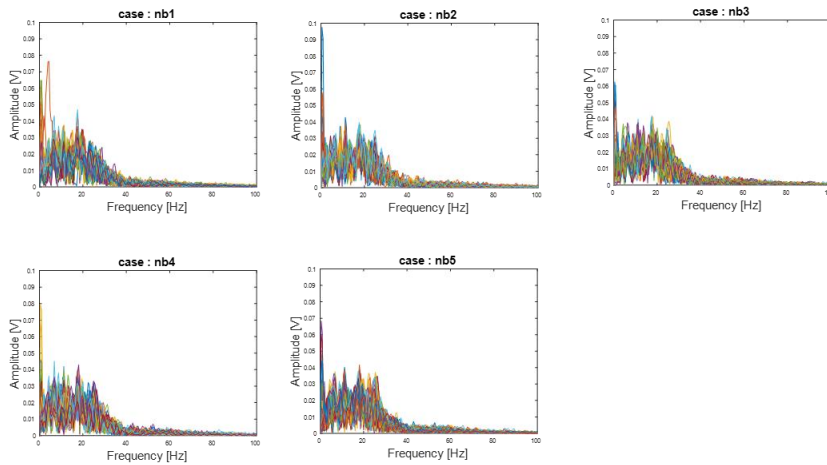
Figure 59 Time domain analysis during 3 runs of breath holding at end inspiration where events are plotted on top of previous SCG event for a subject.
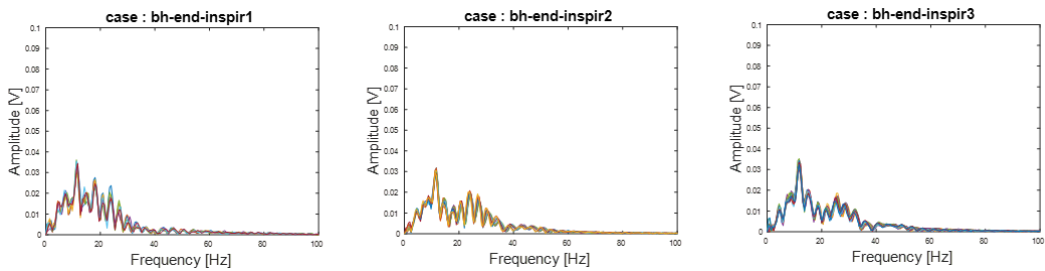
Figure 60 Frequency domain analysis during 3 runs of breath holding at end inspiration where the spectra of each SCG event are plotted on top of each other.

Figure 58 shows Time domain analysis during 3 runs of breath holding at end inspiration with number of events where events are plotted on top of each other and variability in each run can be seen. Figure 59 shows time domain analysis during 3 runs of breath holding at end inspiration where events are plotted on top of each otehr for another subject. Figure 60 shows Frequency domain analysis during 3 runs of breath holding at end inspiration where the spectrum of each events are plotted on top of each other.
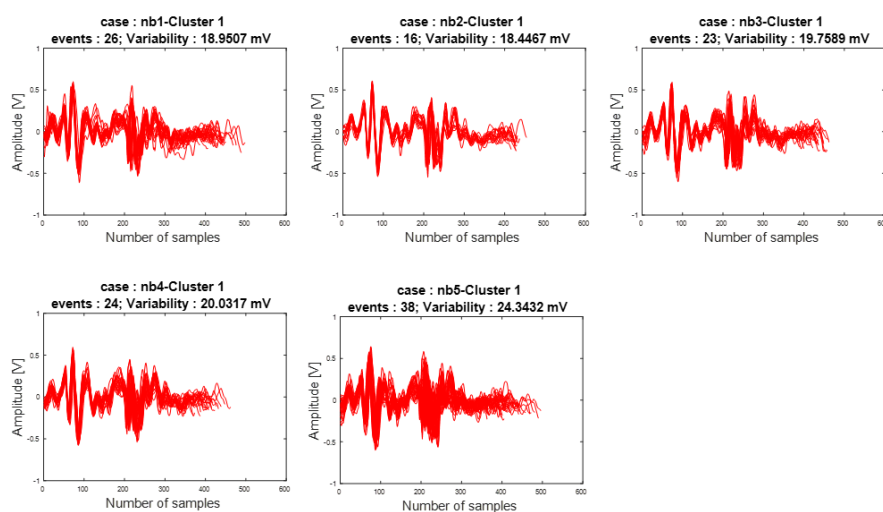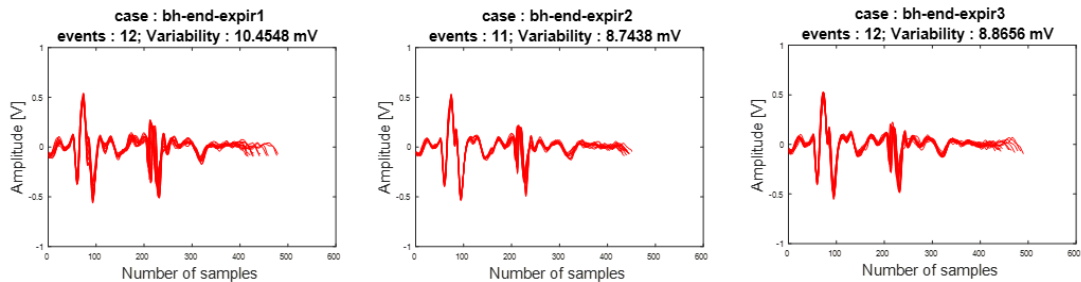

Figure 61 Time domain analysis during 3 runs of breath holding at end expiration with events plotted on top of each other for a subject. Number of events and variability values in each run are also listed.
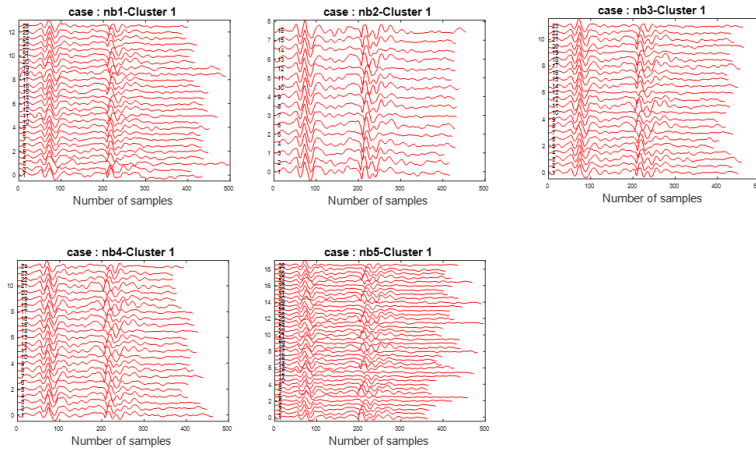
73

Figure 62 Time domain analysis during 3 runs of breath holding at end expiration where events are plotted on top of previous SCG event for a subject.
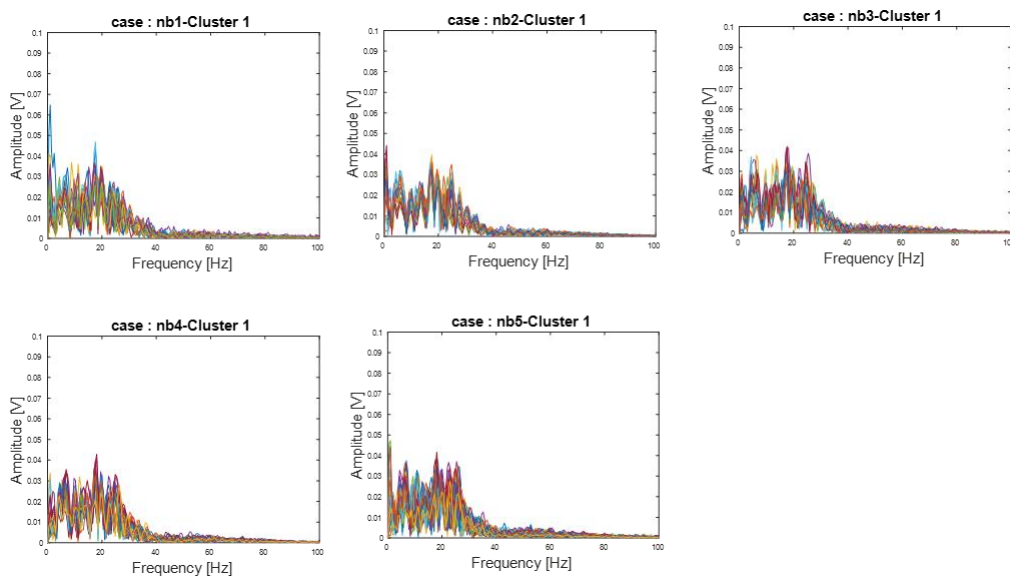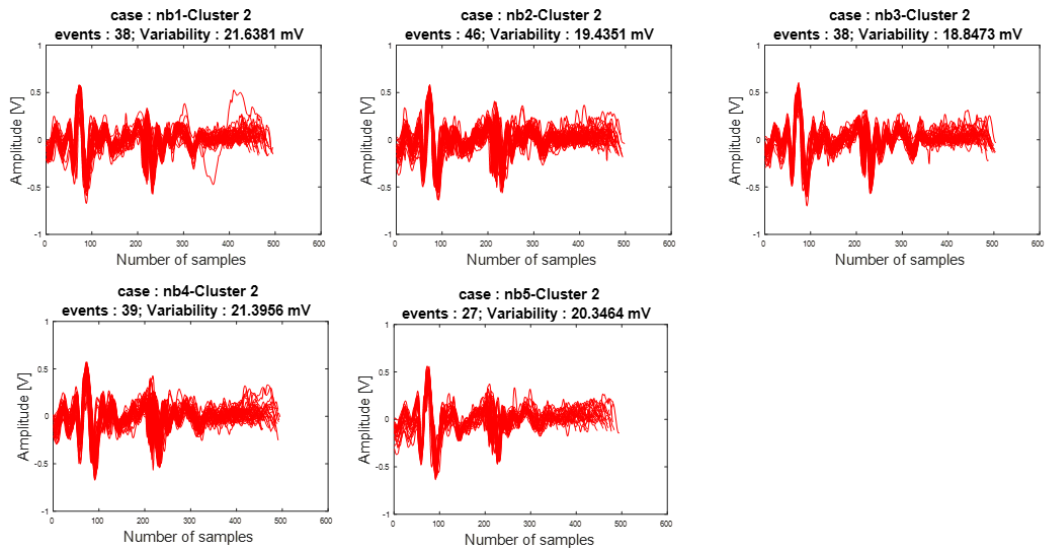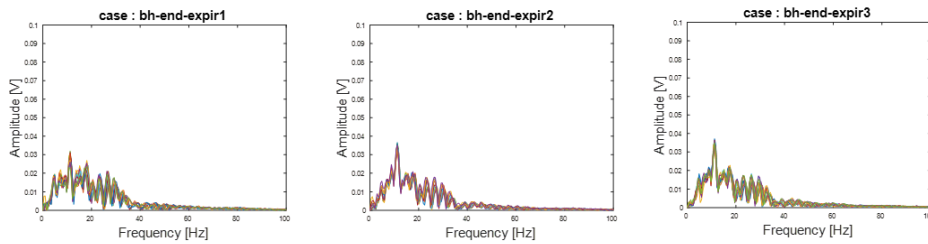

Figure 63 Frequency domain analysis during 3 runs of breath holding at end expiration where the spectra of each SCG event are plotted on top of each other.

Figure 61 shows Time domain analysis during 3 runs of breath holding at end expiration with number of events where events are plotted on top of each other and variability in each run for a subject. Figure 62 shows time domain analysis during 3 runs of breath holding at end expiration where events are plotted on top of previous SCG event for a subject. Figure 63 shows Frequency domain analysis during 3 runs of breath holding at end expiration where frequency domain of events are plotted on top of each other. Time and frequency domain results from Figure 58-63 shows that by performing breath holding variability is further reduced.

Figure 64 Time domain analysis during 3 runs of end inspiration at positive 2-4 cm water pressure with events plotted on top of each other for a subject. Number of events and variability values in each run are also listed.

74

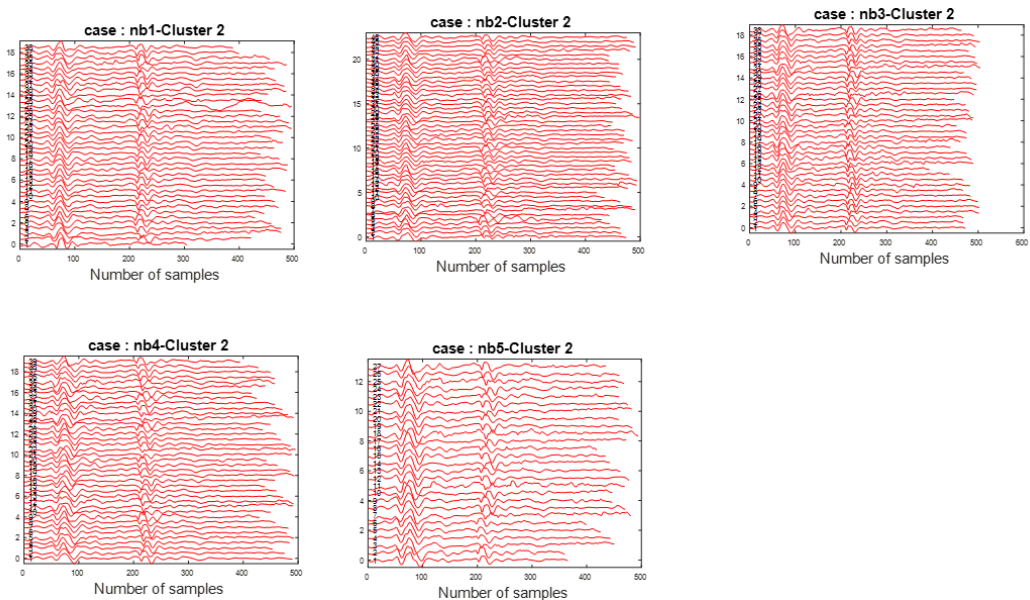Figure 65 Time domain analysis during 3 runs of end inspiration at positive 2-4 cm water pressure where events are plotted on top of previous SCG event for a subject.
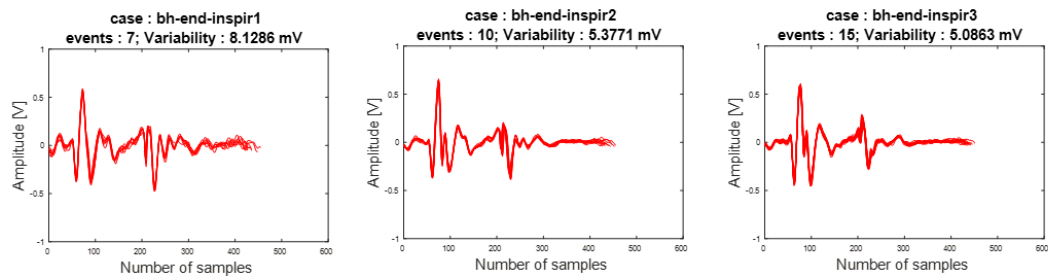

Figure 66 Frequency domain analysis during 3 runs of end inspiration at positive 2-4 cm water pressure where the spectra of each SCG event are plotted on top of each other.

Figure 64 shows Time domain analysis during 3 runs of end inspiration at positive 2-4 cm water pressure with number of events where events are plotted on top of each other for another subject. Figure 65 shows time domain analysis during 3 runs of end inspiration at positive 2-4 cm water pressure where events are plotted on top of previous events for another subject. Figure 66 shows Frequency domain analysis during 3 runs of end inspiration at positive 2-4 cm water pressure where frequency domain of each events are plotted on top of each other.

Figure 67 shows Time domain analysis during 3 runs of end inspiration at negative 2-4 cm water pressure with number of events where events are plotted on top of each other for a subject. Figure 68 shows time domain analysis during 3 runs of end inspiration at negative 2-4 cm water pressure where events are plotted on top of previous SCG event

for another subject. Figure 69 shows Frequency domain analysis during 3 runs of end

inspiration at negative 2-4 cm water pressure where frequency domain of

events are plotted on top of each other.

Figure 67 Time domain analysis during 3 runs of end inspiration at negative 2-4 cm water pressure with events plotted on top of each other for a subject. Number of events and variability values in each run are also listed.
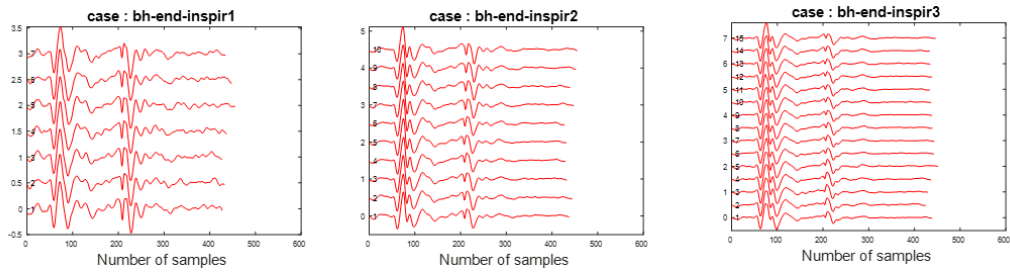

Figure 68 Time domain analysis during 3 runs of end inspiration at negative 2-4 cm water pressure where events are plotted on top of previous SCG event for a subject.

Figure 69 Frequency domain analysis during 3 runs of end inspiration at negative 2-4 cm water pressure where the spectra of each SCG event are plotted on top of each other.

Figure 70 shows Time domain analysis during 3 runs of end inspiration at positive 15-

20 cm water pressure with number of events where events are plotted on top of each

other for a subject. Figure 71 shows time domain analysis during 3 runs of end

inspiration at positive 15-20 cm water pressure where events are plotted on top of

Figure 70 Time domain analysis during 3 runs of end inspiration at positive 15-20 cm water pressure with events plotted on top of each other for a subject. Number of events and variability values in each run are also listed.

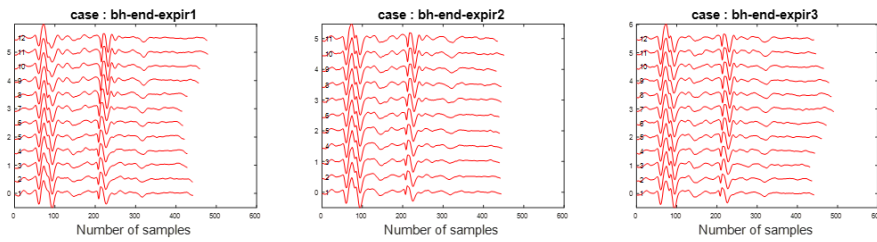Figure 71 Time domain analysis during 3 runs of end inspiration at positive 15-20 cm water pressure where events are plotted on top of previous SCG event for a subject.

Figure 72 Frequency domain analysis during 3 runs of end inspiration at positive 15-20 cm cm water pressure where the spectra of each SCG event are plotted on top of each other.

previous SCG event for a subject. Figure 72 shows Frequency domain analysis during

3 runs of end inspiration at positive 15-20 cm water pressure where frequency domain

of events are plotted on top of each other.

Figure 73 shows Time domain analysis during 3 runs of end inspiration at negative 15-
20 cm water pressure with number of events where events are plotted on top of each
other for another subject. Figure 74 shows time domain analysis during 3 runs of end

Figure 73 Time domain analysis during 3 runs of end inspiration at negative 15-20 cm
water pressure with events plotted on top of each other for a subject. Number of events
and variability values in each run are also listed.

Figure 74 Time domain analysis during 3 runs of end inspiration at negative 15-20 cm
water pressure where events are plotted on top of previous SCG event for a subject.

Figure 75 Frequency domain analysis during 3 runs of end inspiration at negative 15-
20 cm cm water pressure where the spectra of each SCG event are plotted on top of
each other.

inspiration at negative 15-20 cm water pressure where each events are plotted on top of

previous SCG event for a subject. Figure 75 shows Frequency domain analysis during

3 runs of end inspiration at negative 15-20 cm water pressure where frequency domain

of each events are plotted on top of each other. Time and frequency domain results from Figure 64-75 shows that by performing positive and negative normal and increased airway pressure after end inspiration variability is further increased compared to breath holding at end inspiration.
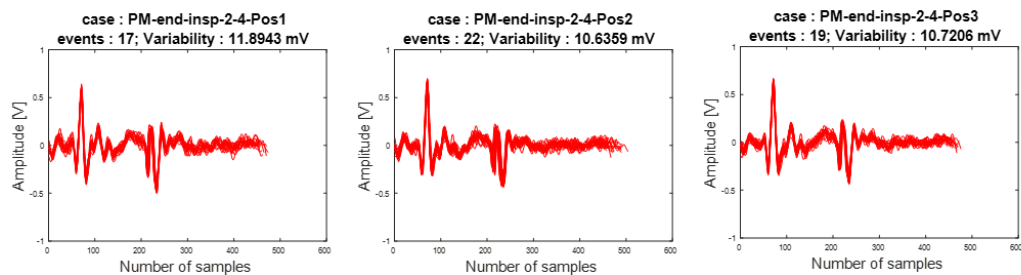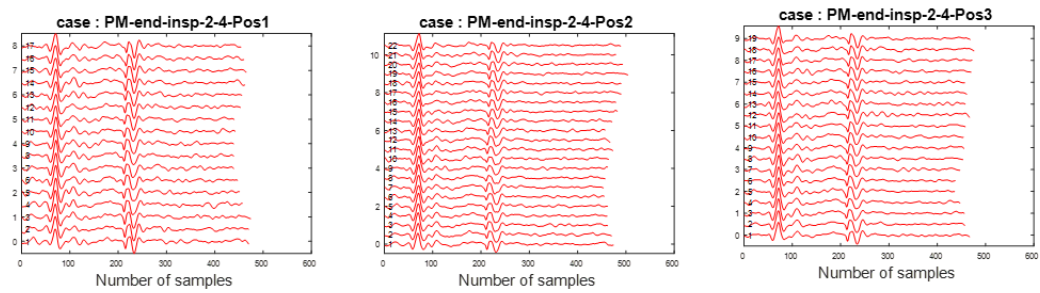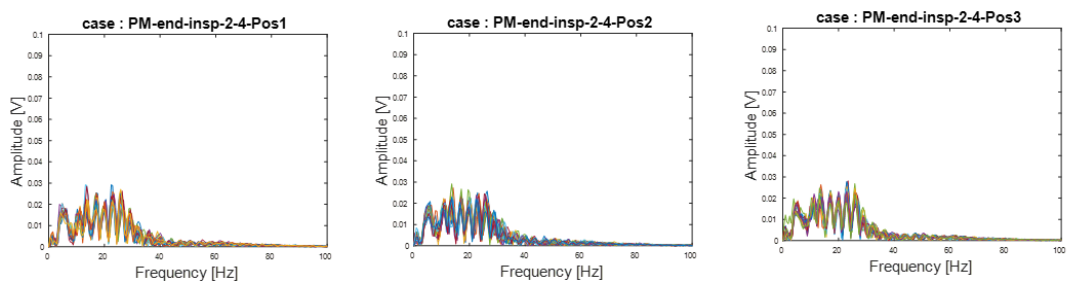

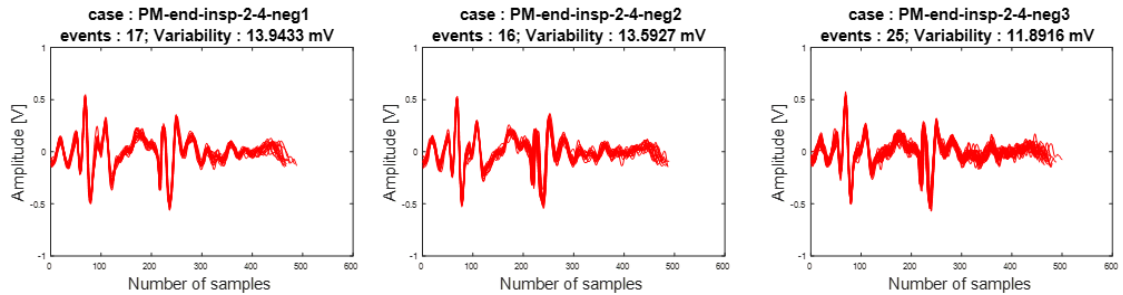Figure 76 Time domain analysis during 3 runs of end expiration at positive 2-4 cm water pressure with events plotted on top of each other for a subject. Number of events and variability values in each run are also listed.

Figure 77 Time domain analysis during 3 runs of end expiration at positive 2-4 cm water pressure where events are plotted on top of previous SCG event for a subject.

Figure 78 Frequency domain analysis during 3 runs of end expiration at positive 2-4 cm water pressure where the spectra of each SCG event are plotted on top of each other.

Figure 76 shows Time domain analysis during 3 runs of end expiration at positive 2-4 cm water pressure with number of events where each events are plotted on top of each

79

other and variability in each run for a subject. Figure 77 shows time domain analysis

during 3 runs of end expiration at positive 2-4 cm water pressure where each events are

plotted on top of previous SCG event for a subject. Figure 78 shows Frequency domain

analysis during 3 runs of end expiration at positive 2-4 cm water pressure where

frequency domain of each events are plotted on top of each other.
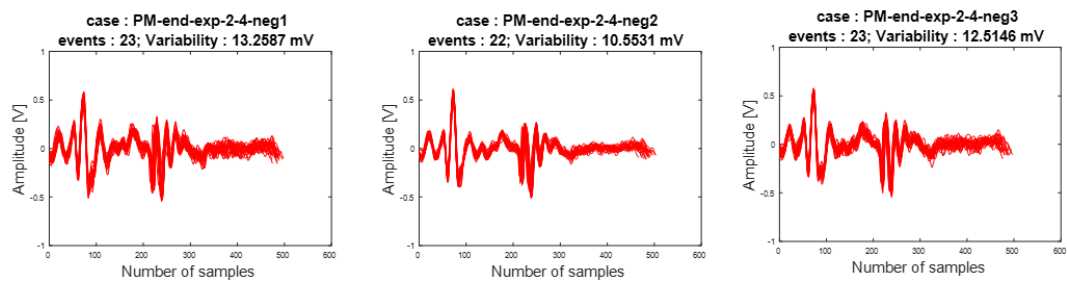
Figure 79 Time domain analysis during 3 runs of end expiration at negative 2-4 cm
water pressure with events plotted on top of each other for a subject. Number of events
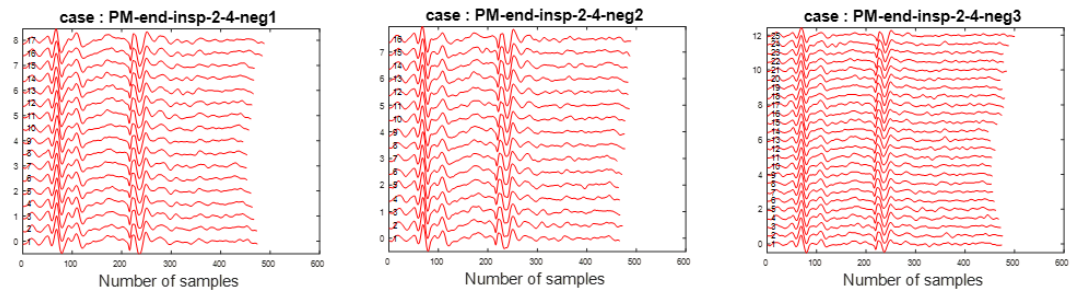and variability values in each run are also listed.
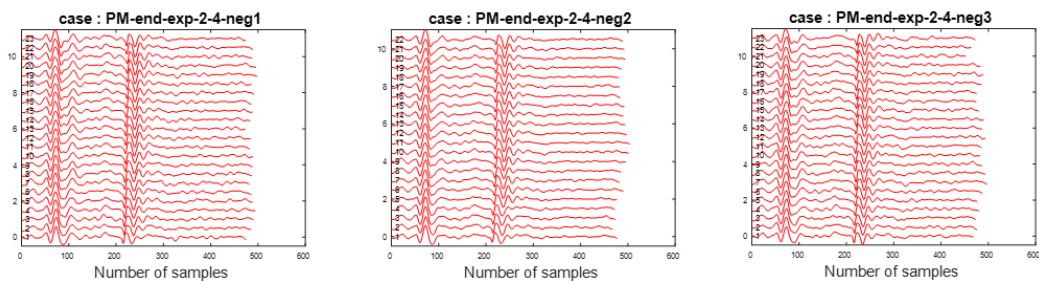
Figure 80 Time domain analysis during 3 runs of end expiration at negative 2-4 cm
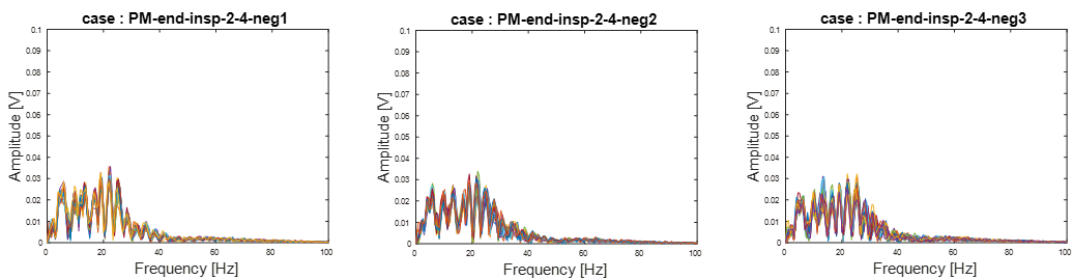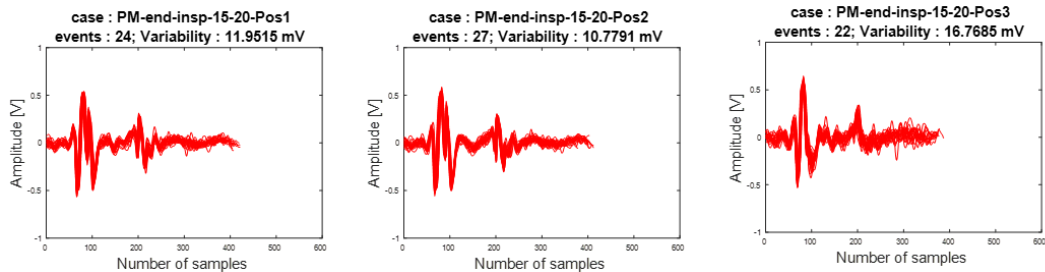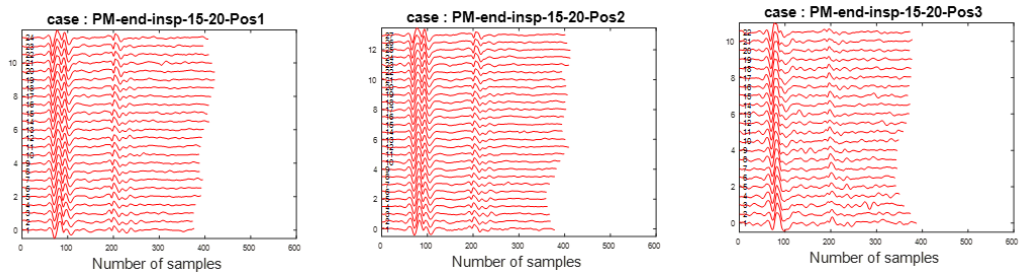water pressure where events are plotted on top of previous SCG event for a subject.
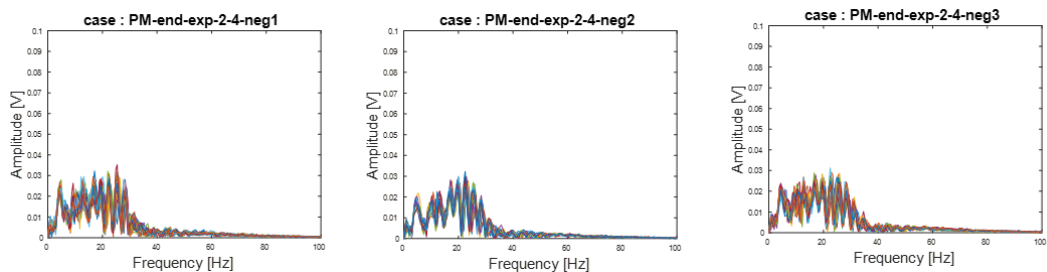
Figure 81 Frequency domain analysis during 3 runs of end expiration at negative 2-4
cm water pressure where the spectra of each SCG event are plotted on top of each other.

Figure 79 shows Time domain analysis during 3 runs of end expiration at negative 2-4

cm water pressure with number of events where each events are plotted on top of each

other and variability in each run for a subject. Figure 80 shows time domain analysis during 3 runs of end expiration at negative 2-4 cm water pressure where each events are plotted on top of previous SCG event for a subject. Figure 81 shows Frequency domain analysis during 3 runs of end expiration at negative 2-4 cm water pressure where frequency domain of each events are plotted on top of each other.
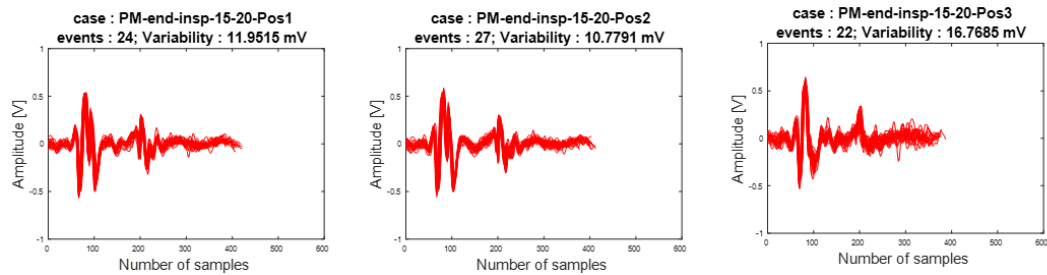
Figure 82 Time domain analysis during 3 runs of end inspiration at positive 15-20 cm water pressure with events plotted on top of each other for a subject. Number of events and variability values in each run are also listed.
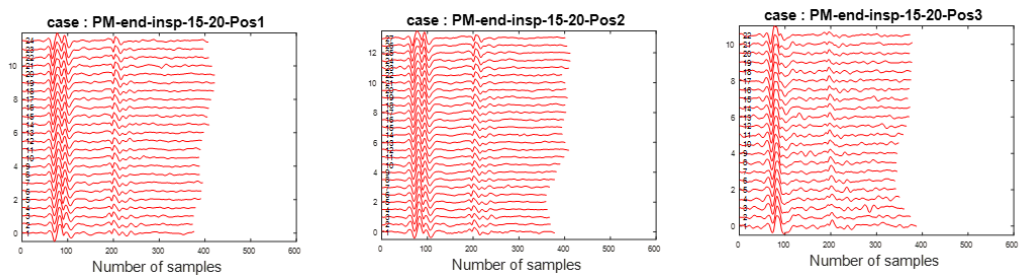
Figure 83 Time domain analysis during 3 runs of end inspiration at positive 15-20 cm water pressure where events are plotted on top of previous SCG event for a subject.
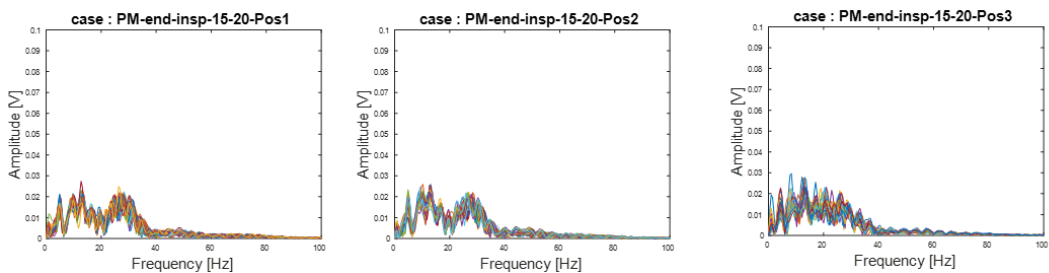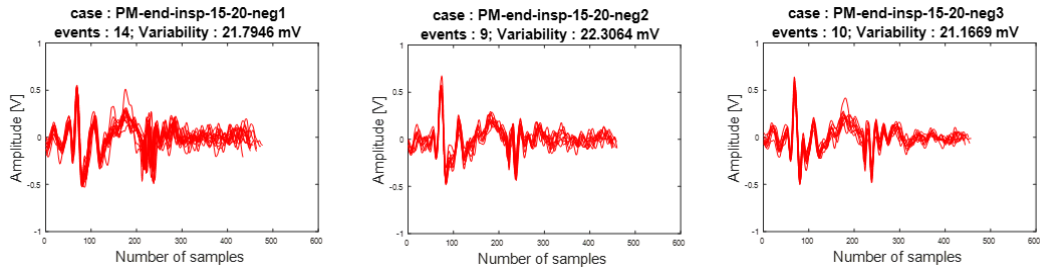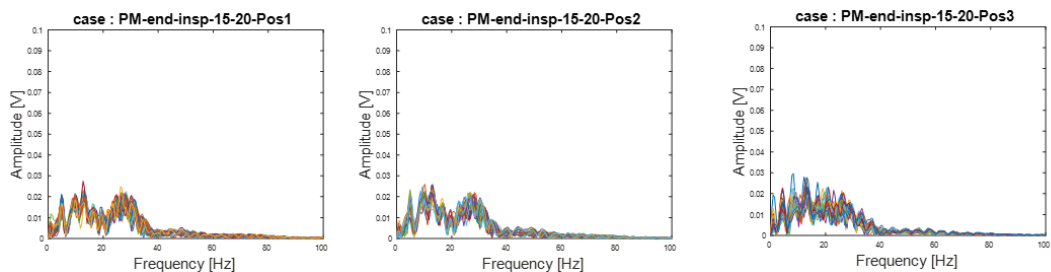

Figure 84 Frequency domain analysis during 3 runs of end inspiration at positive 15-20 cm cm water pressure where the spectra of each SCG event are plotted on top of each other.

Figure 82 shows Time domain analysis during 3 runs of end expiration at positive 15-20 cm water pressure with number of events where each events are plotted on top of each other and variability in each run for a subject. Figure 83 shows time domain analysis during 3 runs of end expiration at positive 15-20 cm water pressure where each events are plotted on top of previous SCG event for a subject. Figure 84 shows Frequency domain analysis during 3 runs of end expiration at positive 15-20 cm water pressure where frequency domain of each events are plotted on top of each other.

Figure 85 shows Time domain analysis during 3 runs of end expiration at negative 15-20 cm water pressure with number of events where each events are plotted on top of each other and variability in each run for a subject. Figure 86 shows time domain analysis during 3 runs of end expiration at negative 15-20 cm water pressure where each events are plotted on top of previous SCG event for a subject. Figure 87 shows Frequency domain analysis during 3 runs of end expiration at negative 15-20 cm water pressure where frequency domain of each events are plotted on top of each other. Time and frequency domain results from Figure 76-87 shows that by performing positive and negative normal and increased airway pressure after end expiration variability is further increased compared to breath holding at end expiration.
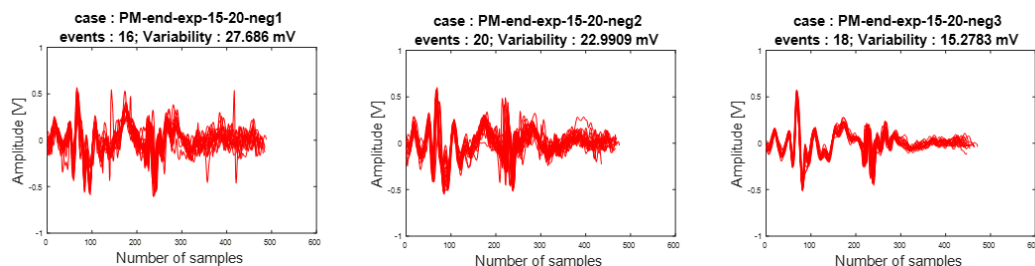
Figure 85 Time domain analysis during 3 runs of end expiration at negative 15-20 cm water pressure with events plotted on top of each other for a subject. Number of events and variability values in each run are also listed.
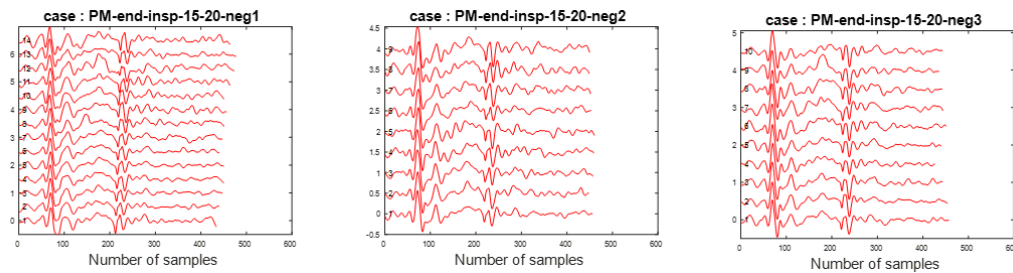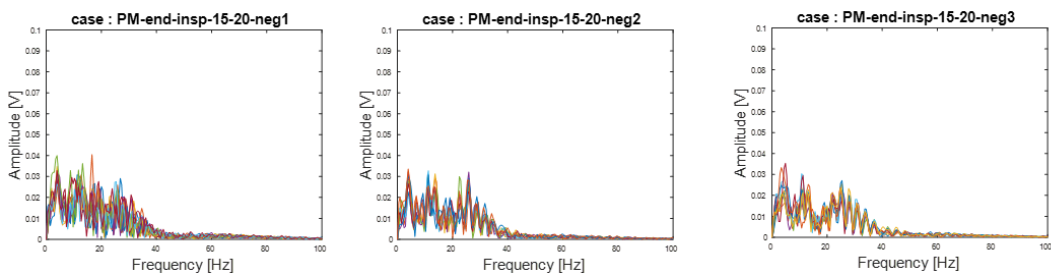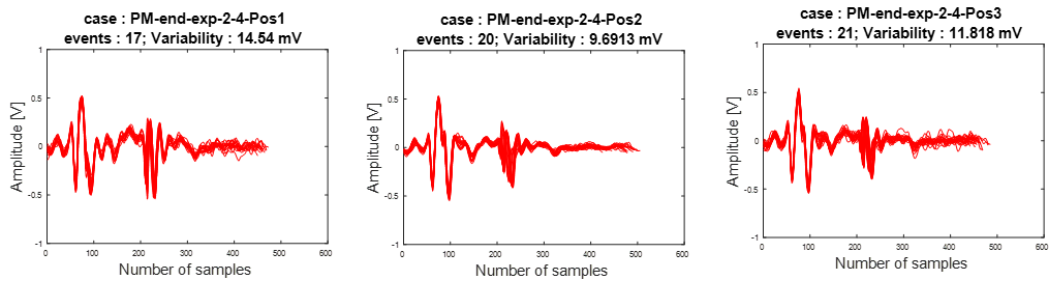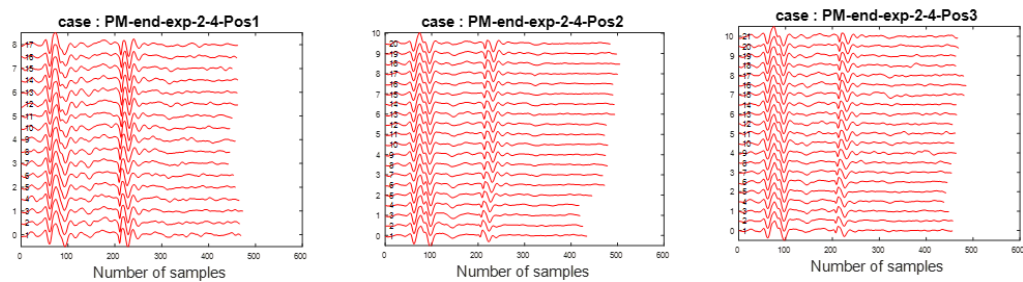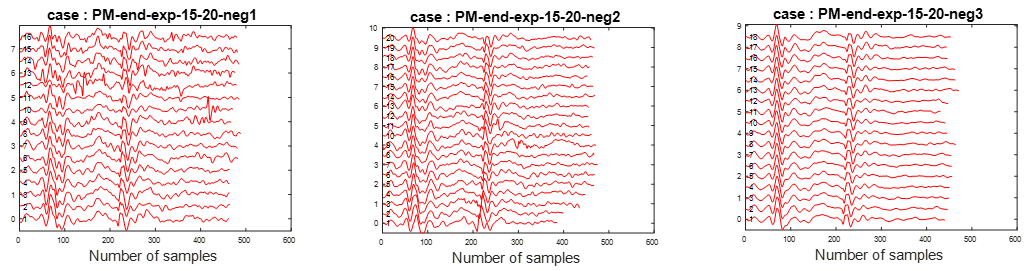
Figure 86 Time domain analysis during 3 runs of end expiration at negative 15-20 cm water pressure where events are plotted on top of previous SCG event for a subject.
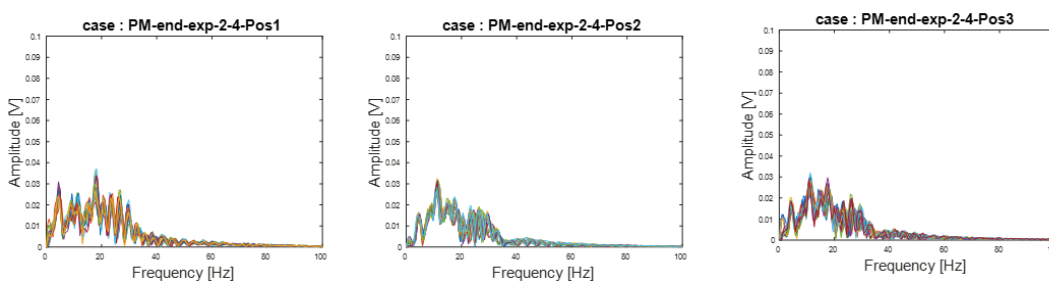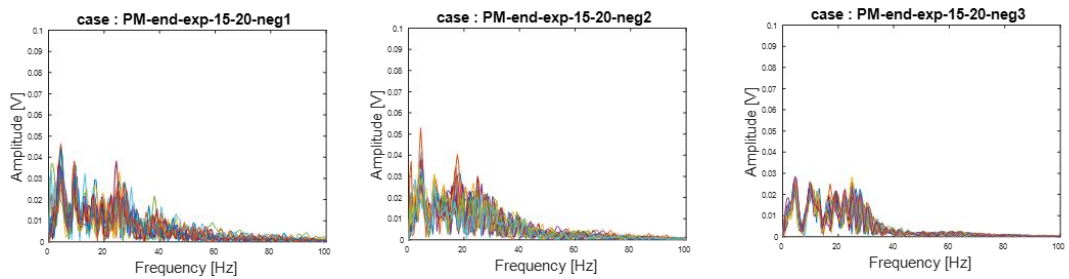

Figure 87 Frequency domain analysis during 3 runs of end expiration at negative 15-20 cm cm water pressure where the spectra of each SCG event are plotted on top of each other.

APPENDIX B: CLUSTER ANALYSIS OF SCG EVENTS DURING NORMAL BREATHING

Objective: The objective of this study is to perform cluster distribution for each subjects to show how SCG can accurately cluster during normal breathing.

Methods: Unsupervised k-medoid clustering was performed and clustering accuracy was calculated for each subjects after SCG segmentation.

Findings: Cluster distribution and clustering accuracy for normal breathing of 1 min are shown for some sample subjects. Figure 88 shows cluster distribution and accuracy of normal breathing for 5 runs for subject 2. Here, the accuracy of cluster distribution are
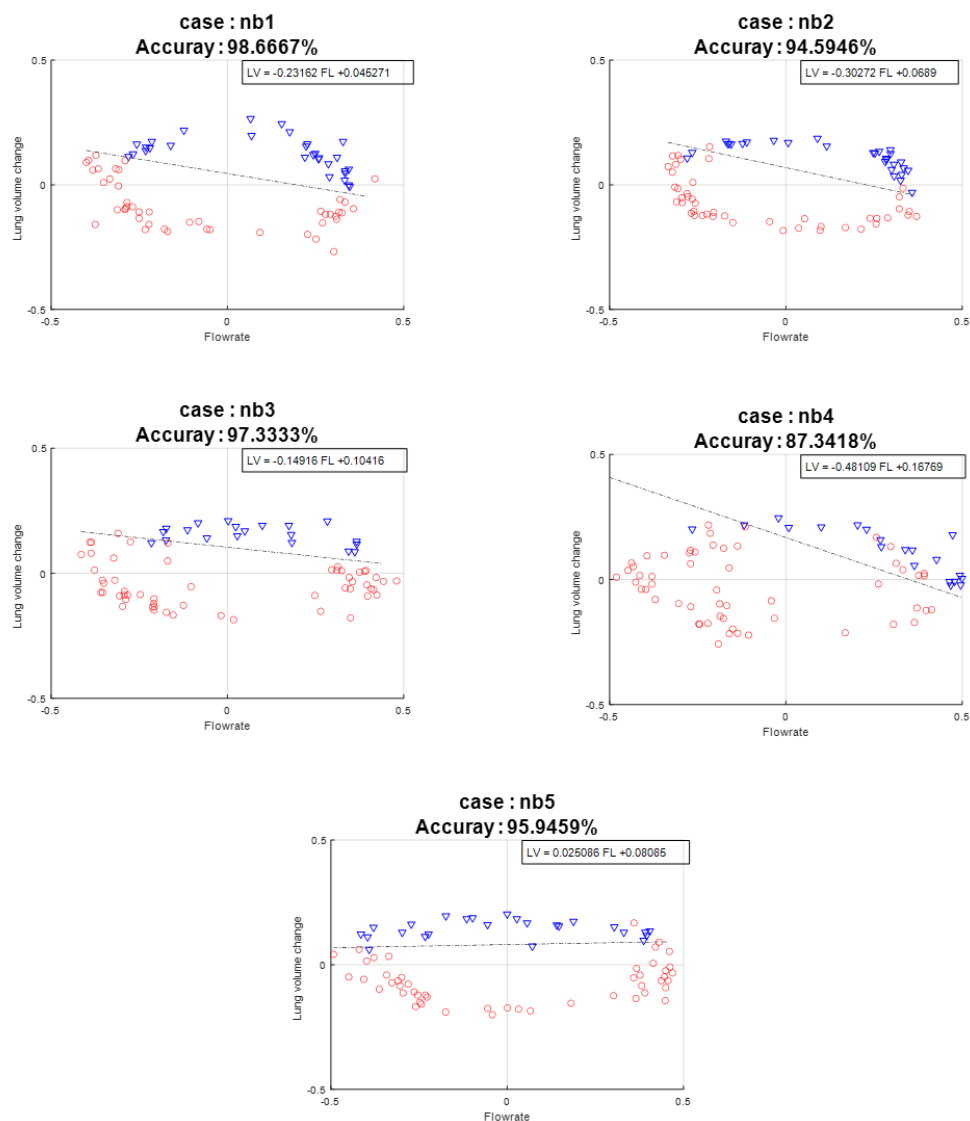
Figure 88 Cluster distribution and the accuracy of normal breathing for 5 runs (1 min each) for subject 2.

99, 95, 97, 87 and 96%, respectively. Figure 89 shows cluster distribution and accuracy of normal breathing for 5 runs for subject 4. Here, the accuracy of cluster distribution for 5 runs are respectively 82, 90, 96, 93 and 94%. Figure 90 shows cluster distribution and accuracy of normal breathing for 5 runs for subject 7. Here, the accuracy of cluster distribution for 5 runs are respectively 100, 99, 95, 94 and 91%. Figure 91 shows cluster distribution and accuracy of normal breathing for 5 runs for subject 14.
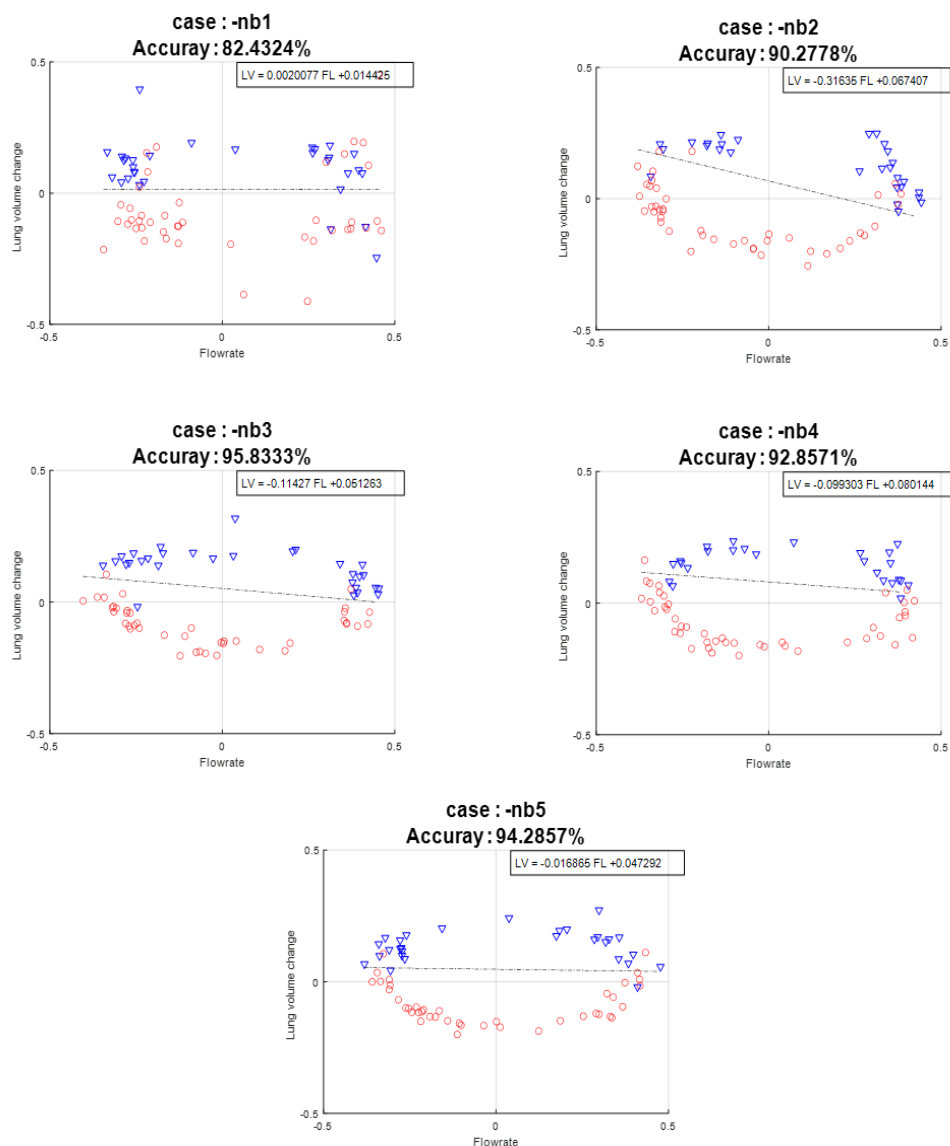
Figure 89 Cluster distribution and the accuracy of normal breathing for 5 runs (1 min each) for subject 4.

Here, the accuracy of cluster distribution for 5 runs are respectively 98, 100, 98, 97 and 92%. Figure 92 shows cluster distribution and accuracy of normal breathing for 5 runs for subject 15. Here, the accuracy of cluster distribution for 5 runs are respectively 83, 94, 100, 94 and 98%.
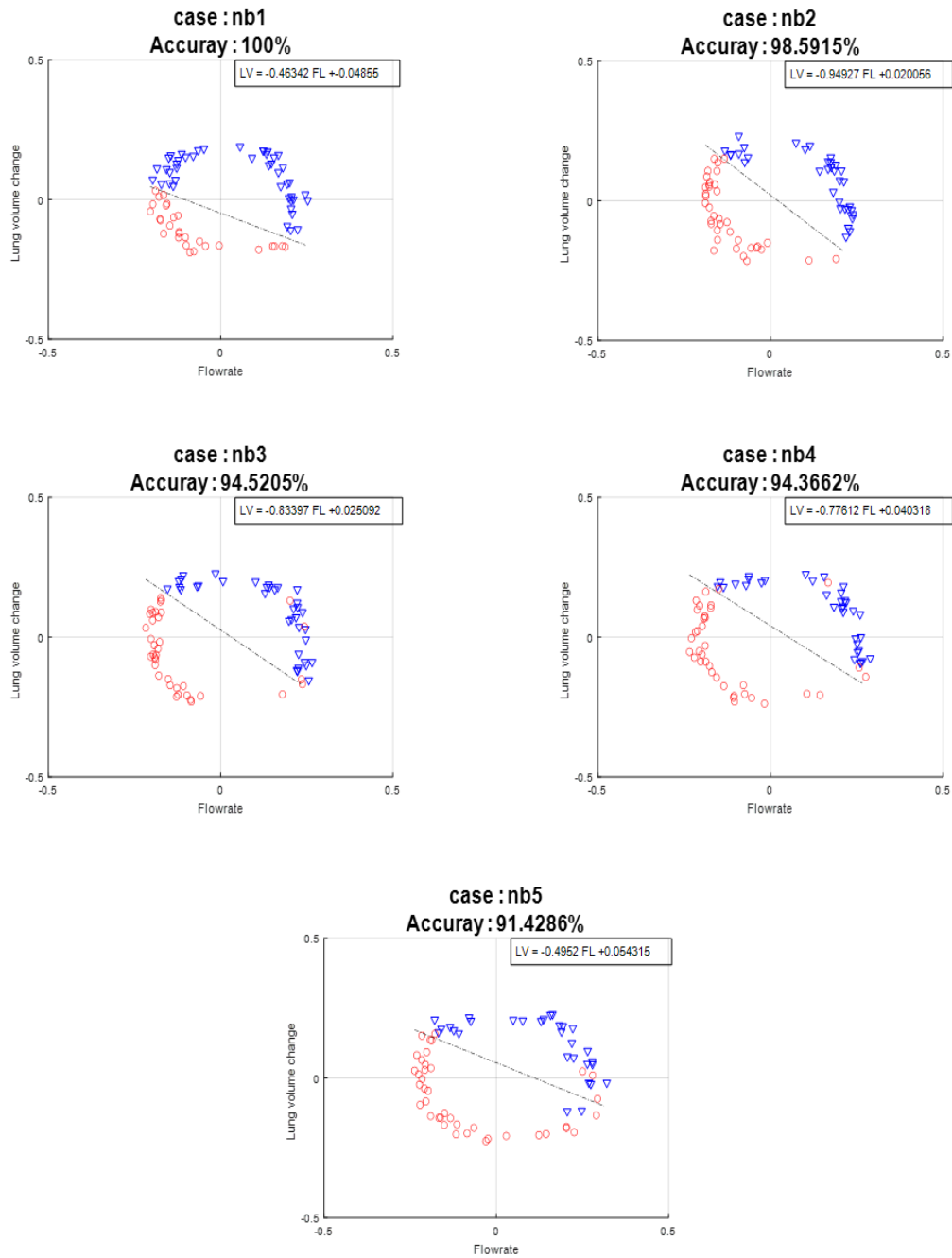
Figure 90 Cluster distribution and the accuracy of normal breathing for 5 runs (1 min each) for subject 7.
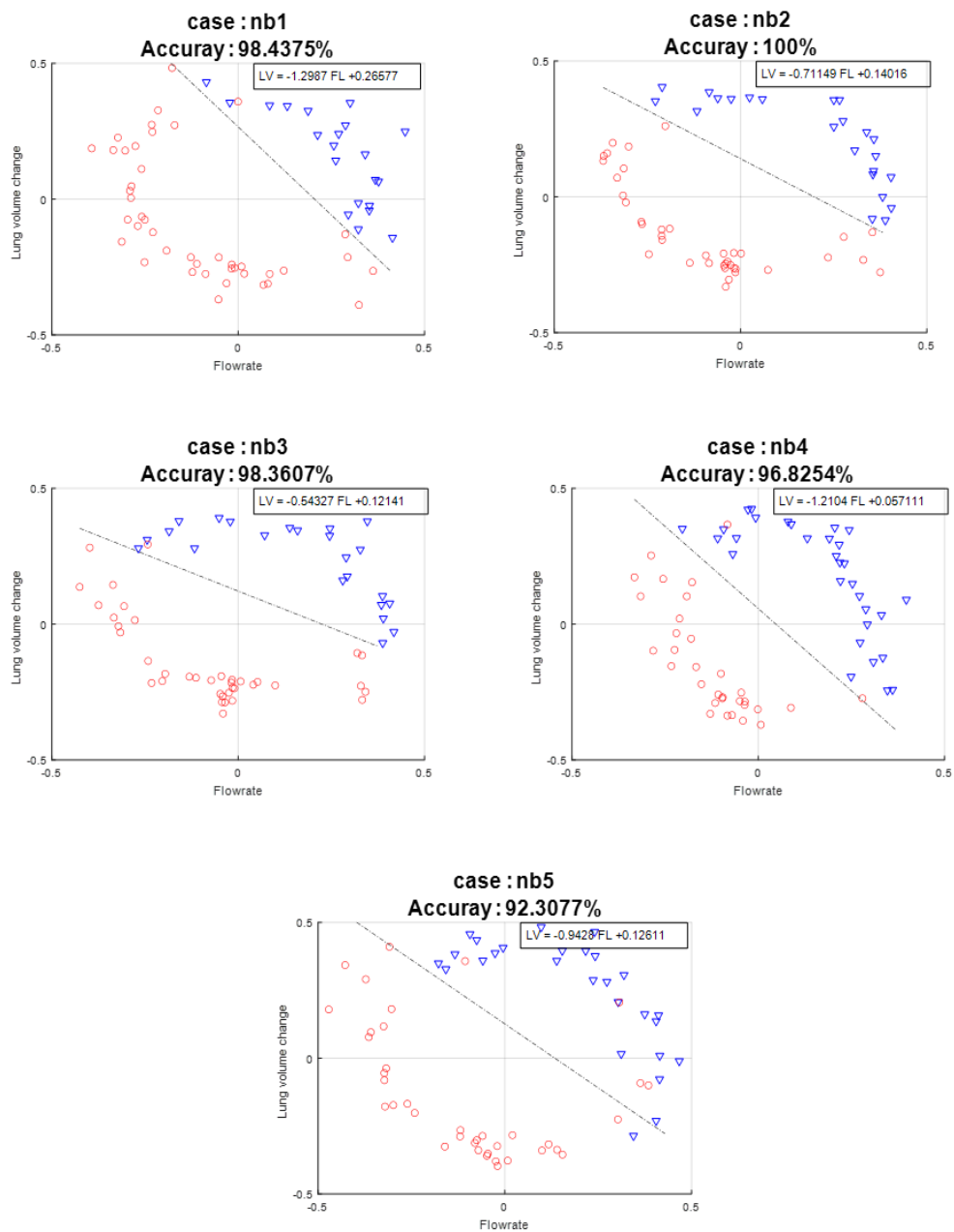
Figure 91 Cluster distribution and the accuracy of normal breathing for 5 runs (1 min each) for subject 14.
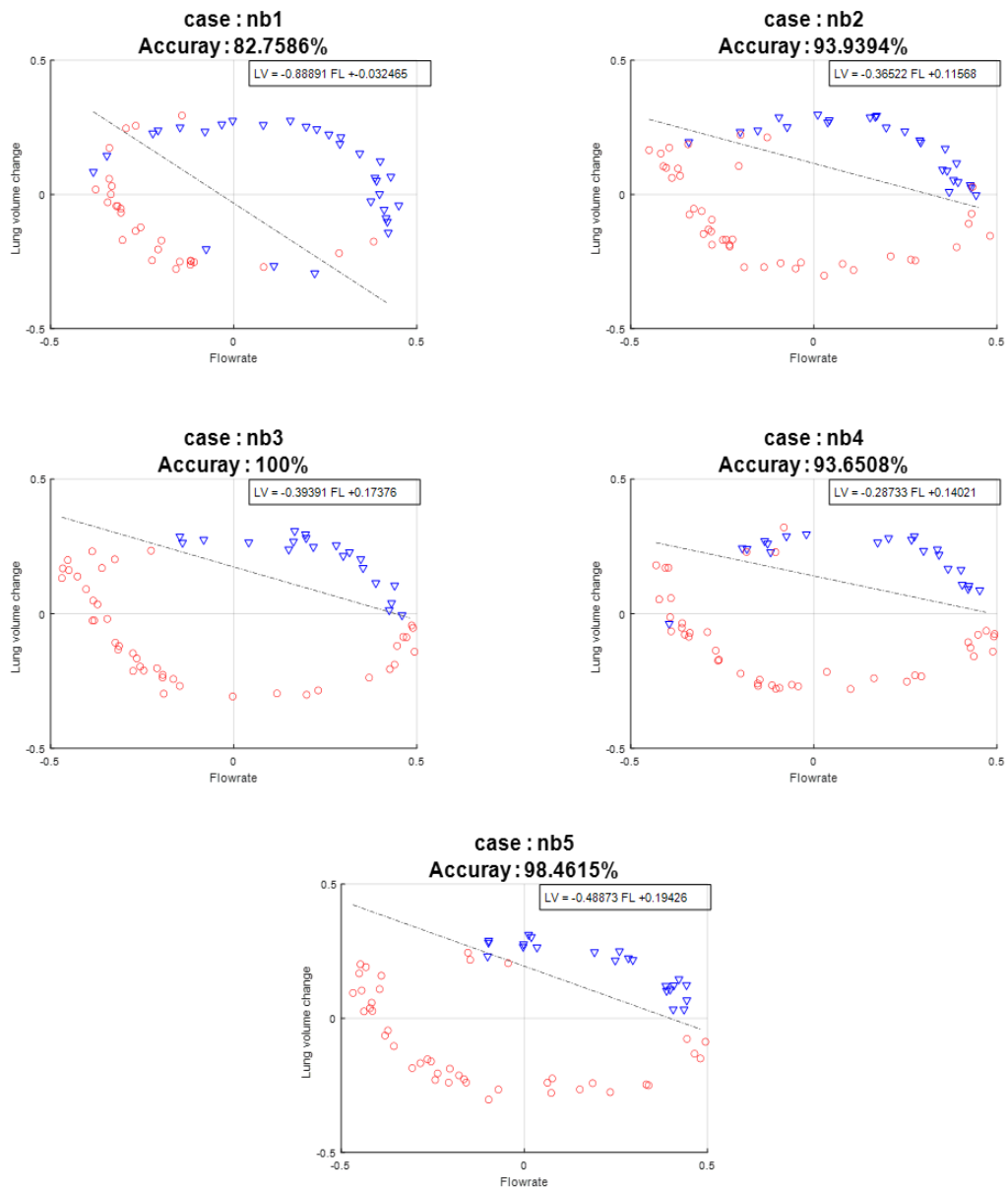
Figure 92 Cluster distribution and the accuracy of normal breathing for 5 runs (1 min each) for subject 15.

APPENDIX C: IRB INFORMATION

☰ ⚖ Compare   «

◀ Go to forms menu   🖶 Print ▼   ❓ Help

CH SUITE

Hello, **Hansen Mansy** ▼

You Are Here: 📄 A device for monitoring heart …

Reading: BIO-16-12783

Basic Study
Information

**Study Funding
Sources**

Local Study Team
Members

Study Scope

Local Research
Locations

Local Site
Documents

UCF Additional
Information

Basic Study Information ❓

1. *** Title of study:**
A device for monitoring heart failure patients

2. *** Short title:** ❓
A device for monitoring heart failure patients

3. *** Brief description:** ❓
We will study how heart sounds and vibrations can detect changes in heart activity. If
successful it can lead us to develop new low-cost and non-invasive methods for monitoring
heart desease including heart failure.

4. *** What kind of study is this?** ❓
Single-site study

5. *** Will an external IRB act as the IRB of record for this study?** ❓
○ Yes ● No

6. *** Local principal investigator:** ❓
Hansen Mansy

7. *** Does the local principal investigator have a financial interest related to
this research?** ❓
● Yes ○ No

8. *** Attach the protocol:** ❓

	Document	Category	Date Modified	Document History
View	📄 HF_Application_04.23.21.docx(0.02)	IRB Protocol	4/23/2021	History

Study Funding Sources ❓

1. Identify each organization supplying funding for the study: ❓

Funding Source	Sponsor's Funding ID	Grants Office ID	Attachments

❌ Exit

≡ ⚖ Compare   «

	Funding Source	Sponsor's Funding ID	Grants Office ...
Biomedical Acoustics Research Company			1059481

◀ Go to forms menu   🖨 Print ▼   ❓ Help

Basic Study Information

Study Funding Sources

Local Study Team Members

Study Scope

Local Research Locations

Local Site Documents

UCF Additional Information

Local Study Team Members

1. **Identify each additional person involved in the design, conduct, or reporting of the research:** ❓

Name	Roles	Financial Interest	Involved in Consent	Access to Data	E-mail	Phone
Rajkumar Dhar	Research Assistant	no	yes	no	rajkumar.dhar@knights.ucf.edu	
Tanvir Hassan	Co-Investigator	no	yes	no	thassan@knights.ucf.edu	
Daniella King	Research Assistant	no	yes	no	Daniella.King@ucf.edu	
Badrun Nessa Rahman	Research Assistant	no	yes	yes	bnessa@knights.ucf.edu	407/427-5692
Richard Sandler	Co-Investigator	yes	yes	yes	rhsandler@gmail.com	407/286-5794
Anna Voyatzoglou	Research Assistant	no	yes	no	voyatzoglou@knights.ucf.edu	

2. **External team member information:** ❓

Name	Description
There are no items to display	

Study Scope ❓

1. **★ Does the study specify the use of an approved drug or biologic, use an unapproved drug or biologic, or use a food or dietary supplement to diagnose, cure, treat, or mitigate a disease or condition?** ❓
   ○ Yes ● No

2. **★ Does the study evaluate the safety or effectiveness of a device or use a humanitarian use device (HUD)?** ❓
   ○ Yes ● No

Local Research Locations ❓

1. **Identify research locations where research activities will be conducted or overseen by the local investigator:**

Location	Contact	Phone	Email

❌ Exit

APPENDIX D: IRB APPROVAL

UNIVERSITY OF CENTRAL FLORIDA

<u>APPROVAL</u>

January 14, 2022

Dear Hansen Mansy:

On 9/30/2021, the IRB reviewed the following submission:

Type of Review:	Modification / Update to study team members
Title:	A device for monitoring heart failure patients
Investigators:	Hansen Mansy, PI Richard Sandler, Co-I Tanvir Hassan, Co-I
IRB ID:	MOD00002164
Funding:	Name: Biomedical Acoustics Research Company, Grant Office ID: 1059481
Grant ID:	None
IND, IDE, or HDE:	None
Documents Reviewed:	None

The IRB approved the protocol from 9/30/2021 to 5/24/2022.

In conducting this protocol, you are required to follow the requirements listed in the Investigator Manual (HRP-103), which can be found by navigating to the IRB Library within the IRB system. Guidance on submitting Modifications and a Continuing Review or Administrative Check-in are detailed in the manual. When you have completed your research, please submit a Study Closure request so that IRB records will be accurate.

If you have any questions, please contact the UCF IRB at 407-823-2901 or irb@ucf.edu. Please include your project title and IRB number in all correspondence with this office.

Sincerely,

Renea Carver
Designated Reviewer

Page 1 of 1

LIST OF REFERENCES

Abrams, J. (1978). Current Concepts of the Genesis of Heart Sounds: I. First and Second Sounds. Jama, 239(26), 2787–2789.

Akhbardeh, A., Tavakolian, K., Gurev, V., Lee, T., New, W., Kaminska, B., & Trayanova, N. (2009). Comparative analysis of three different modalities for characterization of the seismocardiogram. Paper presented at the Conference Proceedings.

Al-Mayah, A., Moseley, J., & Brock, K. (2007). Contact surface and material nonlinearity modeling of human lungs. Physics in Medicine & Biology, 53(1), 305.

Azad, M. K., Gamage, P. T., Sandler, R. H., Raval, N., & Mansy, H. A. (2019). Seismocardiographic Signal Variability During Regular Breathing and Breath Hold in Healthy Adults. 2019 IEEE Signal Processing in Medicine and Biology Symposium (SPMB), 3–6.

Azad, M. K. (2020). Seismocardiographic Signal Variability and Pulmonary Phase Detection in Adults. University of Central Florida.

Bland, J. M., & Altman, D. G. (1999). Measuring agreement in method comparison studies. Statistical Methods in Medical Research, 8(2), 135–160.

Bozhenko, B. (1961). Seismocardiography--a new method in the study of functional conditions of the heart. Terapevticheskii arkhiv, 33, 55.

Chen, T., & Guestrin, C. (2016). Xgboost: A scalable tree boosting system. In Proceedings of the 22nd acm sigkdd international conference on knowledge discovery and data mining (pp. 785-794).

Cozic, M., Durand, L.-G., & Guardo, R. (1998). Development of a cardiac acoustic mapping system. Medical and Biological Engineering and Computing, 36(4), 431–437.

Crow, R. S., Hannan, P., Jacobs, D., Hedquist, L., & Salerno, D. M. (1994). Relationship between seismocardiogram and echocardiogram for events in the cardiac cycle. American Journal of Noninvasive Cardiology, 8, 39–46.

Dijkstra, E. W. (1959). A note on two problems in connexion with graphs. Numerische Mathematik, 1(1), 269–271.

Fawcett, T. (2006). An introduction to ROC analysis. Pattern recognition letters, 27(8), 861-874.

Gamage, P. T., Khurshidul.Azad, M., Taebi, A., Sandler, R. H., & Mansy, H. A. (2018). Clustering Seismocardiographic Events using Unsupervised Machine Learning. 2018 IEEE Signal Processing in Medicine and Biology Symposium (SPMB), 1–5. https://doi.org/10.1109/SPMB.2018.8615615

Gamage, P. T., Azad, M. K., Sandler, R. H., & Mansy, H. A. (2019). Modeling Seismocardiographic Signal using Finite Element Modeling and Medical Image Processing. 2019 IEEE Signal Processing in Medicine and Biology Symposium (SPMB), 1–4.

Gamage, P. T., Azad, M. K., Taebi, A., Sandler, R. H., & Mansy, H. A. (2020). Clustering of SCG Events Using Unsupervised Machine Learning. In I. Obeid, I. Selesnick, & J. Picone (Eds.), Signal Processing in Medicine and Biology: Emerging Trends in Research and Applications (pp. 205–233). Springer International Publishing. https://doi.org/10.1007/978-3-030-36844-9_7

Gamage, P. (2020). Seismocardiography-Genesis, and Utilization of Machine Learning for Variability Reduction and Improved Cardiac Health Monitoring. University of Central Florida.

Glower, D. D., Murrah, R. L., Olsen, C. O., Davis, J. W., & Rankin, J. S. (1992). Mechanical correlates of the third heart sound. Journal of the American College of Cardiology, 19(2), 450–457.

Hosenpud, J. D., & Greenberg, B. H. (2007). Congestive heart failure. Lippincott Williams & Wilkins.

Hassan, T., Mckinney, L., Sandler, R. H., Kassab, A., Price, C., Moslehy, F., & Mansy, H. A. (2018). An Acoustic Approach for Detection of Developmental Dysplasia of Hip. 2018 IEEE Signal Processing in Medicine and Biology Symposium (SPMB), pp. 1-6.

Hassan, T., Mckinney, L., Sandler, R. H., Kassab, A., Price, C., Moslehy, F., & Mansy, H. A. (2019). A System for Measuring Sound Transmission Through Joints. 2019 IEEE Signal Processing in Medicine and Biology Symposium (SPMB), pp. 1-4.

Hassan, T., Sandler, R., Price, C., Kassab, A., & Mansy, H. (2020). Detecting Hip Dysplasia Using Acoustic Excitation in a Pig Model. 2020 IEEE Signal Processing in Medicine and Biology Symposium (SPMB), pp. 1-3.

Hassan, T. (2019). Detection of DDH in Infants and Children Using Audible Acoustics. University of Central Florida.

Hassan, T., Rahman, B., Sandler, R. H., & Mansy, H. A. (2021). Effect of Normal Breathing and Breath Holding on Seismocardiographic Signals and Heart Rate.

2021 IEEE Signal Processing in Medicine and Biology Symposium (SPMB), pp. 1-6.

Javaid, A. Q., Dowling, S., Etemadi, M., Heller, J. A., Roy, S., Klein, L., & Inan, O. T. (2016). Quantification of posture induced changes in wearable seismocardiogram signals for heart failure patients. Computing in Cardiology Conference (CinC), 2016, 777–780.

Kawamura, Y., Yokota, Y., & Nogata, F. (2007). Propagation route estimation of heart sound through simultaneous multi-site recording on the chest wall. 2007 29th Annual International Conference of the IEEE Engineering in Medicine and Biology Society, 2875–2878.

Kompis, M, Pasterkamp, H., Motai, Y., & Wodicka, G. R. (1998). Spatial representation of thoracic sounds. Proceedings of the 20th Annual International Conference of the IEEE Engineering in Medicine and Biology Society. Vol. 20 Biomedical Engineering Towards the Year 2000 and Beyond (Cat. No. 98CH36286), 3, 1661–1664.

Kompis, Martin, Pasterkamp, H., & Wodicka, G. R. (2001). Acoustic imaging of the human chest. Chest, 120(4), 1309–1321.

Lin, W. Y., Chou, W. C., Chang, P. C., Chou, C. C., Wen, M. S., Ho, M. Y., Lee, W.C., Hsieh, M. J., Lin, C. C., & Tsai, T. H. (2018). Identification of location specific feature points in a cardiac cycle using a novel seismocardiogram spectrum system. IEEE Journal of Biomedical and Health Informatics, 22(2), 442–449.

Luu, L., & Dinh, A. (2018). Artifact Noise Removal Techniques on Seismocardiogram Using Two Tri-Axial Accelerometers. Sensors, 18(4), 1067.

Nogata, F., Yokota, Y., & Kawamura, Y. (2014). Distribution of Vibration of Chest Surface with Heart Movement. Frontiers in Sensors, 2, 26–31.

Nogata, F., Yokota, Y., Kawamura, Y., Morita, H., & Uno, Y. (2010). Visualization of Heart Motion by Analysis of Chest Vibration. Analysis of Biomedical Signals and Images, 20, 11–16.

Okada, M. (1982). Chest wall maps of heart sounds and murmurs. Computers and Biomedical Research, 15(3), 281–294.

Pan, J., & Tompkins, W. J. (1985). A real-time QRS detection algorithm. IEEE Trans. Biomed. Eng, 32(3), 230–236.

Pandia, K., Inan, O. T., Kovacs, G. T. A., & Giovangrandi, L. (2012). Extracting respiratory information from seismocardiogram signals acquired on the chest using a miniature accelerometer. Physiological Measurement, 33(10), 1643.

Paparrizos, J., & Gravano, L. (2017). Fast and accurate time-series clustering. ACM Transactions on Database Systems (TODS), 42(2), 8.

Rahman, B., Hassan, T., Azad, M., Sandler, R. H., & Mansy, H. A. (2021). The Identification of Respiratory Phase Using Support Vector Machines and Extreme Gradient Boosting. 2021 IEEE Signal Processing in Medicine and Biology Symposium (SPMB), pp. 1-5.

Raodeo, P., Brown, L., Hartig, M., Hassan, T., Sandler, R. H., Price, C., & Mansy, H. A. (2021). A Chicken Model for Acoustic Detection of Developmental Hip Dysplasia. 2021 IEEE Signal Processing in Medicine and Biology Symposium (SPMB), pp. 1-3.

Sakoe, H., & Chiba, S. (1978). Dynamic programming algorithm optimization for spoken word recognition. IEEE Transactions on Acoustics, Speech, and Signal Processing, 26(1), 43–49.

Salerno, D. M. (1990). Seismocardiography: A new technique for recording cardiac vibrations. Concept, method, and initial observations. Journal of cardiovascular technology, 9(2), 111-118.

Sandler, R. H., Azad, K., Rahman, B., Taebi, A., Gamage, P., Raval, N., Mentz, R. J., & Mansy, H. A. (2019). Minimizing Seismocardiography Variability by Accounting for Respiratory Effects. Journal of Cardiac Failure, 25(8), S172.

Sandler, R. H., Hassan, T., Rahman, B., Raval, N., Mentz, R. J., & Mansy, H. A. (2021). Seismocardiographic Signal Variability During Regular Breathing and Breath Holding. Journal of Cardiac Failure.

Sandler, R. H., Hassan, T., Azad, K., Rahman, B., Raval, N., Mentz, R. J., & Mansy, H. A. (2021). Respiratory Phase Detection From Seismocardiographic Signals Using Machine Learning. Journal of Cardiac Failure.

Sapsanis, C., Welsh, N., Pozin, M., Garreau, G., Tognetti, G., Bakhshaee, H., Pouliquen, P. O., Mitral, R., Thompson, W. R., & Andreou, A. G. (2018). StethoVest: A simultaneous multichannel wearable system for cardiac acoustic mapping. 2018 IEEE Biomedical Circuits and Systems Conference (BioCAS), 1–4.

Shafiq, G., Tatinati, S., Ang, W. T., & Veluvolu, K. C. (2016). Automatic identification of systolic time intervals in seismocardiogram. Scientific Reports, 6, 37524.

Siejko, K. Z., Thakur, P. H., Maile, K., Patangay, A., & OLIVARI, M. (2013). Feasibility of heart sounds measurements from an accelerometer within an ICD pulse generator. Pacing and Clinical Electrophysiology, 36(3), 334–346.

Silva, D. F., & Batista, G. E. (2016). Speeding up all-pairwise dynamic time warping matrix calculation. Proceedings of the 2016 SIAM International Conference on Data Mining, 837–845.

Šipinková, I., Hahn, G., Meyer, M., Tadlanek, M., & Hajek, J. (1997). Effect of respiration and posture on heart rate variability. Physiol. Res, 46, 173–179.

Solar, B. E., Taebi, A., & Mansy, H. A. (2017). Classification of Seismocardiographic Cycles into Lung Volume Phases. 2017 IEEE Signal Processing in Medicine and Biology Symposium (SPMB), pp. 1–2.

Taebi, A. (2018). Characterization, Classification, and Genesis of Seismocardiographic Signals. University of Central Florida.

Taebi, A., & Mansy, H. A. (2017). Time-Frequency Distribution of Seismocardiographic Signals: A Comparative Study. Bioengineering, 4(2), 32. https://doi.org/10.3390/bioengineering4020032

Taebi, A., & Mansy, H. A. (2017). Grouping Similar Seismocardiographic Signals Using Respiratory Information. 2017 IEEE Signal Processing in Medicine and Biology Symposium (SPMB), pp. 1–6.

Taebi, A., Solar, B. E., Bomar, A. J., Sandler, R. H., & Mansy, H. A. (2019). Recent advances in seismocardiography. Vibration, 2(1), 64–86.

Tavakolian, K. (2010). Characterization and analysis of seismocardiogram for estimation of hemodynamic parameters. Applied Science: School of Engineering Science.

Tavakolian, K. (2016). Systolic time intervals and new measurement methods. Cardiovascular Engineering and Technology, 7(2), 118–125.

Tavakolian, K., Portacio, G., Tamddondoust, N. R., Jahns, G., Ngai, B., Dumont, G. A., & Blaber, A. P. (2012). Myocardial contractility: A seismocardiography approach. Engineering in Medicine and Biology Society (EMBC), 2012 Annual International Conference of the IEEE, 3801–3804.

Virani, S. S., Alonso, A., Benjamin, E. J., Bittencourt, M. S., Callaway, C. W., Carson, A. P., Chamberlain, A. M., Chang, A. R., Cheng, S., & Delling, F. N. (2020). Heart Disease and Stroke Statistics-2020 Update: A Report from the American Heart Association. Circulation, CIR0000000000000757.

Watanabe, N., Reece, J., & Polus, B. I. (2007). Effects of body position on autonomic regulation of cardiovascular function in young, healthy adults. Chiropractic & Osteopathy, 15(1), 19.

Zakeri, V., Akhbardeh, A., Alamdari, N., Fazel-Rezai, R., Paukkunen, M., & Tavakolian, K. (2017). Analyzing seismocardiogram cycles to identify the respiratory phases. IEEE Transactions on Biomedical Engineering, 64(8), 1786-1792.

Zanetti, J., Poliac, M., & Crow, R. (1991). Seismocardiography: waveform identification and noise analysis. Paper presented at the [1991] Proceedings Computers in Cardiology.

Zanetti, J. M., & Tavakolian, K. (2013). Seismocardiography: Past, present and future. Paper presented at the 2013 35th Annual International Conference of the IEEE Engineering in Medicine and Biology Society (EMBC).

Zeng, Y., Yager, D., & Fung, Y. (1987). Measurement of the mechanical properties of the human lung tissue. Journal of biomechanical engineering, 109(2), 169-174.

Zigras, T. C. (2007). Biomechanics of human pericardium: a comparative study of fresh and fixed tissue. McGill University Doctoral dissertation.